DISSERTATION

PHOTOTUNABLE BLOCK COPOLYMER HYDROGELS

Submitted by

Nabila A. Huq

Department of Chemical and Biological Engineering

In partial fulfillment of the requirements

For the Degree of Doctor of Philosophy

Colorado State University

Fort Collins, Colorado

Fall 2017

Doctoral Committee:

    Advisor: Travis S. Bailey

    Matthew J. Kipper
    Melissa M. Reynolds
    Christopher D. Snow

ABSTRACT

PHOTOTUNABLE BLOCK COPOLYMER HYDROGELS

Thermoplastic elastomer (TPE) hydrogel networks, based on swelling of nanostructured blends

of amphiphilic, sphere-forming AB diblock and ABA triblock copolymers, provide direct access

to thermally processable plastics that exhibit exceptional elastic recovery and fatigue resistance

even after hydration. In such two-component systems, the ratio of ABA to AB block copolymer

(BCP) is used to control the resultant swelling ratio, system modulus, and overall mechanical

response. This dissertation focuses on developing material strategies through which adjustment

of such AB/ABA ratios, and thus the resultant properties, can be accomplished using light. The

chapters within capture the manipulation of a photoreactive AB diblock copolymer micelle-like

spheres to controllably generate ABA triblock copolymer and the network nanostructure *in situ*,

both in the melt state and after dispersal in solution. This was accomplished using efficient

photoinduced [4 + 4]cycloaddition (λ = 365 nm) between terminal anthracene units on a ω-

anthracenylpolystyrene-*b*-poly(ethylene oxide) diblock copolymer precursor to produce the

desired amount of polystyrene-*b*-poly(ethylene oxide)-*b*-polystyrene triblock copolymer. This

direct, UV-mediated handle on tethering between adjacent micelles in the BCP matrix was found

to be capable of controllably manipulating hydrogel material properties using (1) duration of

irradiation, (2) hydration level and consequent micelle spacing upon exposure, and (3)

photopatterning strategies to spatially direct swelling and mechanics. This level of control

yielded an array of hydrogels, ranging from those irradiated in the dry melt to produce high-

modulus, elastic materials suited for fibrocartilage repair and replacement, to moldable or

injectable precursor solutions irradiated into soft, conformally shaped TPE hydrogels ideal for use in high contact applications such as wound healing. The development and scope of this versatile new photoactive BCP system is enclosed.

ACKNOWLEDGMENTS

DEDICATION

For my family, who decided it was a good idea to teach a three-year-old algebra.

TABLE OF CONTENTS

STRUCTURES AND ABBREVIATIONS

Abbreviation	Name	Definition, structure, or drawing
Anth	Anthracene	
BCC	Body-centered cubic	
BCP	Block copolymer	Covalently bound homopolymer chains (e.g. AB, ABC, ABA where a letter A, B, or C represents a chain of like monomer units).
BHT	Butylated hydroxy toluene	
DBX	Dibromoxylene	
DLS	Dynamic light scattering	Technique which uses Brownian motion to determine size distribution of macromolecules and nanoparticles in solution.
G'	Storage/elastic modulus	A measure of the stored energy in a material, representing elastic characteristics of viscoelastic substances.
G"	Loss/viscous modulus	A measure of energy lost to heat in a material, representing viscous characteristics of viscoelastic substances.
GPC	Gel permeation chromatography	A type of size exclusion chromatography (see SEC) which reveals size distributions of analytes using movement through a porous gel column.

^{1}H NMR	Proton nuclear magnetic resonance	Spectroscopy technique which uses the properties of hydrogen nuclei to determine the structure of molecules.
IO	Polyisoprene-*b*-poly(ethylene oxide), PI-*b*-PEO	
LLP	Liquid like packing of spheres	
PEO	Poly(ethylene oxide)	
PI	Polyisoprene	
PI-anth	Polyisoprene-anthracene	
PS	Polystyrene	
PS-anth	Polystyrene-anthracene	
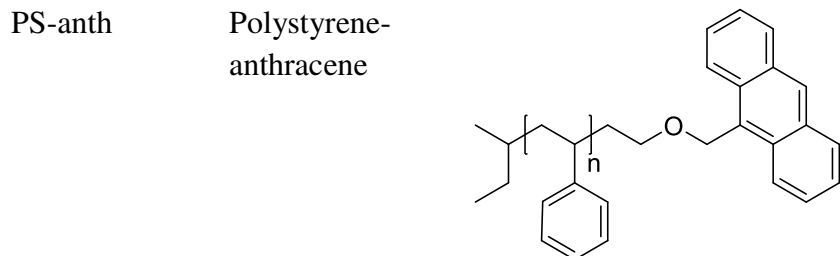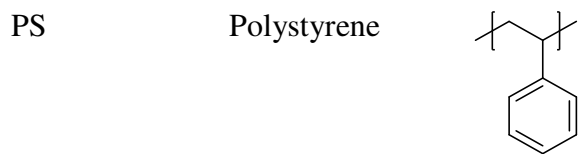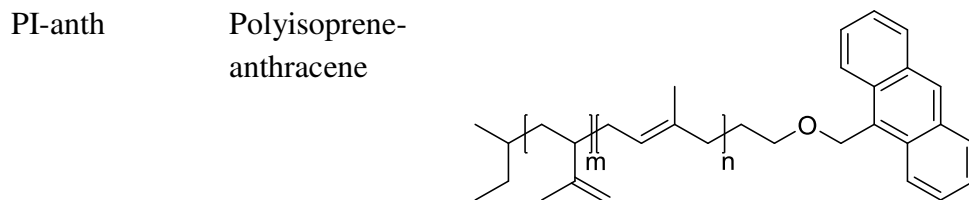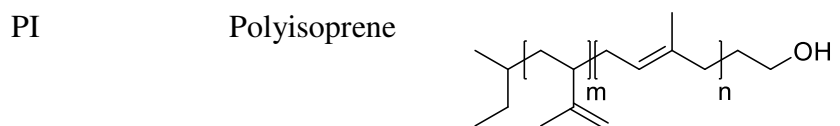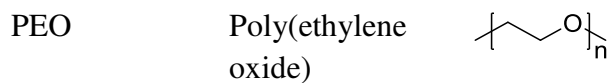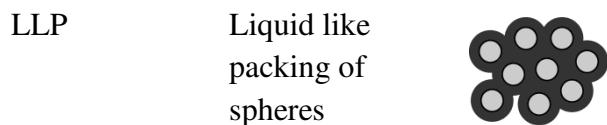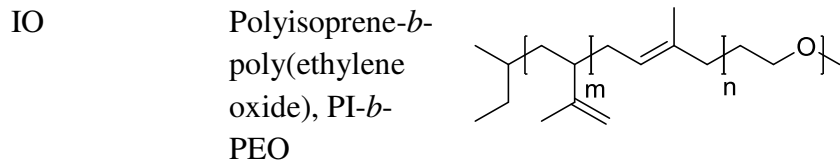
SAXS	Small angle X-ray scattering	Instrumentation technique used to determine morphology and domain structure at the nanoscale by analyzing scattering behavior of X-rays traveling through the material at small angles.
SEC	Size exclusion chromatography	Material characterization technique that separates components based on size.
SO-OH	Polystyrene-*b*-poly(ethylene oxide)-OH, PS-*b*-PEO-OH	
SOS	Polystyrene-*b*-poly(ethylene oxide)-b-polystyrene, PS-*b*-PEO-*b*-PS	*Or*
TEM	Transmission electron microscopy	Imaging technique using transmission (and scattering) of electrons through a sample for material visualization down to the order of angstroms.
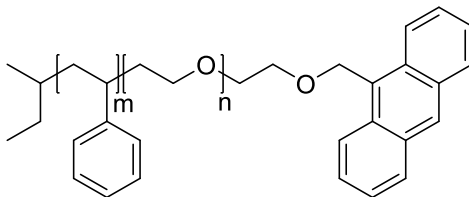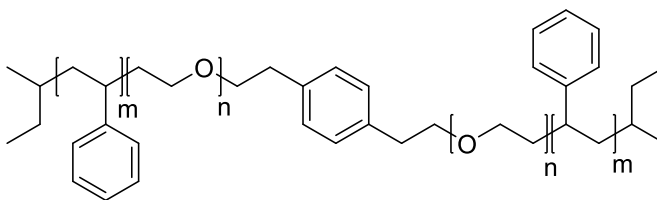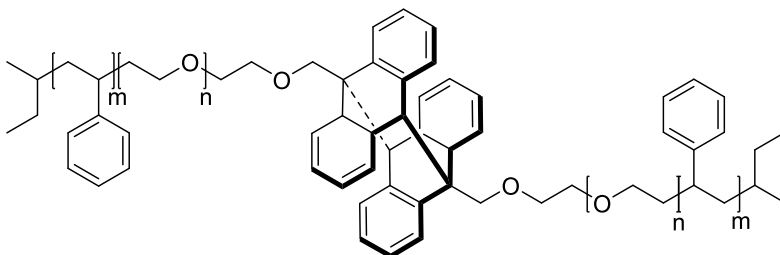
Chapter 1.

Introduction and Perspective of the Dissertation

1.1 Overview of the Dissertation

This introductory chapter serves to provide an overview of the research included in this dissertation. There are four main studies included:

1. Development of thermoplastic elastomer hydrogel networks which are mechanically phototunable in the melt state (**Chapter 3**).

2. Probing reversibility of network formation in this phototunable system toward the assessment of its applicability in antifouling ultrafiltration membranes (**Chapter 4**).

3. Adaptation of the phototunable hydrogel system to one in which materials are first synthesized as pourable or moldable solutions at ambient temperatures and then photocured to form soft, flexible, conformally shaped TPE hydrogels with potential for biomedical applications (**Chapter 5**).

4. Exploring potential of spatially directed, photoinstalled secondary networks as a means of influencing tensile properties and achieving unique surface topologies through photopatterning (**Chapter 6**).

Below are brief descriptions of each major study included in this dissertation.

1.1.1 Phototunable Thermoplastic Elastomer Hydrogel Networks (Chapter 3)

Thermoplastic elastomer hydrogel networks, based on swelling of nanostructured blends of amphiphilic, sphere-forming AB diblock and ABA triblock copolymers, provide direct access to thermally processable plastics that exhibit exceptional elastic recovery and fatigue resistance

even after hydration. In such two component systems, the ratio of ABA triblock copolymer to AB diblock copolymer is used to control the resultant swelling ratio, system modulus, and overall mechanical response. In this chapter, a simplified one-component alternative is introduced which exploits a single component, photoreactive AB diblock copolymer precursor to controllably generate ABA triblock copolymer in situ during melt-processing. This was accomplished using efficient photoinduced [4 + 4]cycloaddition (λ = 365 nm) between terminal anthracene units on a ω-anthracenylpolystyrene-b-poly(ethylene oxide) diblock copolymer precursor (SO-anth, f_{PS} = 0.13, M_n = 70100 g mol^{-1}) to produce the desired amount of polystyrene-b-poly(ethylene oxide)-b-polystyrene (SOS) triblock copolymer. The amount of SOS triblock copolymer formed was tunable (from 11.7 to 45 mol%) using UV exposure time (2 to 20 min, ~30 mW cm^{-2}) in the melt state, giving direct control over swelling and mechanical properties in the resultant hydrogels produced upon cooling and subsequent vitrification of the sample followed by addition of water. Hydrogels produced in this manner were found to exhibit dynamic shear moduli and shape preservation characteristics typical of preblended, two component SO/SOS TPE hydrogels of similar SOS concentrations.

1.1.2 Reversible Photocoupling (Chapter 4)

While Chapters 3, 5, and 6 focus primarily on coupling of anthracene end groups of SO-based polymer micelles, this chapter focuses more closely on the reversible aspect of anthracene dimerization. Anthracene can be repeatedly coupled (365 nm) and decoupled (254 nm) via UV irradiation, with 100% reversibility. In this study, we aimed to exploit this reversible coupling ability to allow polymer chain ends to be joined and separated repeatedly exploiting anthracene as a substituent. However, the ability to repeatedly couple and decouple chain ends was found to be challenging, with each successive irradiative cycle achieving a lower efficiency than the last.

2

A number of studies were performed in an attempt to discover the source of this limitation. First, based on the hypothesis that the anthracene group was being cleaved from the diblock copolymer chain end due to susceptibility of polystyrene to radical formation through absorption of the 254 nm light used for decoupling, we explored the effect of an alternate A block. To simplify the synthetic demands and remove the potential influence of the PEO, polystyrene (PS) and polyisoprene (PI) homopolymers were directly functionalized with anthracene. No significant improvement in an ability to repeatedly photocouple and decouple using PI was found. As a result, the potential of a radical inhibitor (BHT) to improve SO-anth's ability to reversibly photocouple was further explored. Addition of BHT provided some improved reversibility from initial experiments, however the ability to recouple after every subsequent decoupling cycle continued to decrease regardless.

1.1.3 Melt-fabricated photoreactive block copolymer micelles as building blocks for tunable elastomeric hydrogels (Chapter 5)

In this chapter, we studied the self-assembly behavior of the photoactive micelle building blocks described in Chapter 3, and adapted these building blocks to a system in which they were dispersed into moldable, water-based solutions. These solutions could then be irradiated to form a network at ambient temperatures. This system allowed the thermal processing step required for micelle formation to be divorced from network formation. Upon examining self-assembly of these spheres prior to dispersal in solution, evolution of the sphere morphology from its initial liquid-like packing to a highly ordered BCC lattice did not appear to be critical to the structural uniformity among micelles. The assembled micelle building blocks were then dispersed homogenously in water, resulting in pourable, spreadable, or moldable photoactive micelle solutions, depending on micelle concentration. Four concentrations of micelle precursor

solutions (8, 12, 16, 20 g water/g polymer) were studied for their ability to form elastomeric hydrogels once exposed to UV light. The stability of the precursor micelle solutions was confirmed over a period of nine weeks, showing no detectably significant change in micelle size distribution. Once put into molds, these solutions of varied concentration were then irradiated over a range of times (2.5 – 7.5 min) to form soft TPE hydrogels (dynamic shear G' = 0.6 to 3.3 kPa). The amount of installed triblock copolymer was dependent on UV exposure time, which in combination with the initially chosen micelle concentration, could be used to dictate the mechanical properties of the resultant hydrogels. These soft, conformally-shaped TPE hydrogels producible from the moldable or spreadable precursor solution are extremely desirable in a number of biomedical, surgical, and pharmaceutical applications.

1.1.4 Spatial control of mechanical properties and surface topography in a photoreactive block copolymer hydrogel (Chapter 6)

   In this chapter, a simple method for spatially directed mechanical reinforcement and surface feature implementation on the photoactive BCP-based TPE hydrogel system is presented. The work reveals findings on a hydrogel comprising a base amount of SOS triblock copolymer which serves as a primary tethering network (24 or 17 mol %), with the balance SO diblock copolymer primarily terminated with anthracene. Upon melt-state self-assembly followed by swelling to its equilibrium dimensions, photoinstallation of a secondary SOS network (up to a 6 mol % increase in SOS) resulted in two- to five-fold increase in toughening (from 86 to 224 and 35 to 168 kJ/m^3 for SOS-24 and SOS-17, respectively). This ability to photoinstall tethers *in situ* also presents a straightforward means to reinforce particular regions of a hydrogel, exploited here by incorporating photopatterned mechanical anisotropy, in addition to the formation of surface topography due to intrinsically restricted swelling in irradiated hydrogel regions.

Supplementary information specific to each chapter is provided at the end of that chapter. Additionally, **Chapter 2** serves to provide additional context and background information for the main research focus areas described above, and includes a review of key literature, and an overview of materials and synthetic strategies used.

Chapter 2.

Background and Motivation

This chapter provides an introduction to a versatile photoactive thermoplastic elastomer (TPE) hydrogel construct which shows promise for effective use in a number of applications. This material's mechanical tunability coupled with chemical suitability for biological environments makes it well-positioned for applications ranging from tissue replacement and repair, to separations, to dermal treatment and wound healing.

Generally, hydrogels are hydrophilic polymeric networks capable of absorbing large amounts of water or biological fluids.[1] These features, in addition to hydrogels' inherent porosity, low sliding friction, and low modulus, make them prime candidates for use in biomedical applications which require an ability to closely match properties of natural living tissue.[2] The ideal material for these applications is a largely non-cytotoxic, easily fabricated and applied material that is suitable for biological environments with uses such as contact lenses,[3] wound dressings,[4] drug delivery vehicles or scaffolds,[5] tissue engineering materials,[6, 7] and hygiene products.[1, 8] Depending on the desired end-use, hydrogels can be made either chemically stable, an advantageous quality in applications such as tissue repair or dermal treatment, or designed to degrade over time or with some stimulus, which is of particular interest in regenerative medicine (as temporary scaffolds) or drug delivery.[1, 9]

However, the use of traditional hydrogels in many biomedical applications is often limited by their mechanical capabilities. Most hydrogels are very brittle due to the low density of polymer chains upon swelling, and the lack of elasticity that can limit the extent of their use for load-

bearing or highly mobile biomedical applications.[10, 11] One example of increasing elasticity in a product to improve mechanical compatibility was seen in the replacement of hard contact lenses made from hydrophobic, non-elastic polymers with softer, elastic alternatives comprising hydrophilic polymer hydrogels. This had a marked positive effect on comfort and reduced irritation of the eye area due to the improved mechanical compatibility with the contacting tissue.[1, 3] The benefit of elasticity in contact lenses extended past just comfort to the arena of mechanical compatibility with surrounding tissues.

This requirement for the synthetic material to exhibit mechanical compatibility with surrounding tissue is also present in applications such as tissue scaffolding, or fibrocartilage repair. Most synthetic, biocompatible hydrogels are not mechanically comparable to natural biological tissue such as cartilage or muscle, often being unable to recover after deformation from physiological loading.[12] There is also an apparent barrier in designing a material which is easily modified to match the large variety of chemical and mechanical requirements present in the body.

Some efforts have been made to address the shortcomings of traditional hydrogels for biomedical applications, but often involve complex procedures and potentially dangerous monomeric byproducts.[1, 2] One example of a successful advance in combating limitations in mechanical properties came with the development of double-network (DN) hydrogels. These typically consist of two hydrophilic polymer component networks, one of which is brittle and the other, ductile.[13, 14] This construct allows for the sacrificial brittle network to dissipate energy through fracture upon deformation resulting in higher moduli, at which point the second softer, more ductile network can be engaged to prevent crack propagation, resulting in tougher hydrogel materials. While some DN hydrogels have exhibited toughness[15] and strength[16] comparable to

that of cartilage,[17] these DN hydrogels have not shown promise in their mechanical capabilities for effective soft tissue replacement materials. The fabrication process of DN hydrogels tends to produce heterogeneous networks unsuitable for applications which require retention of the macroscopic hydrogel shape upon swelling or loading, and exhibit low levels of fatigue resistance upon initial compression and tension due to irreversible failure of the primary brittle network.[11] Additionally, the fabrication process of such DN hydrogels for biomedical applications requires complex and time-intensive measures to ensure the removal of unreacted monomer, cross-linker, or oligomers to prevent the risk of cytotoxic responses as a result of leeched small molecules.[18] This leads us to consider an alternative route to exploit the advantages of hydrogels for applications which require mechanical and biological compatibility with tissue an DN hydrogels have exhibited, but which are fatigue resistant and require less complex fabrication. Our construct, based on block copolymer (BCP) species used to form thermoplastic elastomer hydrogels, is capable of high elasticity and fatigue resistance without complex synthetic procedures or use of small molecule monomers and harmful solvents after fabrication.

2.1 Development of TPE hydrogels for biomedical applications

BCPs have been used in a variety of applications largely due to their ability to form spatially uniform networks through thermodynamically driven nanoscale phase separation of covalently bonded dissimilar blocks.[19, 20] This homogeneity avoids the spatial inconsistencies found in many traditional hydrogels, which tend to result in unreliable or undesirable mechanical, swelling, and mass transport behavior.[21] Depending on the monomers chosen, relative volume fractions, and molecular weight of the blocks in the BCP, enthalpic and entropic forces compete to produce the

lowest free energy morphology possible. The competition can be quantified by the degree of segregation χN, where χ is the Flory-Huggins interaction parameter and N is the segmental volume of a chosen repeat unit. A large enough value of χN indicates that it is energetically favorable to microphase separate into the ordered state morphology. **Figure 2.1** is a theoretical phase diagram adapted from Cochran et al. for an AB BCP system, where AB represents a linear block copolymer comprising polymer A covalently bound to polymer B.[22-24] The phase diagram gives χN of the AB BCP as a function of the block volume fraction (*f*) for a generic BCP, showing morphologies favored at various combinations of χN and *f*. BCP phase behavior depends first on determining if it is energetically favorable for the polymer blocks to phase separate, and to subsequently find the most energetically favorable interfacial geometry (morphology) to balance contributions from interfacial contact and individual chain stretching penalties.[25]

(a)　　　　　　　　　　　　　　　　　　　　　(b)
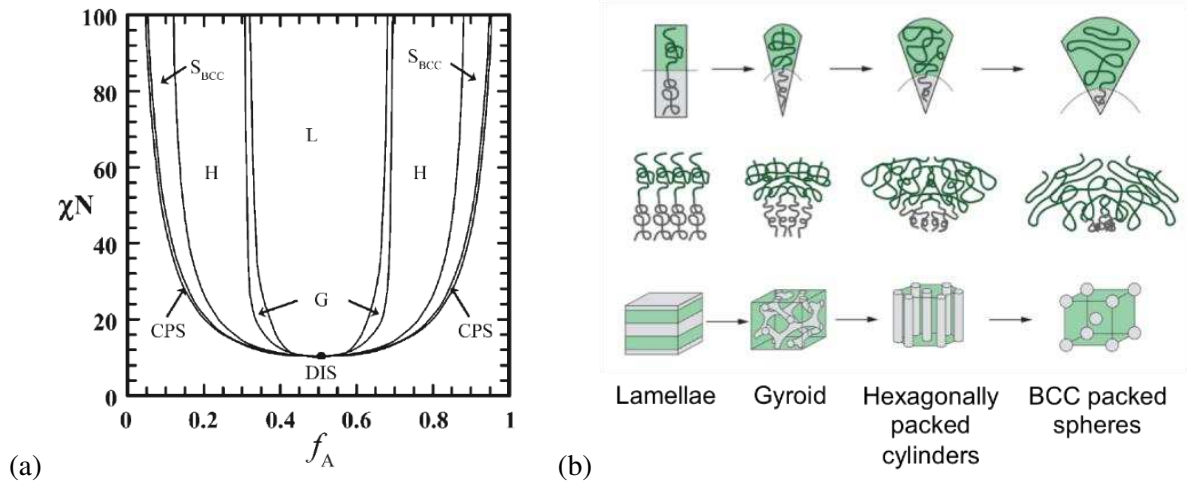
Figure 2.1.[24] **(a)** Phase diagram of a generic BCP system for various morphologies of the degree of segregation χN as a function of the volume fraction *f* of block A, where DIS is disordered (χN <10.495 for *f*=0.5), CPS is spherical phases with close-packed (face-centered cubic or hexagonal) symmetry, L is lamellae, G is double gyroid, and S_{BCC} is body-centered cubic (BCC)

spheres. **(b)** Physical representation of these anticipated morphologies is shown based on BCP volume fraction.

In 2010, our group published a study revealing a tough, thermally processable, physically crosslinked hydrogel capable of elastic recovery termed TPE hydrogels.[26] These materials required a relatively simple fabrication process, and were capable of being mechanically and chemically tailored to particular end uses, exhibiting excellent fatigue resistance as well as the capability to effectively absorb energy without failure, a large shift from traditionally brittle hydrogels. The two-component blends of polystyrene-*b*-poly(ethylene oxide) (PS-*b*-PEO-OH or SO-OH) and polystyrene-*b*-poly(ethylene oxide)-*b*-polystyrene (PS-*b*-PEO-*b*-PS or SOS) BCPs were designed to thermodynamically favor self-assembly into tethered spherical micelle-like aggregates with hydrophobic PS cores and hydrophilic PEO coronas, tethered with the shared midblocks of SOS triblock copolymer (**Figure 2.2**). In order to achieve this desired geometry, the BCP was synthesized such that the PS volume fraction fell within the range of access to the S_{BCC} morphology (f_{PS} = 0.9-0.13). The combination of this required high asymmetry, moderate χ values based on interactions of PS and PEO,[26] and for PS to remain glassy under conditions of swollen hydrogel use, a high molecular weight BCP was required. However, this had to be balanced against the kinetic limitations to self-assembly intrinsic to large molecular weight chains. Careful design of the resulting SO (f_{PS} = 0.10, $M_{n,SO}$ = 91450 g mol^{-1}) resulted in achievement of this delicate balance. A portion of this SO was then coupled using dibromoxylene (DBX) to form the symmetrical SOS triblock copolymer, which upon melt-state self-assembly provided the tethering PEO midblocks between adjacent micelle[26] spheres. When cooled, both nanoscale and macroscale structure were preserved through physical vitrification[18, 26, 27] of the hydrophobic PS core domains prior to preferential swelling of the surrounding

10

hydrophilic matrix. After introduction to water, these tethered networks adopted equilibrium dimensions from the balance of osmotic swelling forces from the entering water against entropic resistance to stretching intrinsic to the tethering and entangled PEO midblocks, acting to restrict expansion. The resulting hydrogel networks preserved the macroscopic shape adopted during melt-processing, and were highly elastic. This elasticity was a product of the homogeneously distributed, vitrified PS cores serving as physical junctions of the highly entangled tethered and dangling PEO chains. This resulted in a polymer matrix capable of distributing stress throughout the entire network, allowing for recovery without failure after tensile stressing.[26]
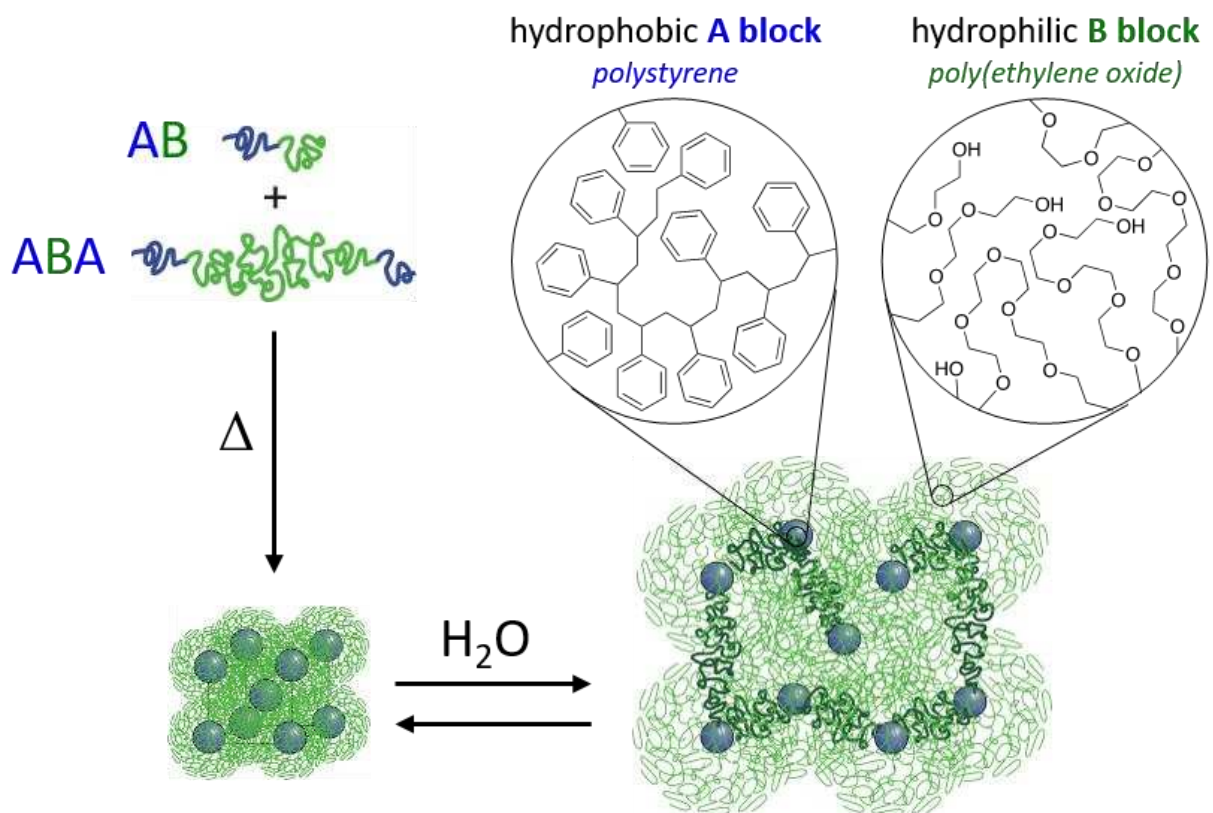
Figure 2.2. Generalized depiction of a two-component TPE hydrogel system based on AB diblock and ABA triblock copolymer blends designed to self-assemble into a lattice of tethered micelles. The magnified regions depict the composition of the hydrophobic core (polystyrene A block) and hydrophilic coronal layer (poly(ethylene oxide) B block).

These networks could be mechanically tuned using the concentration[18, 26] or length[27] of SOS triblock copolymers, as mechanical response is determined not only by integrity of the micellar core, but also the degree of coronal overlap which largely dictates the elastic behavior of the system.[27] This versatility recommends the use of TPE hydrogels as attractive options for a large range of applications in which an elastic, porous hydrogel material would be necessary.

2.2 Incorporation and advantages of a secondary network in TPE hydrogels

Since this foundational study, our group has made efforts to further improve and refine the mechanical capabilities of these TPE hydrogels.[18, 26, 27] These SO-based systems contain a high density of hydroxyl terminals in the corona of each micelle aggregate, a direct way to incorporate functionality into theses corona and the resulting hydrogel. Another study from our group exploited these modifiable hydroxyl terminals by using azide/alkyne click chemistry to install a secondary network of SOS triblock copolymer while the hydrogel was in the swollen state, effectively increasing toughness of the hydrogels in a similar manner to DN hydrogels, albeit with the added benefit of fatigue resistance. This extended the TPE hydrogel's potential applicability to areas in which such toughening and extensibility is desired.[18] Though this and other methods produced mechanically tunable hydrogels, they require the use of metal and small-molecule catalysts, which if left unremoved render them unsuitable for use in biological environments.[28, 29] While others have designed and exploited click style reactions without metal catalysts,[30] these strategies often involve complex organic syntheses or coupling requiring activation via ring strain.[31, 32] The following section discusses our intention to develop a way to access this tunability while combatting limitations of the click strategies, presents a system in which the hydrogel is easily fabricated without residual small-molecules, and retains the valuable features of the TPE hydrogel construct for a variety of biomedical applications.

2.3 UV tunability of TPE hydrogels

The objective behind developing this system was to simplify our traditional SO/SOS two-component approach to one in which the blend composition could be adjusted *in situ*, without addition of the tethering SOS prior to melt processing. UV irradiation was initially considered as an attractive option for material property adjustment due to the ability to use it to affect materials

in situ. Incorporation of a photo-mediated connectivity in the micelle-based network would introduce an externally controlled handle to deliberately affect physiochemical properties of the network. The use of light as a stimulus is attractive in contrast to other stimuli (such as pH), which are often passively triggered by local environmental changes rather than deliberately and directedly applied as irradiation would be.[33] Prior work has demonstrated its effectiveness for construction of tailored, highly connected polymeric networks,[34-36] though many of these photoactive fabrication strategies involve photoinitiated radical polymerizations which involve small molecule initiators and byproducts. A way around this is to exploit photodimerizable groups at polymeric chain ends, which would theoretically allow for chain-end coupling in situ upon application of light. Our strategy exploits photodimerizable anthracene groups which have proven to be significantly more stable than other photodimerizable molecules such as cinnimates or coumarin,[33] which can also yield low photocoupling efficiencies and limited reversible dimerization.[33] In this work, the terminus of the SO diblock copolymer chain is functionalized with anthracene via the hydroxyl end-group to form SO-anth. Melt-state self-assembly of this BCP results in formation of photoactive micelles, which allows us to exploit anthracene's photoinduced reversible 4 + 4]cycloaddition ($\lambda = 365$ nm) (**Figure 2.3**)[37] when the chain ends are mobile, and subsequently tether spherical domains through symmetric SOS triblock copolymer formation *in situ*. This strategy eliminates the need to pre-bend the SOS triblock copolymer prior to thermal processing/self-assembly.

14
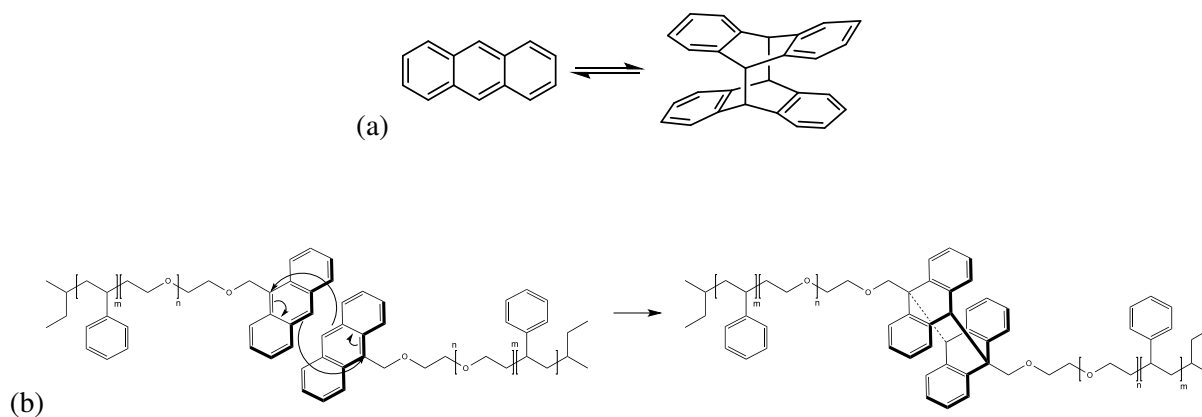
Figure 2.3. Reversible photoinduced [4+4]cycloaddition of **(a)** anthracene and **(b)** anthracene as a terminal substituent of SO diblock copolymer, used to couple SO to form symmetric SOS triblock copolymer under 365 nm irradiation.

A number of groups have utilized anthracene for its high efficiency photocoupling capabilities, stability, and reversibility, many using polyether-based hydrogels[33, 38-40] in which polymers were chemically cross-linked using photoinduced anthracene dimerization. However, unlike these chemically fixed systems, the SO-anth block copolymer systems developed here intrinsically retain the processability of traditional thermoplastics, even after UV exposure. The ability to install tethering triblock copolymer at any point following self-assembly in the melt introduces a new level of control to our TPE hydrogel construct. The work in this dissertation focuses primarily on development and utilization of this photoactive polymer construct towards hydrogel formation, exploring the material's versatility with respect to potential applications ranging from soft tissue repair, to dermal patches, to separation membranes. Discussion on the use of anthracene to affect material properties in the melt (**Ch. 3**), exploiting reversibility of anthracene on BCPs (**Ch. 4**), solution-based photocoupling approaches (**Ch. 5**), and photopatterning (**Ch. 6**)

are described within the indicated chapters, with corresponding publications indicated at the

beginning of each chapter.

References

1.	Calo, E.; Khutoryanskiy, V. V. Biomedical applications of hydrogels: A review of patents and commercial products. *Eur. Polym. J.* **2015,** 65, 252-267.

2.	Chen, Q.; Chen, H.; Zhu, L.; Zheng, J. Fundamentals of double network hydrogels. *J Mater Chem B* **2015,** 3, (18), 3654-3676.

3.	Lloyd, A. W.; Faragher, R. G. A.; Denyer, S. P. Ocular biomaterials and implants. *Biomaterials* **2001,** 22, (8), 769-785.

4.	Murphy, P. S.; Evans, G. R. Advances in wound healing: a review of current wound healing products. *Plastic surgery international* **2012,** 2012, 190436.

5.	Hoare, T. R.; Kohane, D. S. Hydrogels in drug delivery: Progress and challenges. *Polymer* **2008,** 49, (8), 1993-2007.

6.	Drury, J. L.; Mooney, D. J. Hydrogels for tissue engineering: scaffold design variables and applications. *Biomaterials* **2003,** 24, (24), 4337-4351.

7.	Suzuki, A.; Tanaka, T. Phase-Transition in Polymer Gels Induced by Visible-Light. *Nature* **1990,** 346, (6282), 345-347.

8.	Omidian, H.; Rocca, J. G.; Park, K. Advances in superporous hydrogels. *J. Controlled Release* **2005,** 102, (1), 3-12.

9.	Ashley, G. W.; Henise, J.; Reid, R.; Santi, D. V. Hydrogel drug delivery system with predictable and tunable drug release and degradation rates. *P Natl Acad Sci USA* **2013,** 110, (6), 2318-2323.

10.	Long, R.; Hui, C. Y. Fracture toughness of hydrogels: measurement and interpretation. *Soft Matter* **2016,** 12, (39), 8069-8086.

11.	Sun, J. Y.; Zhao, X. H.; Illeperuma, W. R. K.; Chaudhuri, O.; Oh, K. H.; Mooney, D. J.; Vlassak, J. J.; Suo, Z. G. Highly stretchable and tough hydrogels. *Nature* **2012,** 489, (7414), 133-136.

12.	Calvert, P. Hydrogels for Soft Machines. *Adv. Mater.* **2009,** 21, (7), 743-756.

13.   Ahmed, S.; Nakajima, T.; Kurokawa, T.; Haque, M. A.; Gong, J. P. Brittle-ductile transition of double network hydrogels: Mechanical balance of two networks as the key factor. *Polymer* **2014,** 55, (3), 914-923.

14.   Nonoyama, T.; Gong, J. P. Double-network hydrogel and its potential biomedical application: A review. *P I Mech Eng H* **2015,** 229, (12), 853-863.

15.   Gong, J. P. Why are double network hydrogels so tough? *Soft Matter* **2010,** 6, (12), 2583-2590.

16.   Gong, J. P.; Katsuyama, Y.; Kurokawa, T.; Osada, Y. Double-network hydrogels with extremely high mechanical strength. *Adv. Mater.* **2003,** 15, (14), 1155-+.

17.   Simha, N. K.; Carlson, C. S.; Lewis, J. L. Evaluation of fracture toughness of cartilage by micropenetration. *J Mater Sci-Mater M* **2004,** 15, (5), 631-639.

18.   Guo, C.; Lewis, J. T.; Scalfani, V. F.; Schwartz, M. M.; Bailey, T. S. Dangling-End Double Networks: Tapping Hidden Toughness in Highly Swollen Thermoplastic Elastomer Hydrogels. *Chem. Mater.* **2016,** 28, (6), 1678-1690.

19.   Bates, F. S. Polymer-Polymer Phase Behavior. *Science* **1991,** 251, (4996), 898-905.

20.   Bates, F. S.; Fredrickson, G. H. Block Copolymers: Designer Soft Materials. *Phys.Today* **1999,** 52, 32-38.

21.   Slaughter, B. V.; Khurshid, S. S.; Fisher, O. Z.; Khademhosseini, A.; Peppas, N. A. Hydrogels in Regenerative Medicine. *Adv. Mater.* **2009,** 21, 3307-3329.

22.   Bates, F. S.; Fredrickson, G. H. Block Copolymer Thermodynamics - Theory and Experiment. *Annu. Rev. Phys. Chem.* **1990,** 41, 525-557.

23.   Hiemenz, P. C.; Lodge, T., *Polymer Chemistry*. 2nd ed.; 2007.

24.   Cochran, E. W.; Garcia-Cervera, C. J.; Fredrickson, G. H. Stability of the gyroid phase in diblock copolymers at strong segregation. *Macromolecules* **2006,** 39, (7), 2449-2451.

25.   Scalfani, V. F. Part I — Access to UV Photocured Nanostructures via Selective Morphological Trapping of Block Copolymer Melts. Part II — Morphological Phase Behavior of Poly(RTIL) Containing Block Copolymer Melts. Ph.D. Dissertation, Colorado State University, Fort Collins, Colorado, 2012.

26.   Guo, C.; Bailey, T. S. Highly distensible nanostructured elastic hydrogels from AB diblock and ABA triblock copolymer melt blends. *Soft Matter* **2010,** 6, (19), 4807-4818.

27.   Guo, C.; Bailey, T. S. Tailoring mechanical response through coronal layer overlap in tethered micelle hydrogel networks. *Soft Matter* **2015,** 11, (37), 7345-7355.

28.   Yoon, J. A.; Bencherif, S. A.; Aksak, B.; Kim, E. K.; Kowalewski, T.; Oh, J. K.; Matyjaszewski, K. Thermoresponsive Hydrogel Scaffolds with Tailored Hydrophilic Pores. *Chem-Asian J* **2011,** 6, (1), 128-136.

29.   Yoon, J. A.; Oh, J. K.; Bencherif, S. A.; Kowalewski, T.; Matyjaszewski, K. POLY 29-Preparation of porous hydrogels by ATRP in the presence of star-branched polymers. *Abstr Pap Am Chem S* **2009,** 238.

30.   Becer, C. R.; Hoogenboom, R.; Schubert, U. S. Click Chemistry beyond Metal-Catalyzed Cycloaddition. *Angew Chem Int Edit* **2009,** 48, (27), 4900-4908.

31.   Kharkar, P. M.; Kiick, K. L.; Kloxin, A. M. Designing degradable hydrogels for orthogonal control of cell microenvironments. *Chem. Soc. Rev.* **2013,** 42, (17), 7335-7372.

32.   Ning, X. H.; Guo, J.; Wolfert, M. A.; Boons, G. J. Visualizing metabolically labeled glycoconjugates of living cells by copper-free and fast huisgen cycloadditions. *Angew Chem Int Edit* **2008,** 47, (12), 2253-2255.

33.   Zheng, Y.; Micic, M.; Mello, S. V.; Mabrouki, M.; Andreopoulos, F. M.; Konka, V.; Pham, S. M.; Leblanc, R. M. PEG-Based Hydrogel Synthesis via the Photodimerization of Anthracene Groups. *Macromolecules* **2002,** 35, (13), 5228-5234.

34.   Jo, S.; Shin, H.; Shung, A. K.; Fisher, J. P.; Mikos, A. G. Synthesis and characterization of oligo(poly(ethylene glycol) fumarate) macromer. *Macromolecules* **2001,** 34, (9), 2839-2844.

35.   Giammona, G.; Pitarresi, G.; Cavallaro, G.; Buscemi, S.; Saiano, F. New biodegradable hydrogels based on a photocrosslinkable modified polyaspartamide: synthesis and characterization. *Bba-Gen Subjects* **1999,** 1428, (1), 29-38.

36.   Andreopoulos, F. M.; Deible, C. R.; Stauffer, M. T.; Weber, S. G.; Wagner, W. R.; Beckman, E. J.; Russell, A. J. Photoscissable hydrogel synthesis via rapid photopolymerization of novel PEG-based polymers in the absence of photoinitiators. *J. Am. Chem. Soc.* **1996,** 118, (26), 6235-6240.

37.   Becker, H. D. Unimolecular photochemistry of anthracenes. *Chem. Rev.* **1993,** 93, (1), 145-172.

38.   Froimowicz, P.; Frey, H.; Landfester, K. Towards the Generation of Self-Healing Materials by Means of a Reversible Photo-induced Approach. *Macromol. Rapid Commun.* **2011,** 32, (5), 468-473.

39.   Wells, L. A.; Brook, M. A.; Sheardown, H. Generic, Anthracene-Based Hydrogel Crosslinkers for Photo-controllable Drug Delivery. *Macromol Biosci* **2011,** 11, (7), 988-998.

40.   Wells, L. A.; Furukawa, S.; Sheardown, H. Photoresponsive PEG-Anthracene Grafted Hyaluronan as a Controlled-Delivery Biomaterial. *Biomacromolecules* **2011,** 12, (4), 923-932.

Chapter 3.

Phototunable Thermoplastic Elastomer Hydrogel Networks

3.1 Summary

Thermoplastic elastomer hydrogel networks, based on swelling of nanostructured blends of amphiphilic, sphere-forming AB diblock and ABA triblock copolymers, provide direct access to thermally processable plastics that exhibit exceptional elastic recovery and fatigue resistance even after hydration. In such two component systems, the ratio of ABA triblock copolymer to AB diblock copolymer is used to control the resultant swelling ratio, system modulus, and overall mechanical response. In this report, we introduce a simplified one-component alternative which exploits a single component, photoreactive AB diblock copolymer precursor to controllably generate ABA triblock copolymer *in situ* during melt-processing. This was accomplished using efficient photoinduced [4 + 4]cycloaddition (λ = 365 nm) between terminal anthracene units on a ω-anthracenylpolystyrene-*b*-poly(ethylene oxide) diblock copolymer precursor (SO-anth, f_{PS} = 0.13, M_n = 70100 g mol^{-1}) to produce the desired amount of polystyrene-*b*-poly(ethylene oxide)-*b*-polystyrene (SOS) triblock copolymer. The amount of SOS triblock copolymer formed was tunable (from 11.7 to 45 mol%) using UV exposure time (2 to 20 min, ~30 mW cm^{-2}), giving direct control over swelling and mechanical properties in the resultant hydrogels produced upon subsequent vitrification of the melt-sample followed by addition of water. Hydrogels produced in this manner were found to exhibit dynamic shear

moduli and shape preservation characteristics typical of preblended, two component SO/SOS TPE hydrogels of similar SOS concentrations.

3.2   Introduction

Hydrogel networks[1-3] are of broad scientific interest due to their utility and compatibility in a variety of applications including tissue scaffolds,[4-8] encapsulation matrices,[9, 10] delivery agents,[11, 12] and separation membranes.[13-15] Numerous successful methods to produce hydrogel networks have been reported, generally exploiting physical or chemical cross-linking of hydrophilic polymers and monomers in solution.[1] However, conventional systems like these based on spatially random or statistical cross-linking mechanisms can suffer from weakly defined network structures with a large distribution of mesh sizes arising from the random nature of the cross-linking process. Heterogeneity in structure and mesh size across the sample profile can result in spatial inconsistencies in mechanical properties, swelling, and mass transport within the hydrogel.[2]

One strategy to overcome the nonuniformity intrinsic to solution-based network formation is to exploit melt-state self-assembly processes that produce periodic network structures.[16-22] Block copolymers (BCPs) are ideal candidates for spatially uniform network formation due to their inherent ability to form periodic structures on the nanometer length scale through thermodynamically driven phase separation of dissimilar blocks.[19, 23] Relative volume fractions of the constituent blocks and their connective architecture dictate a preferred interfacial curvature for each specific system, resulting in a diverse range of network structures. One interesting network subclass involves BCP-based thermoplastic elastomers (TPEs), in which triblock or multiblock copolymer architectures[24] are used to provide mechanical connectivity among

isolated domains in the system. Our group has recently developed a class of swollen TPE networks[25] and hydrogels[26-29] based on self-assembled blends of AB diblock and ABA triblock copolymers that adopt the sphere morphology in the melt state (**Figure 3.1**). This use of AB diblock with ABA triblock copolymer creates a periodic network of densely packed spherical aggregates in which the amount of ABA triblock copolymer can be used to set the concentration of bridging tethers between spheres. Integrity and preservation of both nano- and macroscale structure can be achieved through either physical vitrification[26-28] or chemical cross-linking[29-31] of the hydrophobic core domains (A blocks) prior to preferential swelling of the surrounding hydrophilic matrix (B blocks). Upon swelling, such tethered networks adopt equilibrium dimensions that are determined by a balance of osmotic swelling forces, entropic resistance to stretching intrinsic to the tethering midblocks, and topological entanglements among these tethers which act to further restrict expansion. We have found these hydrogel networks to exhibit highly elastic properties and complete preservation of the macroscopic shape imposed during melt-processing. Further, the hydrogel mechanical properties and mesh size are easily adjusted simply by changing the concentration of triblock copolymer[26, 28] or the length of triblock copolymer tether itself.[27] Interestingly, only a small percentage of triblock copolymer (~10 mol %) is necessary to produce hydrogels that are easily handled and exhibit excellent elasticity.[26, 29] Notably, hydrogel systems formed from blend compositions containing a majority of diblock relative to triblock copolymer contain a high density of hydroxyl end groups in the corona of each spherical aggregate; this provides a straightforward route to directly incorporate functionality within the interior of the hydrogel. In fact, we have recently used such functionality to enable *in situ* formation of a secondary network of tethers, providing dramatically improved toughness in highly swollen systems.[28]
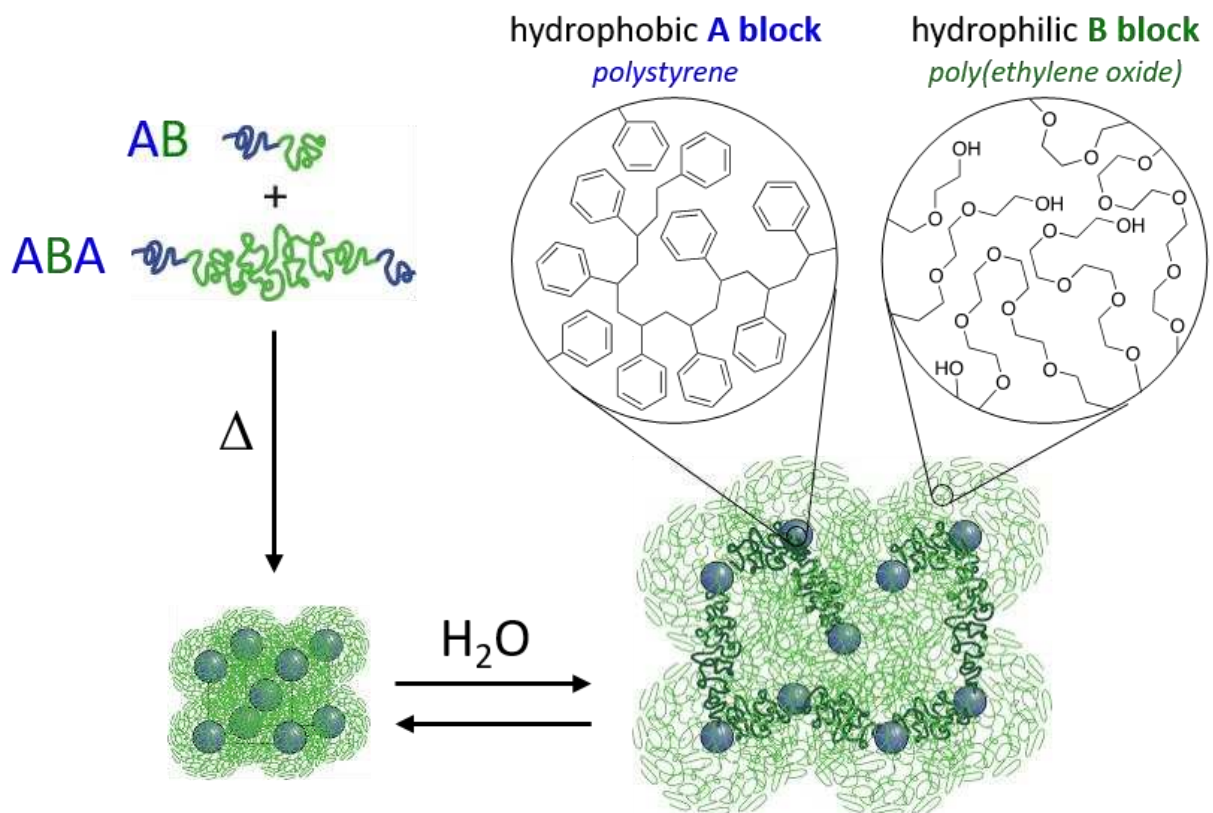
Figure 3.1. Generalized depiction of a two-component TPE hydrogel system based on AB diblock and ABA triblock copolymer blends designed to self-assemble into a lattice of tethered micelles. The magnified regions depict the composition of the core (polystyrene A block) and coronal (poly(ethylene oxide) B block) regions specific to this study.

The objective of this work was to simplify this two-component approach, in which the blend composition is used to tune mechanical properties of the hydrogel, and replace it with a single-component system in which UV irradiation can be used for mechanical property adjustment. The strategy is based on introducing a single AB diblock copolymer, namely poly(styrene)–*b*–poly(ethylene oxide) (SO), in which the coronal chain end has been functionalized with photodimerizable anthracene groups (SO-anth). UV exposure can then be used to induce chain end coupling through a [4 + 4] photocycloaddition between anthracene groups,[32] to form a

symmetric SOS triblock copolymer *in situ*. Anthracene dimerization thus acts to tether spherical domains through direct SOS triblock copolymer formation, eliminating the necessity to preblend the triblock copolymer prior to melt processing (**Figure 3.2**). In many ways, these systems share similarities with polyether-based hydrogels investigated previously by several groups,[33-36] in which hyperbranched[33], graft[34, 35] or star[36] architecture polyether-containing polymers were chemically cross-linked using photoinduced anthracene dimerization. However, unlike these chemically fixed systems, the SO-anth block copolymer systems developed here intrinsically retain the processability of traditional thermoplastics, even after UV exposure. Within, we evaluate the ability of these one-component systems to reproduce the elasticity and shape preservation (when swollen) intrinsic to their two-component analogues. Additionally, the mechanical performance of these UV-tethered TPE hydrogels is quantified and compared to that of the two-component systems, revealing the similarities and differences in behavior between the two uniquely formed, but topologically related, hydrogels.
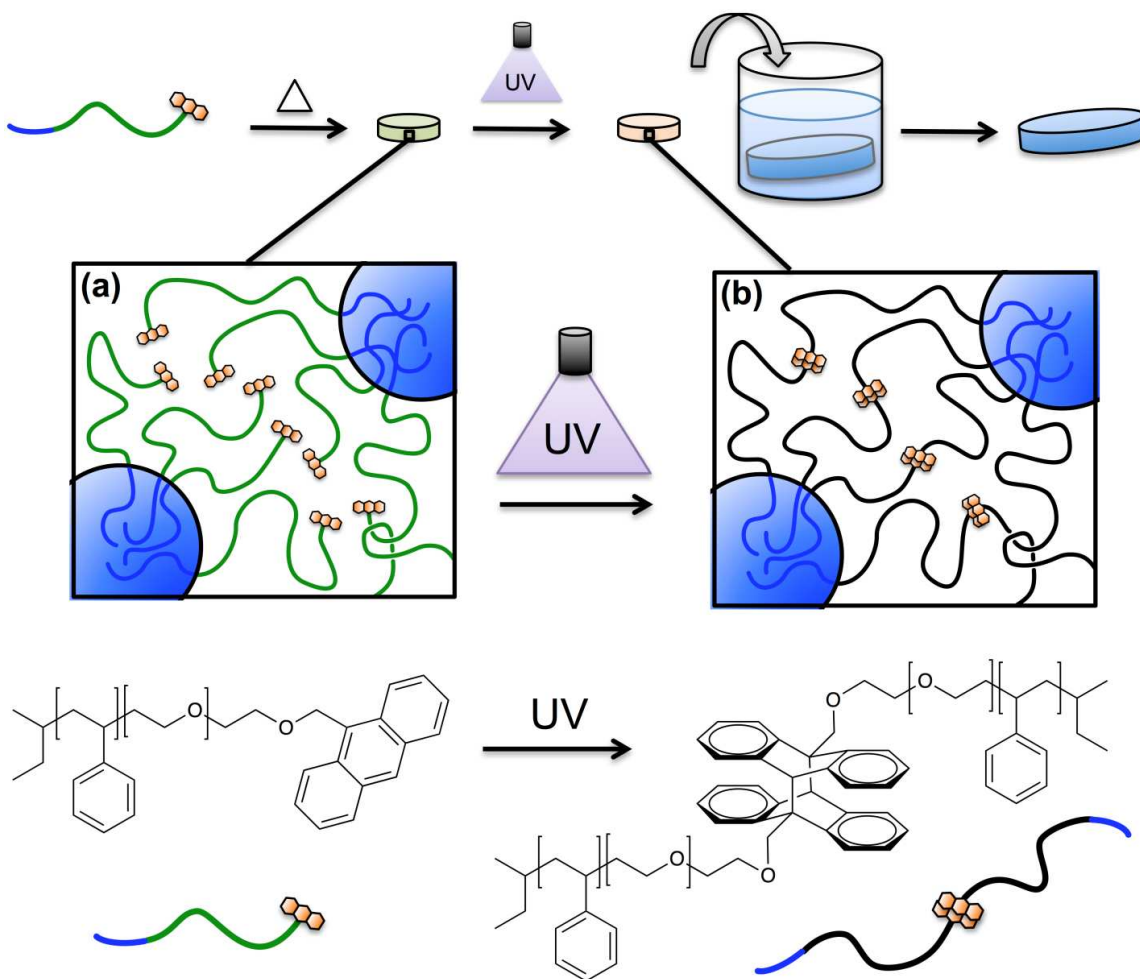
Figure 3.2. Schematic representation of the hydrogel fabrication process. **(a)** SO-anth self-assembles during melt-processing into preformed disks. **(b)** Those disks are then irradiated with UV light while still in the melt state, inducing chain end photocoupling through anthracene dimerization. Disks are then cooled and swollen in water to form the final hydrogel.

3.3 Results and Discussion

3.3.1 Synthesis and Material Characterization

This study involves a comparison of two hydrogel systems. One is based entirely on a single SO-anth diblock copolymer, and the other on blends of SO-OH diblock and SOS triblock copolymer. The synthesis of the SO-OH diblock copolymer (f_{PS} = 0.13, M_n = 70 100 g mol^{-1},

PDI = 1.05) was carried out using anionic polymerization techniques as described previously.[26] This hydroxyl-terminated SO block copolymer was then used as the precursor for both the SO-anth and SOS block copolymers used in the study.

End-functionalization of the SO with anthracene was accomplished through a straightforward nucleophilic substitution reaction with 9-chloromethyl anthracene.[31] The functionality of the end-tagging reaction with anthracene was approximately quantitative within the peak integration resolution of ^{1}H NMR (**Figure S3.1**). Analysis by size exclusion chromatography (SEC) confirmed the molecular weight distribution of SO-anth was nearly identical to the parent SO-OH with no evidence of any chain degradation or premature coupling (**Figure S3.1, inset**).

SOS triblock copolymer was produced similarly, through the slow introduction of a bifunctional halide (α,α'-dibromo-*p*-xylene) to the alkoxide form of the SO-OH diblock copolymer precursor. As reported previously by our group, typical coupling efficiencies for this large chain coupling reaction fall between 80 and 90%, with the balance comprised of unreacted SO-OH diblock copolymer. Preblended sample target compositions containing less SOS triblock copolymer than the product of the coupling reaction were prepared by solvent blending with supplementary SO-OH diblock copolymer precursor. This approach has been described in greater detail in a previous report.[26]

Hydrogel fabrication using the two-component system is achieved using three procedural steps. First, a composition of the SO-OH diblock and SOS triblock copolymer must be selected and homogeneously blended. This is followed by a thermal processing step required to achieve the targeted sphere morphology. Finally, water is introduced to the cooled sample to produce the hydrogel. Using this approach, the ratio of diblock and triblock copolymer fixed in the initial blending step determines the equilibrium water content and mechanical properties of the

27

system.[26, 27] In contrast, hydrogels formed by the one-component SO-anth diblock copolymer can be directly heated for self-assembly, and then irradiated with UV light to achieve any desired ratio of diblock and triblock copolymer, *in situ*. Once the polymer melt is vitrified, water can be introduced to form the hydrogel in the same way as the preblended two-component system.[31]

The selection of the SO-OH precursor molecular weight and composition was based on similar materials in our previous work, in which we explicitly confirmed the adoption of the sphere morphology during self-assembly using a combination of small-angle X-ray scattering (SAXS) model fitting and rheological data analysis. An important aspect of this work was to verify that the addition of anthracene to the SO chain end would not impact the self-assembly process. Indeed, strong interactions among integrated functional groups have been shown to strongly influence morphology, location of thermal transitions, and self-assembly kinetics in some cases.[29, 30, 37-42] In this case, however, the morphology of both SO-OH and its modified SO-anth counterpart was confirmed through a combination of dynamic rheology and SAXS. Both samples exhibited near identical melt-state phase behavior, with rheological and scattering signatures prototypical of a phase-separated sphere morphology with liquid-like packing (LLP) (**Figure 3.3**).[26, 43-46] Isochronal heating under oscillatory shear revealed a steady decrease in moduli upon heating with a larger loss modulus (G'') compared to the elastic modulus (G'). This behavior is characteristic of viscoelastic materials with enhanced viscous liquid-like properties. The absence of a plateau response of the moduli and presence of a gradual transition to the disordered state with increased heating is consistent with spherical morphologies with LLP.[26, 43] SAXS data (100 °C) for both SO-OH and SO-anth show primary scattering reflections at 0.0226 Å^{-1} and 0.0230 Å^{-1}, respectively, confirming the similarity of the domain spacing in the adopted LLP morphologies. Higher order reflections are absent or severely broadened which is also

consistent with phase separated morphologies exhibiting liquid-like packing,[43-46] a characteristic typical of sphere-forming SO-OH systems of similar molecular weight.[26-28]
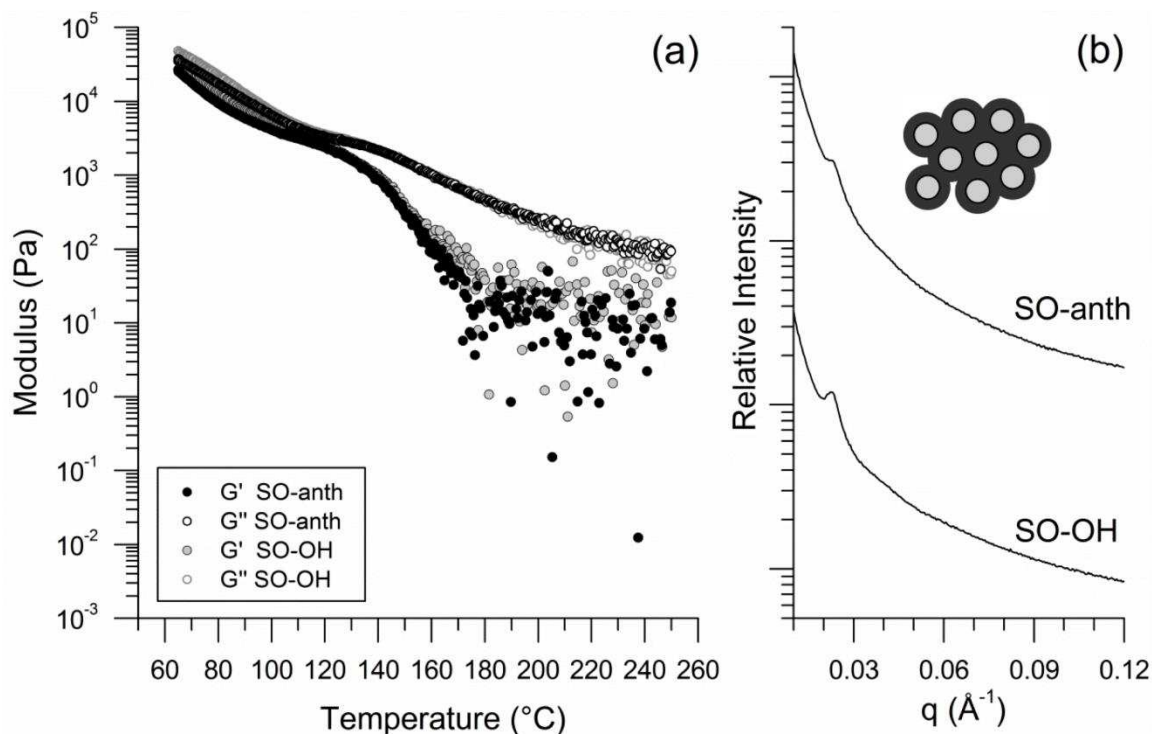
Figure 3.3. (a) Overlay of the rheological temperature ramps of SO-OH and SO-anth while heating at 1 °C min^{-1} with angular frequency of 1 rad s^{-1} and strain of 5%. The steady decrease in moduli and absence of a plateau region in G' are consistent with BCP melts containing a liquid-like packing of domains. (b) Azimuthally integrated SAXS data at 100 °C for PS–PEO and SO-anth. Higher order reflections are absent which is also characteristic of BCPs having LLP.

3.3.2   Network Installation through UV Photocoupling of SO-Anth in the Melt State

To begin the hydrogel fabrication process, preformed disk-shaped samples of SO-anth block copolymer were placed between surface-treated quartz coverslips or glass slides and heated to 150 °C to removal thermal stress. Samples were then cooled to 100°C and held in the melt state under argon during exposure to 365 nm UV light (see **Figure 3.5b-c**). Disks were flipped over

halfway through targeted coupling times to ensure axially symmetric exposure. Installed triblock copolymer was correlated with UV exposure time using SEC as depicted in **Figure 3.4**. SEC data confirmed increasing concentrations of SOS triblock copolymer (from 11.7 to 45.0 mol %) were produced with increasing UV exposure times (from 2 to 20 min), with the balance being uncoupled SO-anth. Notably, a small but growing shoulder at early elution times indicated the development of high molecular weight species during UV exposure. This may be the result of trace amounts of oxygen-promoted radical coupling despite the use of an argon purge. Regardless, there is a clear and predictable relationship between exposure time and the amount of triblock copolymer formed. This rate is likely influenced by a combination of bimolecular kinetics, light intensity decay with sample depth, restricted chain-end mobility in the entangled melt, and spatially limited reaction volumes due to chain anchoring within the nanostructure. In theory, the coupling rate should still also be tunable using the intensity of the incident light used, although that aspect was not investigated in these initial studies. Importantly, this ability to precisely control the relative amounts of diblock and triblock copolymer with UV light alone greatly simplifies the fabrication protocol; that is, the single parent SO-anth BCP can be used to produce hydrogels with a diverse range tethering densities. A comparison of the LLP morphology (via SAXS model fits, see Supporting Information **Figure S3.2** and **Table S3.1**) between systems in which the SOS triblock copolymer was preblended and those in which it was installed through UV-induced chain coupling (as confirmed by SEC in **Figure S3.3**) showed no observable differences, indicating a negligible impact of the UV exposure on the spatial organization of the self-assembled nanostructure.

This system utilizing anthracene coupling in the neat melt phase with a BCP of about 70 kDa (very low concentration of end-groups) appears to be controlled and rapid, producing a wide

range of coupling efficiencies in less than 25 minutes. Coupling reactions of polymer-bound functional groups in the melt have been reported previously,[47-49] and can be very fast and efficient in both miscible[48] and immiscible[47] polymer systems if the reactivities of those groups are extremely high (e.g, between anhydride and amine groups). In cases where reactivities are more moderate, the preorganization afforded by directed assembly can enhance coupling or polymerization efficiencies.[28-30, 50] In our case, we suspect the micelle-like domain structure (which radially directs the PEO chains toward centralized regions of the matrix), in combination with preferential π-π stacking among terminal anthracene groups, act to enhance coupling efficiency in these otherwise dilute systems. To our knowledge, however, there is only one prior report by Russell and co-workers in which anthracene was used to form UV photocoupled BCP in the melt.[51] Notably, we have had past success with UV cationic cross-linking of partially epoxidized poly(diene)-based BCPs over a diverse set of melt morphologies[29, 30] and speculate UV induced photocoupling in the melt state could also be applied in self-assembled BCP structures beyond the LLP spheres employed here. Importantly, the UV photocoupled systems remain processable thermoplastics even after irradiation, being comprised only of SO diblock and photocoupled SOS triblock copolymer species.
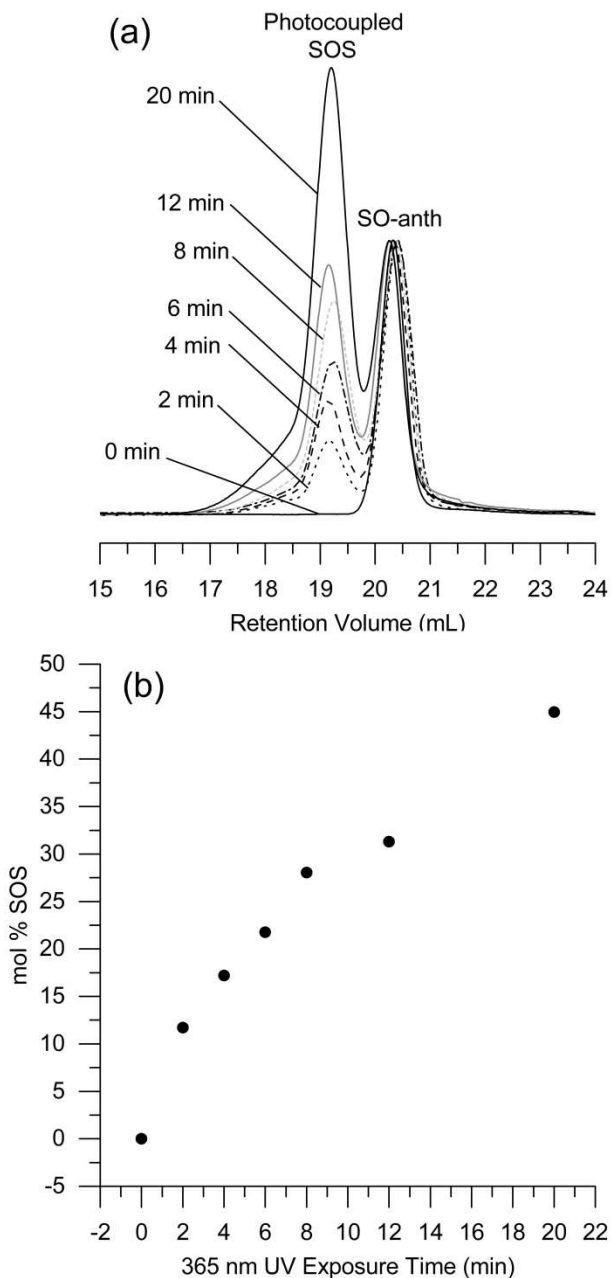
Figure 3.4. **(a)** SEC traces of SO-anth samples that have been photocoupled with 365 nm UV filtered light at 100 °C for 0–20 min. **(b)** Concentration of photocoupled PS–PEO–PS triblock copolymer is correlated with UV irradiation time.

Despite the excellent control UV irradiation affords, there appears to be a limitation in the maximum amount of triblock copolymer that can be installed under the conditions used. After

roughly 20 min of UV exposure, the concentration of triblock copolymer appears to reach a maximum (in this case near 45 mol% SOS). ^{1}H NMR curiously shows that by this point most anthracene units have been dimerized. However, this fails to be reflected in the amount of triblock copolymer indicated by the SEC data. We speculate this apparent discrepancy is the result of UV-promoted radical cleavage of the anthracene functional unit from the PEO chain end, which depletes the level of triblock copolymer achievable by the system. Notably, cleavage could be occurring prior to during, or following the cycloaddition reaction. This hypothesis is consistent with the retention of the distinct and narrow triblock and diblock copolymer molecular weight distributions in the SEC data. In addition, subsequent radical addition of these byproducts may explain the small high molecular weight shoulder discussed earlier. Finally, because of the absence of the distinct aromatic proton resonances associated with undimerized anthracene in the ^{1}H NMR at the point of maximum triblock copolymer concentration, heat or UV-induced retro-cycloaddition is not believed to be a contributor to the depletion of triblock copolymer in these systems.

3.3.3   Swelling Behavior of UV Photocoupled SO-Anth Hydrogels

Once UV exposure was complete and the triblock copolymer tethers were installed, the samples were simply cooled from the melt to resolidify the disks. When placed in DI water, these disks were observed to begin swelling immediately, forming hydrogels that reached equilibrium swelling in about 1–2 h (determined by constant mass and size). Preservation of shape upon swelling was observed (**Figure 3.5d**), as is characteristic of the two-component melt blends studied previously. In this case, some anisotropy in the swelling between the axial and radial directions was detected, suggesting a gradient in triblock copolymer concentration in the axial direction was present. However, flipping the disks over halfway through their full exposure time

ensured this gradient remained symmetric about the axial center. As the concentration of photocoupled triblock copolymer was increased, the amount of swelling decreased in the SO-anth derived hydrogels. Notably, this trend in swelling behavior mimics that of systems in which triblock copolymer was preblended in specific amounts (**Figure 3.5a**). In general, self-entanglements among tethers, which increase with increasing concentrations of triblock copolymer, act to restrict swelling. The amount of water absorbed, or swelling ratio (g H_2O per g dry polymer, Q), was tunable over the range of 5.7 – 19.2 depending on the concentration of photocoupled triblock copolymer present within the sample.
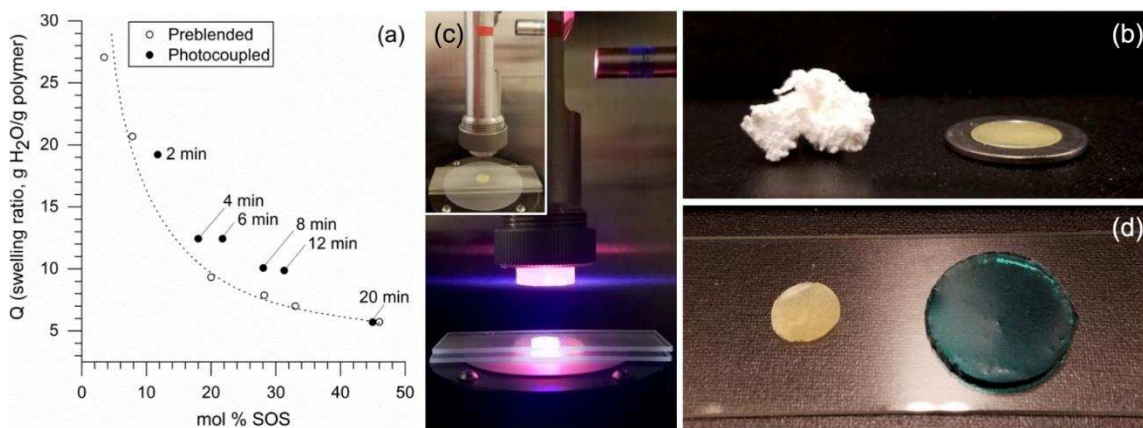
Figure 3.5. (a) Swelling ratios of preblended SO/SOS and photocoupled SO-anth hydrogels as a function of mol % triblock copolymer. In both systems, the swelling ratio (*Q*) could be controlled with concentration of triblock copolymer. The dashed line serves as a visual reference showing the typical swelling behavior of preblended two-component hydrogels as described previously. Adjacent images depict aspects of the hydrogel fabrication process. **(b)** Preformed disks were sandwiched between quartz glass slides and heated using a Peltier plate (inset). Heated samples were then irradiated with UV light (365 nm). **(c)** SO-anth as a powder and as a pressed disk following thermal processing using a circular mold. **(d)** Example of a UV-irradiated

sample before and after swelling in DI water (artificial color added for image contrast purposes only).

Q is about 20 % greater in the SO-anth derived hydrogels compared to the preblended hydrogels, save for the sample with the highest amount of triblock copolymer studied (45 mol %) where the swelling is nearly identical. In order for the SO-anth to photocouple with UV light, two anthracene functional chain ends must meet within a defined reaction volume in which one of the anthracene units is in a short-lived photoexcited state (nanoseconds).[52, 53] The probability of photocoupling increases with UV flux, and therefore coupling within the melt-disk (0.29 mm thick) will be most efficient at the surface and least efficient in the axial center due to being flipped over halfway through irradiation time. This depth-dependent photocoupling efficiency should inherently produce an axial gradient in triblock copolymer concentration with a minimum at the center of the vertical axis. The moderate swelling ratio increase exhibited in photocoupled hydrogels appears to be a direct result of greater swelling in this less densely tethered axial center.   This is in contrast to the preblended samples (regardless of thickness) for which a statistically homogeneous distribution of triblock copolymer produces homogeneous swelling throughout the entire depth of the hydrogel. Notably, there does appear to be a similarity in swelling between the sample with the longest exposure time (20 min, 45 mol % SOS) and its corresponding preblended sample, as mentioned earlier. It is hypothesized that as irradiation time increases, the gradient in tether concentration is diminished as total intensity required to maximize coupling conversion at each depth is reached. Interestingly, the ability to purposefully create an axial gradient of entanglements naturally produces a surface skin layer (tighter mesh size) while retaining a more porous subsurface region. In this way, our hydrogels intrinsically mimic the structure of phase inversion membranes in which such a skin layer is used to dictate

transport rates.[54-57] As such, the self-assembled SO-anth system may provide the foundation for an alternate class of block copolymer-based nanoporous materials[58-67]- one in which the concentration dependent mesh size produced by the installed triblock copolymer, rather than the void space produced by selectively etching away a specific block, is used to define the division of pore space in the system.

3.3.4   Mechanical Performance of UV Photocoupled SO-Anth Hydrogels

To compare the mechanical response of the one- and two- component systems, their behavior under dynamic shear and unconfined compression was examined. Dynamic frequency sweeps over a range of 0.1-100 rad s^{-1} yielded a plateau-like response in elastic modulus for all hydrogels in both systems. **Figure 3.6** contains the elastic moduli (G') at 1 rad s^{-1} extracted from these frequency sweeps, plotted as a function of mol % triblock copolymer. As the triblock copolymer concentration increases for both systems, the modulus also increases. This behavior has been shown to be a product of increased overlap among the individual micellar domains due to increasing entanglements in the tether population.[26, 27] However, it appears that installation of the triblock copolymer through anthracene photocoupling produces elastic moduli slightly lower than those obtained in preblended samples at similar triblock copolymer concentrations. This is consistent with the theory that the tether concentration in the axial center of the hydrogel is lower in photocoupled samples versus those that were preblended. Such a reduced tether concentration in the center is also consistent with the higher degree of swelling, and would translate mechanically as a softer, more deformable core under oscillatory shear. In contrast, the two-component TPE hydrogel, with a statistically homogenous distribution of triblock copolymer throughout, exhibits higher overall modulus values in shear. Of note, the sample with the highest concentration of photoinstalled triblock copolymer (45 mol %) exhibits a very similar elastic

36

modulus to the analogous preblended sample, consistent with the hypothesis that such a gradient is reduced at longer (over 12 min) UV exposure times.

Importantly, tunability in the triblock copolymer concentration using 365 nm light irradiation enables direct and facile control of hydrogel mechanical properties. That is, accessible exposure times (between 2 and 20 min) can produce elastic moduli spanning 2 orders of magnitude (10^3–10^5 Pa), a direct consequence of the ability to prescribe a chosen concentration of installed triblock copolymer.
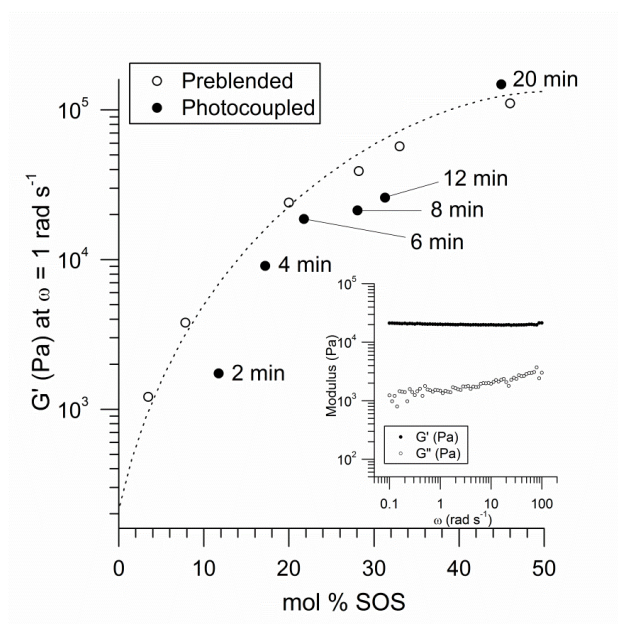
Figure 3.6. Elastic modulus of preblended SO/SOS and photocoupled SO-anth hydrogels taken at 1 rad s^{-1} from room temperature dynamic frequency sweeps performed over frequencies of 0.1 – 100 rad s^{-1} in the linear viscoelastic regime (ε = 0.1 - 1 %) The dashed line serves as a visual reference showing the typical elastic moduli of preblended two-component hydrogels. Inset: dynamic frequency sweep of SO-anth hydrogel that has been UV photocoupled for 8 min (28.1 mol % triblock copolymer). The plateau response is representative of these hydrogels at all triblock copolymer concentrations and prototypical of highly elastic solids.

The mechanical behavior of the photocoupled SO-anth hydrogels was further investigated by evaluating the stress-strain behavior under unconfined compression. Samples containing various installed triblock copolymer concentrations were compressed to 50% strain (2% s^{-1}) over two successive cycles as shown in **Figure 3.7**. In general, all samples showed a small degree of recoverable hysteresis upon removal of the stress, such that each second cycle replicates the initial stress-strain behavior nearly identically (**Figure 3.7** and **Figure S3.4**). The reproducibility demonstrated by the second cycle implies the origin of the hysteresis is from rate dependent elastic recovery, which is associated with diffusion limitations of the water distributed within the material and not any permanent network deformation or damage.[26] These results imply the photocoupled hydrogel systems may possess excellent fatigue resistance, a property observed to be characteristic of the preblended hydrogels in separate preliminary studies.
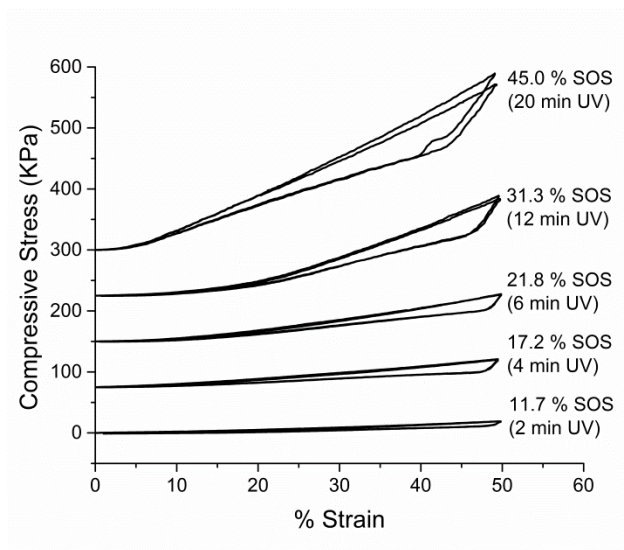
Figure 3.7. Compressive stress vs strain data for two complete compression cycles of photocoupled SO-anth hydrogels with varying installed triblock copolymer content, artificially spaced for visibility. Each curve is labeled with the mol % triblock copolymer and the associated UV exposure time.

An interesting feature of the compression data for the photocoupled samples is the distinct change in slope at a critical strain value for each sample. This change in slope defines a low-modulus toeing region at early strain values followed by a region of much stronger strain dependence (higher modulus). The strain range of this early toeing behavior clearly decreases with increasing triblock copolymer content. Again, it appears that there is a strong correlation between the strain range over which the sample is easily deformed and UV exposure time. The hypothesis that the lower concentration of tethering molecules at the axial center at shorter exposure times produces a softer core is consistent with this clear trend in toeing behavior under compressive strains. At the inflection point, the softer center region has been significantly compressed such that the material modulus begins to reflect that characteristic of the more densely tethered outer regions of the hydrogel. In agreement with this assertion is the clear correlation between increasing modulus and overall triblock copolymer content in this region. Notably, at short UV exposure times, the distinction between the two regions becomes difficult to discern due to the low overall triblock copolymer content at any depth in the sample.

To investigate that the reduced toeing region is in fact related to a diminished gradient in triblock copolymer concentration, these compression data were directly compared to preblended hydrogels in which the triblock copolymer distribution is statistically homogeneous. Toeing in such samples has been shown to be minimal.[26] To evaluate the difference in toeing behavior between these two systems, compression data for the samples at two similar concentrations of triblock copolymer are juxtaposed in **Figure 3.8**. The comparison immediately reveals that the homogeneous distribution of tethers in the preblended samples virtually eliminates the toeing behavior, with preblended samples adopting a constant modulus at much lower strain values than that of their photocoupled counterparts of similar triblock copolymer content.
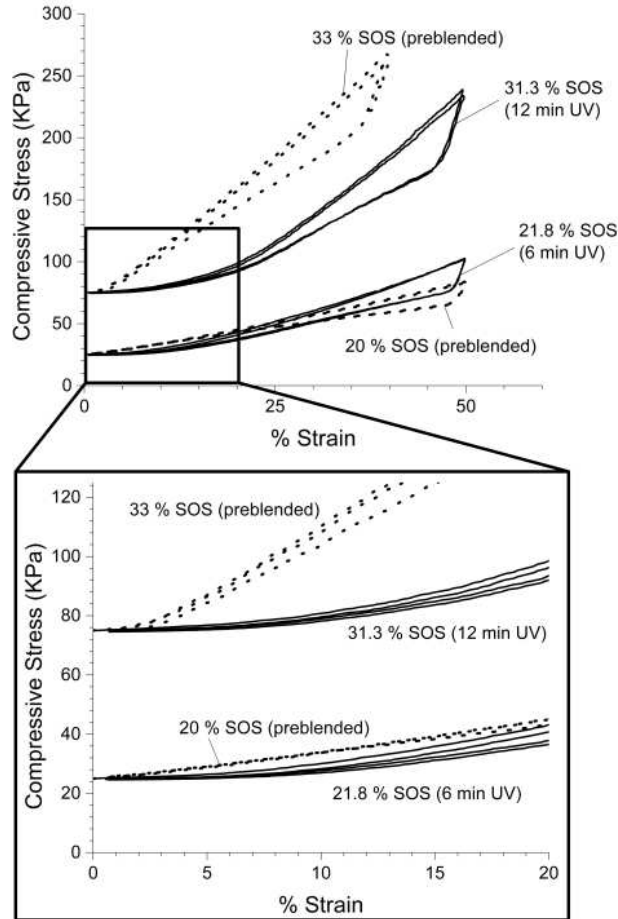
Figure 3.8. Comparisons of compressive stress vs. strain data between two sets of preblended and photocoupled samples of similar triblock content with an enlarged view of toeing region (artificially spaced along the y axis). Graduated installation of triblock copolymer through UV photocoupling allows for the integration of toeing behavior which is not possible in preblended systems due to homogeneously distributed tethering.

Figure 3.9 depicts the first cycle compressive moduli for both preblended and photocoupled hydrogels in the higher strain region as a function of the overall triblock copolymer content. This plot emphasizes two key distinctions between this pair of hydrogel systems. First, the average triblock copolymer content is ultimately a fairly good predictor of the higher-strain modulus in both materials. Second, the toeing region modulus of the photocoupled samples stays largely

independent of triblock copolymer content until higher triblock copolymer concentrations (therefore reduced axial gradients) are reached. Uniquely, the graduated distribution of tethers intrinsic to the UV installation mechanism provides a means of integrating toeing behavior that is otherwise absent from classic TPE hydrogel systems. Such toeing behavior is common in a range of hydrated soft tissues and a key characteristic often critical to their physiological function and biomechanical performance. As such, the integration of phototunability into this basic TPE hydrogel framework extends their current potential as important materials in soft tissue repair applications.
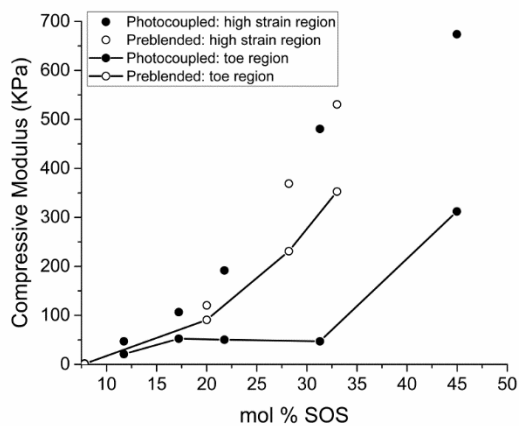
Figure 3.9. Comparison of compressive moduli between photocoupled and preblended gels as a function of triblock content in toe ($\varepsilon = 0 - 0.1$) and high strain ($\varepsilon = 0.2 - 0.3$) regions. Lines connecting toeing region data are added for clarity only.

3.4 Conclusions

In summary, a series of TPE hydrogels based on single component photoreactive block copolymers were fabricated. Samples of sphere-forming SO-anth diblock copolymer were melt-processed to provoke self-assembly, and then UV irradiated as viscous liquids in the melt phase.

The irradiation induces photodimerization of the terminal anthracene units, producing SOS triblock copolymer *in situ*. This new SOS population serves to tether adjacent hydrophobic PS domains, forming a mechanically robust hydrogel after sample vitrification and swelling in water. Through adjustment of UV irradiation time, the installed triblock copolymer concentration could be controlled, producing hydrogels in which the resultant water content and mechanical properties could be easily tuned. The properties of these one-component hydrogels were compared with two-component analogues as previously developed by our group,[26] in which predetermined amounts of triblock copolymer were preblended prior to melt processing. Hydrogels in which tethers were installed using UV irradiation exhibited swelling behavior and mechanical properties consistent with the presence of an axial gradient of triblock copolymer. Unlike preblended samples in which the concentration of triblock copolymer is largely homogeneous, the photocoupled SO-anth hydrogels exhibited slightly increased swelling and toeing behavior in compression, consistent with a softer axial center. However, high strain moduli displayed by the two systems were similar such that the overall triblock copolymer concentration was a good predictor of mechanical behavior in this regime, regardless of installation method (blending or *in situ* UV coupling). At long exposure times, triblock copolymer concentration in the photocoupled samples appears to approach a level of axial homogeneity inherent in the preblended samples, as evidenced by a convergence in mechanical and swelling behavior. Future investigations of the kinetics and spatial distribution of triblock copolymer may help elucidate the network intricacies of this unique hydrogel system.

3.5 Experimental

3.5.1 Materials and Methods

Styrene (99%, 50 ppm *p*-tert-butylcatechol inhibitor, Aldrich) was purified by static vacuum (15-30 mTorr) distillations from di-*n*-butylmagnesium (1.0 M in heptane, Aldrich) at 40 °C. Ethylene oxide (99.5+%, compressed gas, Aldrich) was purified by successive distillations from di-*n*-butylmagnesium (1.0 M in heptane, Aldrich) at 3 °C. *sec*-Butyllithium (1.3 M in cyclohexane/hexane, Fisher) was used as received. Potassium naphthalenide solution was prepared according to a previous report.[26] 9-(Chloromethyl)anthracene (98%, Aldrich) and α, α'-dibromo-*p*-xylene (97%, Aldrich) were dried under high vacuum for several hours prior to use. Tetrahydrofuran (THF) was degassed by sparging with argon (10 psi) for a period of 45 min and then purified over two molecular sieve columns of neutral alumina (Glass Contour, Inc.). Cyclohexane (CHX) was degassed with argon and purified through a column of neutral alumina followed by a column of Q5 copper (II) oxide catalyst (Glass Contour, Inc.). Hydrogels were swollen using DI water of 18.2 MΩ resistivity (Evoqua/U.S. Filter Service Deionization). Other common chemicals and solvents were used as received unless otherwise stated. Ultrahigh purity argon (99.998% Airgas) was passed through a column of 5 Å molecular sieves with drierite (Agilent) and oxygen-absorbing purifier column (Matheson Trigas). Glassware and polymerization reactors were flamed under vacuum and backfilled with argon (3x).

Synthesis of PS–PEO (SO) and PS–PEO–PS (SOS). Hydroxyl terminal polystyrene–*b*–poly(ethylene oxide) (PS–PEO, SO) was synthesized according to a previously reported procedure[26] using two-step anionic polymerization of styrene and ethylene oxide monomer. In brief, step one involved the synthesis of a hydroxyl-terminal polystyrene macroinitiator ($M_{n,PS}$ = 8390 g mol^{-1}, $M_{w,PS}/M_{n,PS}$ = 1.03, SEC (polystyrene standards)), from which the final SO-OH

diblock copolymer was produced. The volume fraction of the PS block in the final diblock copolymer was determined to be 0.13 (using nominal densities at 140 ˚C) [68] with an overall M_n = 70,100 g mol^{-1} ($M_{w,SO}/M_{n,SO}$ = 1.04, SEC (polystyrene standards)) calculated using the measured $M_{n,PS}$ and the relative ^{1}H NMR integrations. The synthesis of triblock PS–PEO–PS for the preblended samples was accomplished via coupling using α,ά-dibromo-*p*-xylene (1 equiv of PS–PEO: 0.5 equiv of α,α'-dibromo-p-xylene) according to previous reports.[26] In general, coupling reactions using α,α'-dibromo-*p*-xylene yield coupling efficiencies in the 70 - 90 mol % range, with the balance material being uncoupled SO-OH diblock copolymer.

Synthesis of PS-PEO-Anthracene (SO-Anth). PS–PEO (1.16 g, 0.017 mmol) was dissolved in 100 mL dry THF. The solution was slowly titrated with potassium naphthalenide such that the solution remained light green for at least 20 min. A large excess of 9-(chloromethyl)-anthracene (0.113 g, 0.5 mmol, 30x excess) was then immediately added to the PS–PEO alkoxide solution under a slight positive pressure of argon at room temperature. The solution was allowed to stir overnight under argon. The anthracene-terminated block copolymer product was precipitated from 25 °C pentane (1 L) twice. Filtration and drying in vacuo (25 °C, 24 h) gave the block copolymer as an off-white powder. Yield = 0.96 g (83 %). SEC (polystyrene standards): M_w/M_n = 1.04. ^{1}H NMR (400 MHz, CDCl$_3$, δ): 8.4–8.5 (m, anthracene H$_1$, H$_8$ and H$_{10}$), 7.9–8.0 (d, anthracene H$_4$ and H$_5$), 7.4–7.6 (m, anthracene H$_2$, H$_3$, H$_6$ and H$_7$), 6.2–7.2 (b, –CH$_2$–C(R)H–C$_6$H$_5$), 5.5 (s, –O–CH_2–anthracene), 3.4–3.8 (b, –CH_2–CH_2–O–), 1.1–2.3 (b, –CH_2–C(R)H–C$_6$H$_5$), 0.8–0.9 (b, CH$_3$–CH_2–C(R)H–CH$_3$), 0.5–0.7 (b, CH_3–CH$_2$–C(R)H–CH_3). See **Figure S3.1** for clarification of anthracene proton assignments. They are consistent with a previous report.[69] Relative integrations of anthracene to initiator protons suggest a quantitative addition within ^{1}H NMR integration error (~5%).

Preparation of Blended SO/SOS Samples. SO/SOS blends were produced by solution blending (0.2 g of total polymer per mL of $CHCl_3$ or benzene) the appropriate amounts of SO-OH diblock copolymer and the SOS coupling product to reach the specified molar concentrations of triblock copolymer. Solutions were made in small glass vials and frozen using an ethanol/liquid N_2 slush bath and then placed in vacuo (10–20 mTorr) at room temperature for at least 24 h. Removal of solvent was confirmed by ^{1}H NMR. The 8.14 mm diameter 0.29 mm thick disks were melt pressed (Carver Press) directly from powders using a stainless steel cutout sandwiched between Teflon covered Lapton sheets. Disks were held under a constant pressure of 500 psi at 150 °C for approximately 60 s, before being removed from the press and cooled (unassisted) to room temperature. The pressed polymer was easily removed from the stainless steel cutout to give homogeneous, slightly opaque (due to PEO crystallinity), disks. Disk dimensions (diameter and thickness) and dry weight were recorded for subsequent swelling experiments.

UV Photocoupling SO-Anth in the Melt Phase. SO-anth, used for the photocoupling experiments, was pressed as solid disks (8.14 x 0.29 mm, 150 °C, 500 psi for 60 s) and stored in the dark before use. The copolymer disk was sandwiched between two quarts coverslips (0.25 mm thickness). The quartz cover slips were pretreated in a solution with 10: 1 volumetric ratio of toluene:trimethylchlorosilane overnight prior to use to make the surface hydrophobic. Immediately before use, the quartz cover slips were rinsed with ethanol to remove any excess solution. The SO-anth disk sandwiched between the quartz slides were placed on a hot plate and heated to 150 °C for 1 min and cooled to 100 °C (5 min cooling time) under a purge of argon. A TA Instruments ARES quartz parallel plate with reflecting mirror tool was positioned approximately 1–2 mm above the surface of the sample. A Hamamatsu Lightning Cure LC8 UV spot cure system was utilized with a 200-Watt mercury-xenon lamp, Asahi Spectra Co high

45

transmission band pass 365nm filter, synthetic silica light guide and short focal point condenser lens. The light guide was positioned approximately 1 cm from the quartz reflecting mirror. The intensity at the surface of the sample was 30–38 mW cm^{-2} (measured in the range of 200–600 nm with an Omnicure R2000 radiometer). Samples were exposed to UV 365 nm filtered light for 2–20 min and flipped over halfway through the exposure time. The formed polymer was easily removed from the quartz coverslips to give homogeneous, slightly opaque (due to PEO crystallinity) disks. Disk dimensions (diameter and thickness) and dry weight were recorded for subsequent swelling experiments.

3.5.2 Measurements

^{1}H NMR spectra were recorded at room temperature on a Varian Inova 400 MHz spectrometer with a d1 pulse delay of 20 s to ensure complete relaxation of end-groups. Spectra were referenced to the residual protio solvent, CHCl$_3$. Size exclusion chromatography (SEC) spectra were collected on a Viscotek GPC-Max chromatography system outfitted with three 7.5 x 340 mm Polypore™ (Polymer Laboratories) columns in series, a Viscotek differential refractive index (RI) detector, and an Alltech column oven (mobile phase THF, 40 °C, 1 mL min^{-1}). Rheological melt experiments were run on a TA Instruments Advanced Rheometric Expansion System (ARES) rheometer. Copolymer samples for melt rheology were pressed as solid disks (8 x 1 mm, 150 °C, 500 psi for 60 s). Disks were positioned between two parallel plates (8 mm diameter). The rheometer parallel plates were heated to 75 °C and the gap was reduced and adjusted to ensure even distribution of the sample (typical gaps were 0.5–0.7 mm). Dynamic temperature ramp tests were performed while heating and cooling at 1 °C min^{-1} at angular frequency of 1 rad s^{-1} and a strain of 5 % (well within the linear viscoelastic regime, determined by dynamic strain sweep experiments for each copolymer). Rheological swollen hydrogel

frequency sweep and compression experiments were run at room temperature using an infinite stainless steel (63 mm) lower plate and an 8 mm stainless steel upper parallel plate. Before starting the rheological experiments, hydrogels were blotted dry with Kimwipes and humidity covers were placed over the water bath to prevent evaporation. A constant force was applied (10 % compression) to all hydrogel samples to prevent slip. Strain rates were adjusted depending on the linear viscoelastic regime (typically 0.1–1%). Small angle X-ray scattering (SAXS) data were collected on a Rigaku S-Max 3000 High Brilliance three pinhole SAXS system outfitted with a MicroMax-007HFM rotating anode (Cu Kα), Confocal Max-Flux Optic, Gabriel multiwire area detector, and a Linkam thermal stage. Dry polymer samples were sandwiched between Kapton windows (0.05 mm thick x 10 mm diameter). Exposure times for samples were typically on the order of 3600 s.

3.6 Supporting Information

[1]1H NMR and SEC of SO-anth, SAXS data and Percus-Yevick model fits comparing morphology between preblended and photo-installed of comparable SOS concentrations, and compression data for SO/SOS hydrogels.

3.6.1 ^{1}H-NMR spectrum of SO-anth
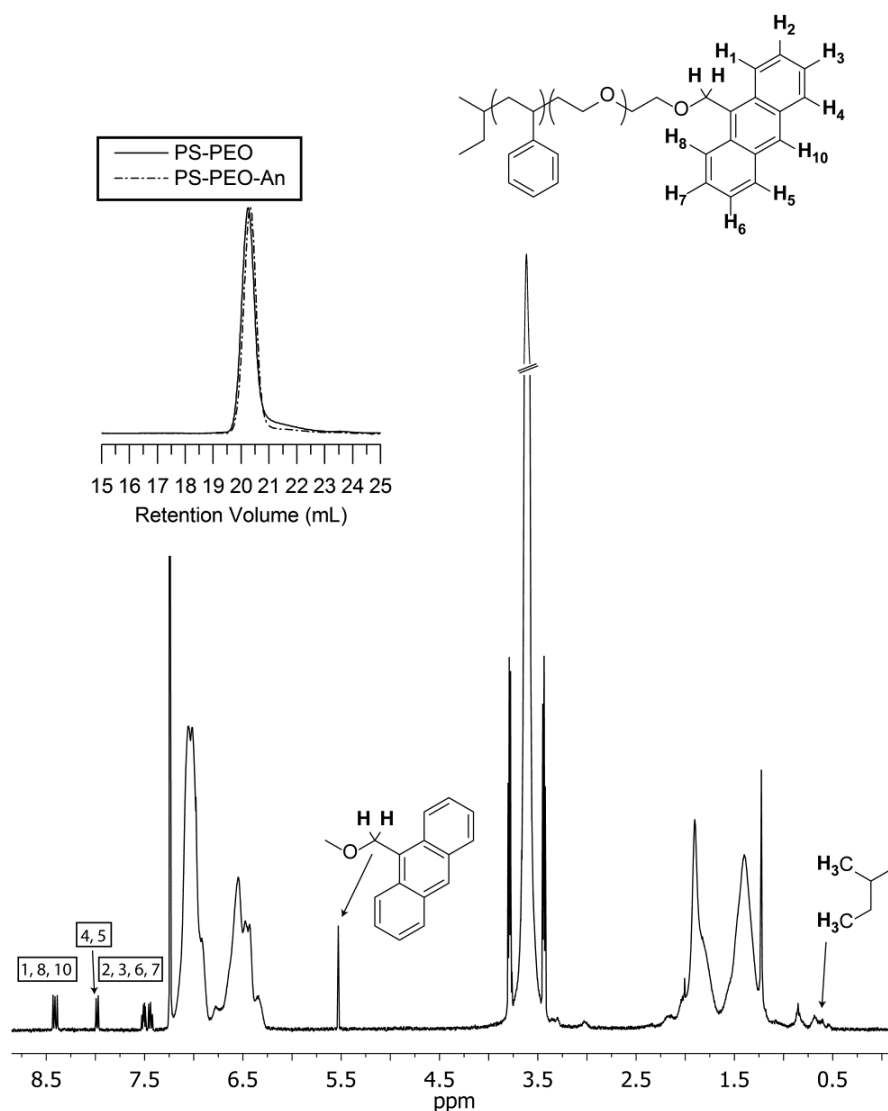
Figure S3.1. ^{1}H NMR end-group assignments of SO-anth. SEC traces of PS–PEO and PS–PEO–An showing near identical molecular weight distributions (inset).

3.6.2 SAXS comparison of samples with photo-installed vs. pre-blended SOS content
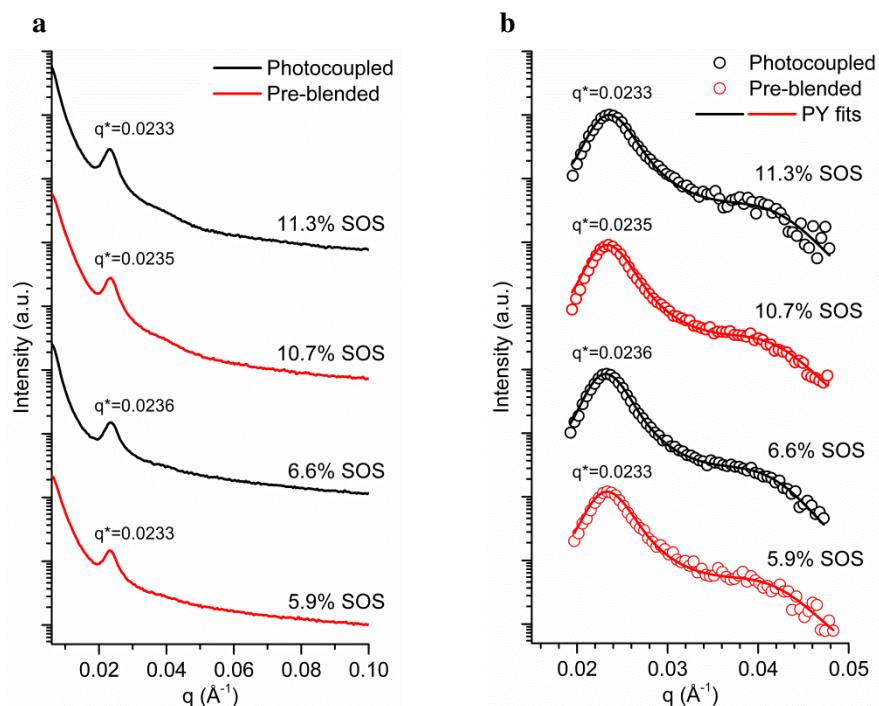
Fig S3.2. (a) Shows 1D azimuthally integrated SAXS data comparing photocoupled SOS 6.6 (1 minute UV exposure) and SOS 11.3 (3 minutes UV exposure) to samples pre-blended to approximately match the SOS contents of these photocoupled samples (SOS 5.9 and SOS 10.7). This was done in the melt at 100 °C just prior to vitrification. The primary peak and adjacent broad shoulder are typical scattering signatures for SOS blends exhibiting a liquid-like packing of spheres, as described previously by our group[26, 27] and others. [44, 46, 70-72] **(b)** Fits of the SOS 5.9, SOS 6.6, SOS 10.7, and SOS 11.3 to a Percus-Yevick hard sphere model[73] for polydisperse spheres confirms a polystyrene core radius of 10.5 nm, with an principal domain spacing of about 26 - 27 nm. Such similarity is expected based on our previous experience with these types of blends (used in hydrogel applications), and is an intended byproduct of using "lattice matched" SO and SOS block copolymer compositions.[26, 27]

Table S3.1. Chemical and melt-state morphological characterization data of block copolymer blends

Sample	Tether added (mol%)	q^*/Å^{-1}	d^*/nm	f_{PS}	$R_c{}^a$/nm	$\phi_c{}^b$	$\theta_{PS}{}^c$	$R_{hs}{}^d$/nm	$\phi_{hs}{}^e$
					Percus-Yevick hard sphere model				
SOS 5.9	5.9	0.0233	27.0	0.125	9.2	0.118	237	15.2	0.53
SOS 6.6 (1 min UV)	6.6	0.0236	26.6	0.125	9.2	0.116	238	15.5	0.55
SOS 10.7	10.7	0.0235	26.7	0.125	9.2	0.116	232	15.3	0.54
SOS 11.3 (3 min UV)	11.3	0.0233	27.0	0.125	9.1	0.118	229	15.1	0.54

[a]Micelle core radius, [b]Micelle core overall volume fraction, $\phi_c=(R_c/R_{hs})^3\phi_{hs}$, based on the PY parameters, [c]Mean aggregation number (i.e., PS chains per sphere), based on the PY parameters, [d]apparent hard sphere radius, [e]hard sphere volume fraction.
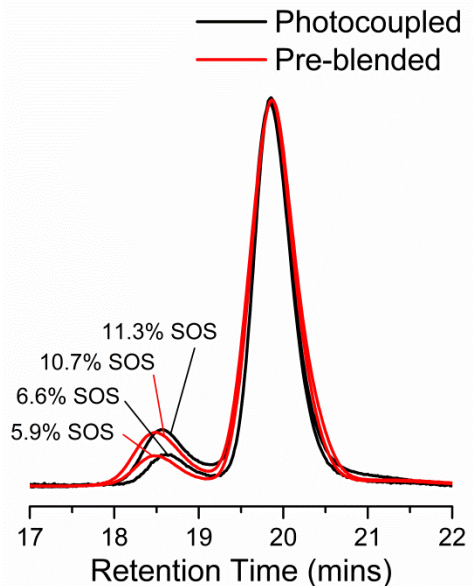
Figure S3.3. SOS content was found by use of GPC. Overlaid S, SO-OH, and SOS-50 materials GPC traces show successful polymerization and subsequent coupling of the starting materials. ^{1}H NMR of the SO-OH was used to determine the size characteristics of the material materials used (f_{PS} = 0.125 (using nominal densities at 140 ˚C)[68], $M_{n,PS}$ = 8,060, $M_{w,PS}/M_{n,PS}$ = 1.03, $M_{n,SO}$ = 71,000 g mol $^{-1}$, $M_{w,SO}/M_{n,SO}$ = 1.05).

3.6.3 Unconfined uniaxial compression data of pre-blended samples
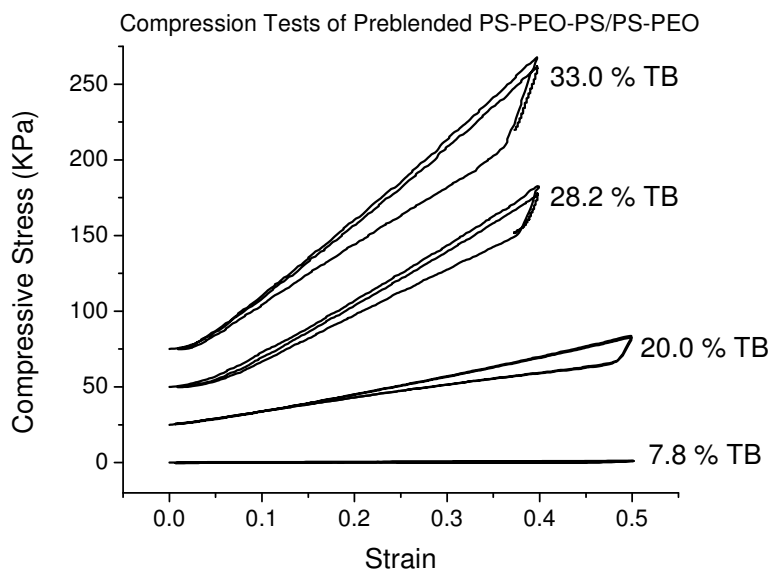
Figure S3.4. Two cycles of unconfined compression data (50% strain at 2% s^{-1}) over two successive cycles on pre-blended samples of various SOS content.

3.6.4 Sample Identification History

Table S3.2.

Manuscript ID	Lab Notebook ID
S	DBW1142
SO	CG3196, NH4128*
SOS	JTL1006, NH4127*
SO-anth	VFS7133, NH4129*
SO/SOS pre-blends	VFS7151

*Applies to data shown in **Figure S3.2** and **S3.3** only

51

References

1.   Hoare, T. R.; Kohane, D. S. Hydrogels in drug delivery: Progress and challenges. *Polymer* **2008,** 49, (8), 1993-2007.

2.   Slaughter, B. V.; Khurshid, S. S.; Fisher, O. Z.; Khademhosseini, A.; Peppas, N. A. Hydrogels in Regenerative Medicine. *Adv. Mater.* **2009,** 21, 3307-3329.

3.   Tokarev, I.; Minko, S. Stimuli-Responsive Porous Hydrogels at Interfaces for Molecular Filtration, Separation, Controlled Release, and Gating in Capsules and Membranes. *Adv. Mater.* **2010,** 22, 3446-3462.

4.   Desai, P. N.; Yuan, Q.; Yang, H. Synthesis and Characterization of Photocurable Polyamidoamine Dendrimer Hydrogels as a Versatile Platform for Tissue Engineering and Drug Delivery. *Biomacromolecules* **2010,** 11, (3), 666-673.

5.   Galperin, A.; Long, T. J.; Ratner, B. D. Degradable, Thermo-Sensitive Poly(N-isopropyl acrylamide)-Based Scaffolds with Controlled Porosity for Tissue Engineering Applications. *Biomacromolecules* **2010,** 11, (10), 2583-2592.

6.   Hou, Y.; Schoener, C. A.; Regan, K. R.; Munoz-Pinto, D.; Hahn, M. S.; Grunlan, M. A. Photo-Cross-Linked PDMSstar-PEG Hydrogels: Synthesis, Characterization, and Potential Application for Tissue Engineering Scaffolds. *Biomacromolecules* **2010,** 11, (3), 648-656.

7.   Lee, K. Y.; Mooney, D. J. Hydrogels for Tissue Engineering. *Chem. Rev.* **2001,** 101, (7), 1869-1880.

8.   Stile, R. A.; Burghardt, W. R.; Healy, K. E. Synthesis and Characterization of Injectable Poly(N-isopropylacrylamide)-Based Hydrogels That Support Tissue Formation in Vitro. *Macromolecules* **1999,** 32, (22), 7370-7379.

9.   Kozlovskaya, V.; Sukhishvili, S. A. Amphoteric Hydrogel Capsules: Multiple Encapsulation and Release Routes. *Macromolecules* **2006,** 39, (18), 6191-6199.

10.   Xu, Y.; Sato, K.; Mawatari, K.; Konno, T.; Jang, K.; Ishihara, K.; Kitamori, T. A Microfluidic Hydrogel Capable of Cell Preservation without Perfusion Culture under Cell-Based Assay Conditions. *Adv. Mater.* **2010,** 22, 3017-3021.

11.   Dai, H.; Chen, Q.; Qin, H.; Guan, Y.; Shen, D.; Hua, Y.; Tang, Y.; Xu, J. A Temperature-Responsive Copolymer Hydrogel in Controlled Drug Delivery. *Macromolecules* **2006,** 39, (19), 6584-6589.

12.   Gong, C.; Shi, S.; Wang, X.; Wang, Y.; Fu, S.; Dong, P.; Chen, L.; Zhao, X.; Wei, Y.; Qian, Z. Novel Composite Drug Delivery System for Honokiol Delivery: Self-Assembled Poly(ethylene glycol)–Poly(ε-caprolactone)–Poly(ethylene glycol) Micelles in Thermosensitive Poly(ethylene glycol)–Poly(ε-caprolactone)–Poly(ethylene glycol) Hydrogel. *J. Phys. Chem. B* **2009,** 113, (30), 10183-10188.

13.   Annaka, M.; Matsuura, T.; Kasai, M.; Nakahira, T.; Hara, Y.; Okano, T. Preparation of Comb-Type N-Isopropylacrylamide Hydrogel Beads and Their Application for Size-Selective Separation Media. *Biomacromolecules* **2003,** 4, (2), 395-403.

14.   Susanto, H.; Ulbricht, M. Photografted Thin Polymer Hydrogel Layers on PES Ultrafiltration Membranes:‚Äâ Characterization, Stability, and Influence on Separation Performance. *Langmuir* **2007,** 23, (14), 7818-7830.

15.   Tokuyama, H.; Iwama, T. Temperature-Swing Solid-Phase Extraction of Heavy Metals on a Poly(N-isopropylacrylamide) Hydrogel. *Langmuir* **2007,** 23, (26), 13104-13108.

16.   Bailey, T. S. Morphological behavior spanning the symmetric AB and ABC block copolymer states. Ph.D. Dissertation, University of Minnesota, Minneapolis, Minnesota, 2001.

17.   Bailey, T. S.; Hardy, C. M.; Epps, T. H.; Bates, F. S. A Noncubic Triply Periodic Network Morphology in Poly(isoprene-b-styrene-b-ethylene oxide) Triblock Copolymers. *Macromolecules* **2002,** 35, (18), 7007-7017.

18.   Bailey, T. S.; Pham, H. D.; Bates, F. S. Morphological Behavior Bridging the Symmetric AB and ABC States in the Poly(styrene-b-isoprene-b-ethylene oxide) Triblock Copolymer System. *Macromolecules* **2001,** 34, (20), 6994-7008.

19.   Bates, F. S.; Fredrickson, G. H. Block Copolymers: Designer Soft Materials. *Phys.Today* **1999,** 52, 32-38.

20.   Epps, T. H.; Cochran, E. W.; Bailey, T. S.; Waletzko, R. S.; Hardy, C. M.; Bates, F. S. Ordered Network Phases in Linear Poly(isoprene-*b*-styrene-*b*-ethylene oxide) Triblock Copolymers. *Macromolecules* **2004,** 37, (22), 8325-8341.

21.   Epps, T. H.; Cochran, E. W.; Hardy, C. M.; Bailey, T. S.; Waletzko, R. S.; Bates, F. S. Network phases in ABC triblock copolymers. *Macromolecules* **2004,** 37, (19), 7085-7088.

22.   Mes, T.; Koenigs, M. M. E.; Scalfani, V. F.; Bailey, T. S.; Meijer, E. W.; Palmans, A. R. A. Network Formation in an Orthogonally Self-Assembling System. *Acs Macro Lett* **2012,** 1, (1), 105-109.

23.   Bates, F. S. Polymer-Polymer Phase Behavior. *Science* **1991,** 251, (4996), 898-905.

24.   Wijayasekara, D. B.; Huang, T.; Richardson, J. M.; Knauss, D. M.; Bailey, T. S. The Role of Architecture in the Melt-State Self-Assembly of (Polystyrene)$_{star}$-*b*-(Polyisoprene)$_{linear}$-*b*-(Polystyrene)$_{star}$ Pom-Pom Triblock Copolymers. *Macromolecules* **2016,** 49, (2), 595-608.

25.   Wijayasekara, D. B.; Cowan, M. G.; Lewis, J. T.; Gin, D. L.; Noble, R. D.; Bailey, T. S. Elastic free-standing RTIL composite membranes for CO2/N2 separation based on sphere-forming triblock/diblock copolymer blends. *Journal of Membrane Science* **2016,** 511, 170-179.

26.   Guo, C.; Bailey, T. S. Highly distensible nanostructured elastic hydrogels from AB diblock and ABA triblock copolymer melt blends. *Soft Matter* **2010,** 6, (19), 4807-4818.

27.   Guo, C.; Bailey, T. S. Tailoring mechanical response through coronal layer overlap in tethered micelle hydrogel networks. *Soft Matter* **2015,** 11, (37), 7345-7355.

28.   Guo, C.; Lewis, J. T.; Scalfani, V. F.; Schwartz, M. M.; Bailey, T. S. Dangling-End Double Networks: Tapping Hidden Toughness in Highly Swollen Thermoplastic Elastomer Hydrogels. *Chem. Mater.* **2016,** 28, (6), 1678-1690.

29.   Scalfani, V. F.; Bailey, T. S. Access to Nanostructured Hydrogel Networks through Photocured Body-Centered Cubic Block Copolymer Melts. *Macromolecules* **2011,** 44, (16), 6557-6567.

30.   Scalfani, V. F.; Bailey, T. S. Thermally Stable Photocuring Chemistry for Selective Morphological Trapping in Block Copolymer Melt Systems. *Chem. Mater.* **2010,** 22, (21), 5992-6000.

31.   Scalfani, V. F. Part I — Access to UV Photocured Nanostructures via Selective Morphological Trapping of Block Copolymer Melts. Part II — Morphological Phase Behavior of Poly(RTIL) Containing Block Copolymer Melts. Ph.D. Dissertation, Colorado State University, Fort Collins, Colorado, 2012.

32.   Becker, H. D. Unimolecular photochemistry of anthracenes. *Chem. Rev.* **1993,** 93, (1), 145-172.

33.   Froimowicz, P.; Frey, H.; Landfester, K. Towards the Generation of Self-Healing Materials by Means of a Reversible Photo-induced Approach. *Macromol. Rapid Commun.* **2011,** 32, (5), 468-473.

34.	Wells, L. A.; Brook, M. A.; Sheardown, H. Generic, Anthracene-Based Hydrogel Crosslinkers for Photo-controllable Drug Delivery. *Macromol Biosci* **2011,** 11, (7), 988-998.

35.	Wells, L. A.; Furukawa, S.; Sheardown, H. Photoresponsive PEG-Anthracene Grafted Hyaluronan as a Controlled-Delivery Biomaterial. *Biomacromolecules* **2011,** 12, (4), 923-932.

36.	Zheng, Y.; Micic, M.; Mello, S. V.; Mabrouki, M.; Andreopoulos, F. M.; Konka, V.; Pham, S. M.; Leblanc, R. M. PEG-Based Hydrogel Synthesis via the Photodimerization of Anthracene Groups. *Macromolecules* **2002,** 35, (13), 5228-5234.

37.	Epps, T. H.; Bailey, T. S.; Pham, H. D.; Bates, F. S. Phase Behavior of Lithium Perchlorate-Doped Poly(styrene-b-isoprene-b-ethylene oxide) Triblock Copolymers. *Chem. Mater.* **2002,** 14, (4), 1706-1714.

38.	Epps, T. H.; Bailey, T. S.; Waletzko, R.; Bates, F. S. Phase Behavior and Block Sequence Effects in Lithium Perchlorate-Doped Poly(isoprene-*b*-styrene-*b*-ethylene oxide) and poly(styrene-*b*-isoprene-b-ethylene oxide) Triblock Copolymers. *Macromolecules* **2003,** 36, (8), 2873-2881.

39.	Scalfani, V. F.; Wiesenauer, E. F.; Ekblad, J. R.; Edwards, J. P.; Gin, D. L.; Bailey, T. S. Morphological Phase Behavior of Poly(RTIL)-Containing Diblock Copolymer Melts. *Macromolecules* **2012,** 45, (10), 4262-4276.

40.	Shi, Z.; Newell, B. S.; Bailey, T. S.; Gin, D. L. Ordered, Microphase-Separated, Noncharged-Charged Diblock Copolymers via the Sequential ATRP of Styrene and Styrenic Imidazolium Monomers. *Polymer* **2014,** 55, (26), 6664-6671.

41.	Wiesenauer, E. F.; Edwards, J. P.; Scalfani, V. F.; Bailey, T. S.; Gin, D. L. Synthesis and Ordered Phase Separation of Imidazolium-Based Alkyl-Ionic Diblock Copolymers Made via ROMP. *Macromolecules* **2011,** 44, (13), 5075-5078.

42.	Wiesenauer, E. F.; Nguyen, P. T.; Newell, B. S.; Bailey, T. S.; Noble, R. D.; Gin, D. L. Imidazolium-Containing, Hydrophobic-Ionic-Hydrophilic ABC Triblock Copolymers: Synthesis, Ordered Phase-Separation, and Supported Membrane Fabrication. *Soft Matter* **2013,** 9, (33), 7923-7927.

43.	Cavicchi, K. A.; Lodge, T. P. Self-Diffusion and Tracer Diffusion in Sphere-Forming Block Copolymers. *Macromolecules* **2003,** 36, (19), 7158-7164.

44.	Kinning, D. J.; Thomas, E. L. Hard-sphere interactions between spherical domains in diblock copolymers. *Macromolecules* **1984,** 17, (9), 1712-1718.

45.   Lee, S.-H.; Char, K.; Kim, G. Order–Disorder and Order–Order Transitions in Mixtures of Highly Asymmetric Triblock Copolymer and Low Molecular Weight Homopolymers. *Macromolecules* **2000,** 33, (19), 7072-7083.

46.   Wang, X.; Dormidontova, E. E.; Lodge, T. P. The Order−Disorder Transition and the Disordered Micelle Regime for Poly(ethylenepropylene-b-dimethylsiloxane) Spheres. *Macromolecules* **2002,** 35, (26), 9687-9697.

47.   Jeon, H. K.; Macosko, C. W.; Moon, B.; Hoye, T. R.; Yin, Z. H. Coupling reactions of end- vs mid-functional polymers. *Macromolecules* **2004,** 37, (7), 2563-2571.

48.   Orr, C. A.; Cernohous, J. J.; Guegan, P.; Hirao, A.; Jeon, H. K.; Macosko, C. W. Homogeneous reactive coupling of terminally functional polymers. *Polymer* **2001,** 42, (19), 8171-8178.

49.   Macosko, C. W.; Jeon, H. K.; Hoye, T. R. Reactions at polymer–polymer interfaces for blend compatibilization. *Prog. Polym. Sci.* 30, (8-9), 939-947.

50.   Sigmund, W. M.; Bailey, T. S.; Hara, M.; Sasabe, H.; Knoll, W.; Duran, R. S. Langmuir-Blodgett-Films of 3-Alkylpyrroles Studied by Scanning-Tunneling-Microscopy. *Langmuir* **1995,** 11, (8), 3153-3160.

51.   Chen, W.; Wang, J.-Y.; Zhao, W.; Li, L.; Wei, X.; Balazs, A. C.; Matyjaszewski, K.; Russell, T. P. Photocontrol over the Disorder-to-Order Transition in Thin Films of Polystyrene-block-poly(methyl methacrylate) Block Copolymers Containing Photodimerizable Anthracene Functionality. *J. Am. Chem. Soc.* **2011,** 133, (43), 17217-17224.

52.   Greene, F. D.; Misrock, S. L.; Wolfe, J. R. The Structure of Anthracene Photodimers. *J. Am. Chem. Soc.* **1955,** 77, (14), 3852-3855.

53.   Goldbach, J. T.; Russell, T. P.; Penelle, J. Synthesis and Thin Film Characterization of Poly(styrene-block-methyl methacrylate) Containing an Anthracene Dimer Photocleavable Junction Point. *Macromolecules* **2002,** 35, (11), 4271-4276.

54.   Ulbricht, M. Advanced functional polymer membranes. *Polymer* **2006,** 47, (7), 2217-2262.

55.   Dai, W. S.; Barbari, T. A. Hydrogel membranes with mesh size asymmetry based on the gradient crosslinking of poly(vinyl alcohol). *Journal of Membrane Science* **1999,** 156, (1), 67-79.

56.   Luo, Y.; Dalton, P. D.; Shoichet, M. S. Investigating the Properties of Novel Poly(2-hydroxyethyl methacrylate-co-methyl methacrylate) Hydrogel Hollow Fiber Membranes. *Chem. Mater.* **2001,** 13, (11), 4087-4093.

57.   Tenhaeff, W. E.; Gleason, K. K. Surface-Tethered pH-Responsive Hydrogel Thin Films as Size-Selective Layers on Nanoporous Asymmetric Membranes. *Chem. Mater.* **2009,** 21, (18), 4323-4331.

58.   Bailey, T. S.; Rzayev, J.; Hillmyer, M. A. Routes to Alkene and Epoxide Functionalized Nanoporous Materials from Poly(styrene-*b*-isoprene-*b*-lactide) Triblock Copolymers. *Macromolecules* **2006,** 39, (25), 8772-8781.

59.   Bolton, J.; Bailey, T. S.; Rzayev, J. Large Pore Size Nanoporous Materials from the Self-Assembly of Asymmetric Bottlebrush Block Copolymers. *Nano Lett.* **2011,** 11, (3), 998-1001.

60.   Cavicchi, K. A.; Zalusky, A. S.; Hillmyer, M. A.; Lodge, T. P. An ordered nanoporous monolith from an elastomeric crosslinked block copolymer precursor. *Macromol. Rapid Commun.* **2004,** 25, (6), 704-709.

61.   Guo, S. W.; Rzayev, J.; Bailey, T. S.; Zalusky, A. S.; Olayo-Valles, R.; Hillmyer, M. A. Nanopore and nanobushing Arrays from ABC triblock thin films containing two etchable blocks. *Chem. Mater.* **2006,** 18, (7), 1719-1721.

62.   Hillmyer, M. A. Nanoporous materials from block copolymer precursors. *Adv. Polym. Sci.* **2005,** 190, 137-181.

63.   Mao, H.; Hillmyer, M. A. Macroscopic samples of polystyrene with ordered three-dimensional nanochannels. *Soft Matter* **2006,** 2, (1), 57-59.

64.   Mao, H. M.; Arrechea, P. L.; Bailey, T. S.; Johnson, B. J. S.; Hillmyer, M. A. Control of Pore Hydrophilicity in Ordered Nanoporous Polystyrene Using an AB/AC Block Copolymer Blending Strategy. *Faraday Discuss.* **2005,** 128, 149-162.

65.   Rzayev, J.; Hillmyer, M. A. Nanochannel Array Plastics with Tailored Surface Chemistry. *J. Am. Chem. Soc.* **2005,** 127, (38), 13373-13379.

66.   Rzayev, J.; Hillmyer, M. A. Nanoporous Polystyrene Containing Hydrophilic Pores from an ABC Triblock Copolymer Precursor. *Macromolecules* **2005,** 38, (1), 3-5.

67.   Zalusky, A. S.; Olayo-Valles, R.; Taylor, C. J.; Hillmyer, M. A. Mesoporous Polystyrene Monoliths. *J. Am. Chem. Soc.* **2001,** 123, (7), 1519-1520.

68.   Fetters, L. J.; Lohse, D. J.; Richter, D.; Witten, T. A.; Zirkel, A. Connection between Polymer Molecular Weight, Density, Chain Dimensions, and Melt Viscoelastic Properties. *Macromolecules* **1994,** 27, (17), 4639-47.

69.   Coursan, M.; Desvergne, J. P.; Deffieux, A. Reversible photodimerisation of ω-anthrylpolystyrenes. *Macromol. Chem. Phys.* **1996,** 197, (5), 1599-1608.

70.   Dormidontova, E. E.; Lodge, T. P. The order-disorder transition and the disordered micelle regime in sphere-forming block copolymer melts. *Macromolecules* **2001,** 34, (26), 9143-9155.

71.   Schwab, M.; Stuhn, B. The states of order and the kinetics of the disorder-to-order transition in strongly asymmetric diblock copolymers. *J. Mol. Struct.* **1996,** 383, (1-3), 57-62.

72.   Schwab, M.; Stuhn, B. Thermotropic transition from a state of liquid order to a macrolattice in asymmetric diblock copolymers. *Phys. Rev. Lett.* **1996,** 76, (6), 924-927.

73.   Percus, J. K.; Yevick, G. J. Analysis of Classical Statistical Mechanics by Means of Collective Coordinates. *Phys Rev* **1958,** 110, (1), 1-13.

Chapter 4.

Reversible Photocoupling

Originally, the melt-state photocoupling established in **Chapter 3** was intended to not only be a source of mechanical tunability for the hydrogel for biomedical applications, but also a means of providing a size-tunable mesh for ultrafiltration purposes. This chapter explores the potential for using anthracene's reversible photocoupling capabilities for development of this membrane, as well as other potential applications. While this particular capability and application were not pursued further, the results and discussion may provide insight into the foundational anthracene-based BCP hydrogel system used for the rest of this dissertation. The work in this chapter builds on the information provided in the previous chapter, and exploits the versatility of these systems for development of a hydrogel membrane intended for separation of biomacromolecules.

4.1 Summary

Anthracene can be repeatedly coupled (365 nm) and decoupled (254 nm) via UV irradiation, with 100% reversibility. In this study, we aimed to exploit this reversible coupling ability to allow polymer chain ends to be joined and separated repeatedly exploiting anthracene as a substituent. However, the ability to repeatedly couple and decouple chain ends was found to be challenging, with each successive irradiative cycle achieving a lower efficiency than the last. A number of studies were performed in an attempt to discover the source of this limitation. First, based on the hypothesis that the anthracene group was being cleaved from the diblock copolymer chain end due to susceptibility of polystyrene to radical formation through absorption of the 254

59

nm light used for decoupling, we explored the effect of an alternate A block. To simplify the synthetic demands and remove the potential influence of the PEO, polystyrene (PS) and polyisoprene (PI) homopolymers were directly functionalized with anthracene. No significant improvement in an ability to repeatedly photocouple and decouple using PI was found. As a result, the potential of a radical inhibitor (BHT) to improve SO-anth's ability to reversibly photocouple was further explored. Addition of BHT provided some improved reversibility from initial experiments, however the ability to recouple after every subsequent decoupling cycle continued to decrease regardless.

4.2 Introduction

The objective of this project is to develop a low cost, easily fabricated ultrafiltration (UF) membrane with light-responsive mesh size tunability and the ability to resist, and potentially reverse, fouling. UF membrane filtration systems, a class of membranes in which pore sizes are below the microscale, are used in a variety of applications including chemical processing and pharmaceuticals, food and beverage industries, and in water treatment.[1] They are used primarily in industrial and academic macromolecular solution processing and research, and are of particular interest to us for size selectivity with nanoparticles, protein solutions, and other biomacromolecules. The driving force for UF membranes can be pressure or concentration gradients, in which a semipermeable membrane prevents high molecular weight solutes from passing into the permeate while allowing low molecular weight components (including solvents) to pass through membrane pores.

Some limitations in currently utilized membrane systems are fouling by particulate deposition, complexity in fabrication and design, and low flux.[2, 3] These shortcomings all work to drive up

costs of UF membranes by necessitating frequent replacement, high production costs, and low filtration efficiencies. Our intended hydrogel UF membrane design combats these shortcomings by working towards an antifouling, tunable, and low-cost filter with high flux filtration capabilities.

Our photoactive TPE hydrogel is a mechanically tunable system based around the use of polystyrene-*b*-poly(ethylene oxide)-anthracene (SO-anth or PS-*b*-PEO-anth). This tunability comes from photocoupling SO-anth chain ends to create PS-*b*-PEO-*b*-PS (SOS) *in situ*, therefore tethering adjacent micelles and providing a means to adjust the mechanical properties of the swollen hydrogel. An ultrafilter exploiting this tunability would have many qualities current UF membranes are lacking. The constant overall porosity due to the consistent intersphere distance that naturally occurs due to length of blocks lends to high flux filtration and improved membrane selectivity from current systems. This inherent homogeneity which is a product of self-assembly also results in narrow pore size distributions.

A key feature in these TPE hydrogel UF membranes is the potential to incorporate reversible changes in mesh size via UV, which may also lend to fouling resistance and tailored molecular weight cutoffs. These advantages come from the ability to tether the photoactive micellar building blocks of the SO-anth system, in that increased network strand densities lend to smaller pore spaces within the network. Slightly different from the original melt-tunable system described in **Chapter 3**,[4] the UF hydrogel design includes a small concentration of primary, permanent network of SOS tethers to fix a base-level pore size (likely on the order of 10%) and to lend to ease of handling). This primary network sets the intersphere distance between micelles in the lattice. The balance of the SOS BCP population is comprised of SO-anth which provides a photoactive corona of photoactive dangling PEO-anth. This provides the ability to tether and

untether adjacent micelles through the coronal end-groups when irradiated, producing a secondary mesh of photo-installed SOS tethers which can be adjusted to suit separation needs. The potential for fouling resistance for extended membrane lifetime is both inherent to the hydrogel due to hydrophilicity, and also augmented in this system particularly by the ability to remove of all SOS tethers from the secondary network by UV, therefore allowing any fouling to be released.

It has already been shown in the literature[5, 6] and through our own investigation (**Figure S4.1**) that free anthracene can dimerize reversibly at 100% efficiency using efficient photoinduced [4 + 4]cycloaddition (λ = 365 nm) as depicted in **Figure 4.1**. However, previous attempts by our group to exploit this reversibility for anthracene functionalized SO diblock copolymer succeeded in melt coupling only about 5% of the originally photocoupled end groups after decoupling for the first time.[7]
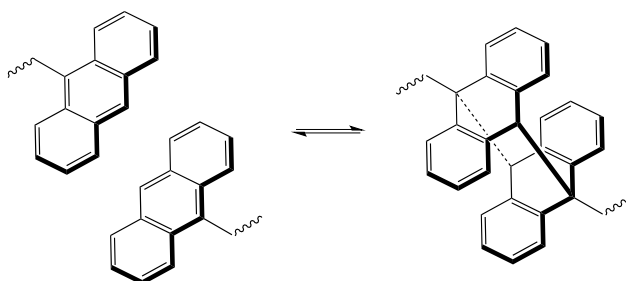
Figure 4.1. Anthracene end group reversibly dimerizing via a photoinduced [4 + 4]cycloaddition (λ = 365 nm).

One theory behind this loss in coupling efficiency after decoupling, is the tendency of PS phenyl radicals to cause instability and detachment of the anthracene end-group from SO diblock copolymer, therefore reducing the concentration of chain ends available for photocoupling. These radicals may alternatively be due to the phenyl groups of the anthracene functionality

substituent itself, in which case detachment may also be due to the proximity of the oxygen on the PEO to the anthracene group. Here, we explore the viability of the proposed TPE hydrogel UF system through a number of preliminary experimental studies which probe time-dependent photocoupling and decoupling, as well as the capabilities and limitations of a reversibly photoactive BCP system.

4.3 Results

4.3.1 PI-anth vs. PS-anth photocoupling

In an attempt to discover deficiency in reversibility (defined as the ability to couple, decouple, then recouple anthracene when attached to the diblock copolymer), the effect of the polystyrene (PS) A block was explored on the theory that the anthracene group separates from the SO diblock copolymer chain end due to radical instability. In addition, PS absorbs light around 254 nm, which may have lent to negative effects on decoupling efficiency of the system, and subsequent attempts to recouple.[8] In this experiment, the midblock PEO was omitted and polystyrene (PS) and polyisoprene (PI) were both directly functionalized with anthracene in order to determine the role of the PS phenyl ring on the deattachment of anthracene to SO, and conclude whether PS phenyl radicals were causing a reduction in photoactive chain ends after the initial photocoupling cycle.

PI-OH (mechanism shown in **Scheme S4.1** was functionalized with anthracene as done with SO-anth in previous work,[4] via displacement of the chlorine on precursor 9-chlormethyl anthracene by nucleophilic substitution using the potassium alkoxide of the terminal hydroxyl end-group of the PI-OH BCP to form PI-anth (M_n= 8450 g/mol, M_w/M_n=1.06), a sticky, viscous liquid (**Scheme S4.2**). The same procedure was used to make PS-anth (M_n= 8290 g/mol ,

M_w/M_n=1.03), a dry, off-white powder. NMR spectra of PI-anth and PS-anth showed 64% and close to 100% attachment respectively (see **Section 4.7**, SI). Due to the viscous, sticky nature of the PI-anth and brittleness of the PS-anth, the method described in **Chapter 3** involving irradiating pressed SO-based polymers in the melt between quartz slides could not be effectively implemented. The former lacked the vitrified PS core, while the latter lacked the elastomeric qualities provided by the PEO block. As a result, PI-anth and PS-anth were each dissolved in deuterated chloroform ($CDCl_3$) and irradiated ($\lambda = 365$ nm) within quartz NMR tubes or cuvettes for ease of exposure and sampling for subsequent characterization (**Figure 4.2**). SEC traces were analyzed to determine the amount of coupled or decoupled material after exposure based on changes in molecular weight distribution.
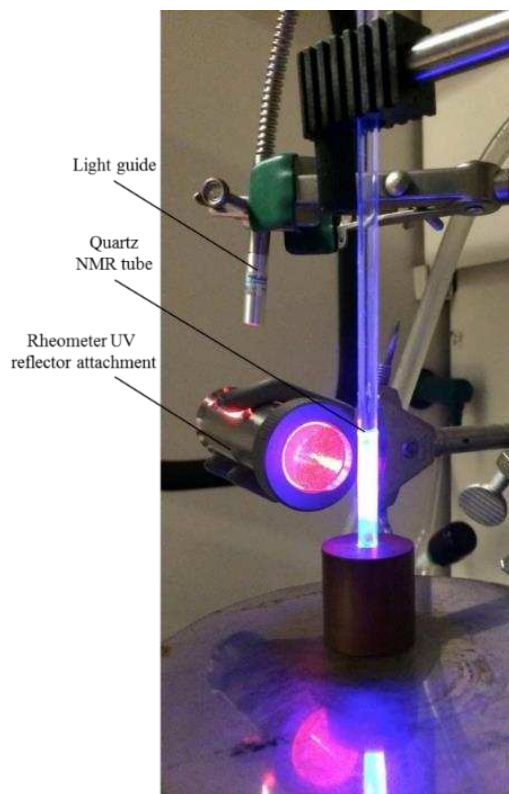
Figure 4.2. UV exposure setup for photocoupling PI-anth and PS-anth in solution using light guide, rheometer attachment, and quartz NMR tube.

The SEC traces presented in **Figure 4.3** are for samples of PI-anth and PS-anth at a range of coupling times between 0 and 6 hours. Given the discrepancy between percent functionalization of end-groups between PS and PI, anthracene end group concentrations were kept equal between the two to allow for a rigorous comparison. It is apparent from the SEC data that minimal coupling occurred in either PS and PI, likely due to the dilute solution-based photocoupling method implemented. The low-level concentration of photoactive end groups reduced the kinetics and efficiency observed with emelt photocoupling SO-anth (**Chapter 3**). As a result, coupling times on the order of days were required to see any marked coupling in these systems. There also appears to be a coupling maximum in these systems as seen by the drop in coupling after 24 hours of UV exposure. Notably, the only significant discrepancy between PI-anth and PS-anth systems was the faster coupling observed between PI-anth chains. This marginal success of PI over PS suggested that the success of reversible photocopuling may indeed have been hampered by use of a phenyl-based A block in the traditional SO diblock copolymer system. This led to further exploration of replacement of the PS in the original SO-anth construct with PI, forming a polyisoprene-*b*-poly(ethylene oxide)-anthracene diblock copolymer (IO-anth). This was also done with the aim of using a material that was more easily handled than liquid PI homopolymer. However, the absence of vitrified PS cores in the micellar matrix resulted in soft, sticky polymer which did not effectively form networks that lent to mechanical robustness, and were deemed unsuitable for the intended applications. Accordingly, IO-based materials would likely require more backbone-based crosslinks rather than solely end-groups to perform viably as separation membranes. Experiments using this material are not included given these mechanical limitations. Notably, future experiments on the effect of PEO length on photoactive SO-anth in contrast to IO-anth would be valuable given that sphere-to-sphere midblock SOS length and

overall molecular weight of the system is critical to BCP assembly and matrix performance. This is discussed in more detail in other work from our group.[9]
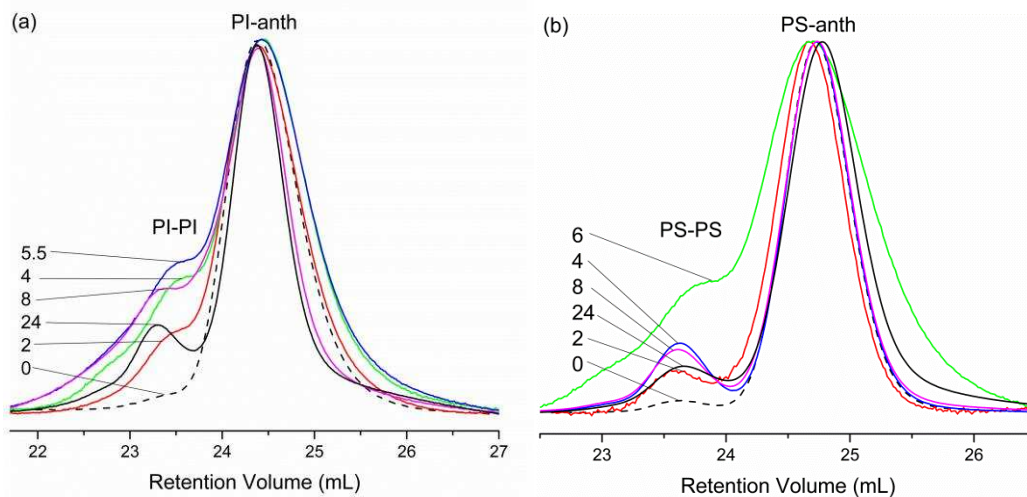
Figure 4.3: GPC traces of **(a)** PI-anth and **(b)** PS-anth photocoupling over time, with UV irradiation times indicated in hours.

4.3.2 PS-*b*-PEO

The inability to utilize a mechanically robust PI-*b*-PEO network led, once again, to the adoption of a PS-*b*-PEO based system (f_{PS} = 0.07, M_n = 114,300 g/mol, M_w/M_n = 1.08). In contrast to the SO-anth used in **Chapter 3** (f_{PS} = 0.13, M_n = 70,100 g/mol, M_w/M_n = 1.04), this SO possessed a significantly higher molecular weight due to the longer PEO block while retaining a PS homopolymer precursor similar to that used in the previous melt-based study. This resulted in a BCP of much lower PS volume fraction yielding a kinetic limitation to BCC development as seen before, and a slightly greater polydispersity. In order to determine material properties of this new system, the material was characterized in a manner similar to that of the lower molecular weight analogue, though in order to test radical inhibition, the resulting SO-anth polymer powder was this time washed repeatedly to ensure maximum removal of free

anthracene, and incorporated with butylated hydroxytoluene (BHT) as a radical inhibitor. Stacked ^{1}H NMR spectra of PS-OH, SO-OH, and SO-anth are shown in **Figure 4.4** to demonstrate successful polymerizations and subsequent end-group functionalization with anthracene (quantitative analysis shown in SI).
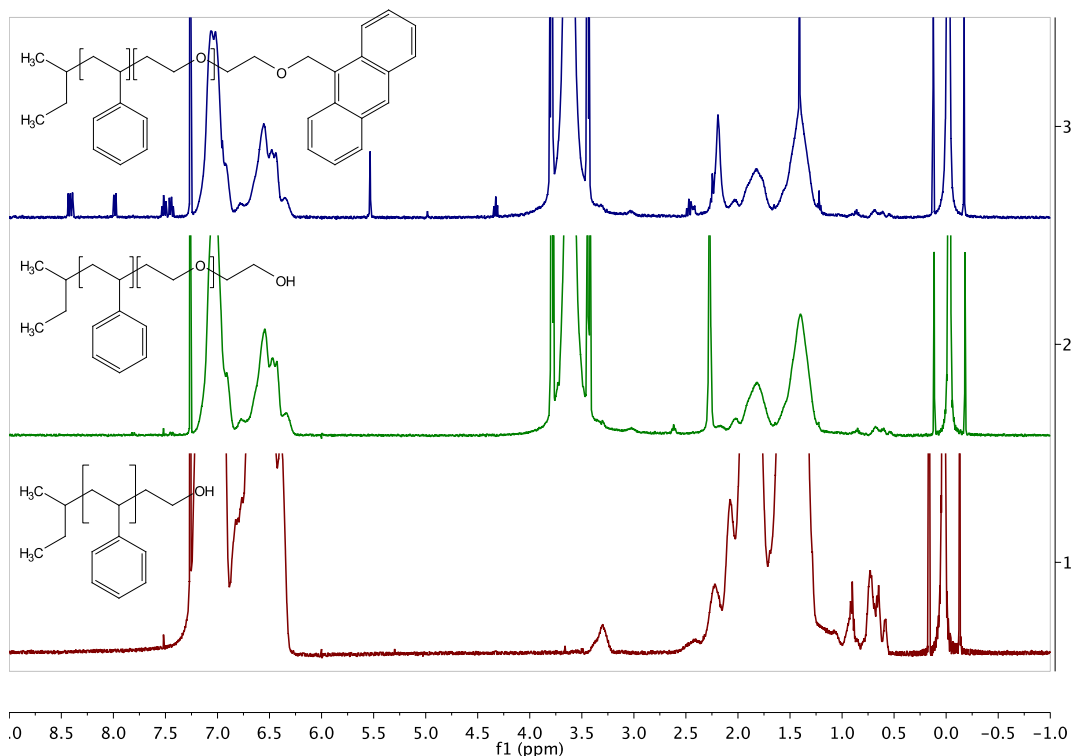
Figure 4.4. Stacked NMR spectra of (**1**) PS, (**2**) SO-OH, and (**3**) SO-anth showing successful EO polymerization and functionalization with anthracene.

SEC revealed minimal changes in molecular weight distribution before and after addition of the anthracene substituent, evidenced by overlapping SO and SO-anth traces (**Figure 4.5**). Some formation of SOS triblock copolymer can be seen to the left of the SO-anth trace, likely due to inadvertent light exposure during washing and isolation steps of SO-anth synthesis.
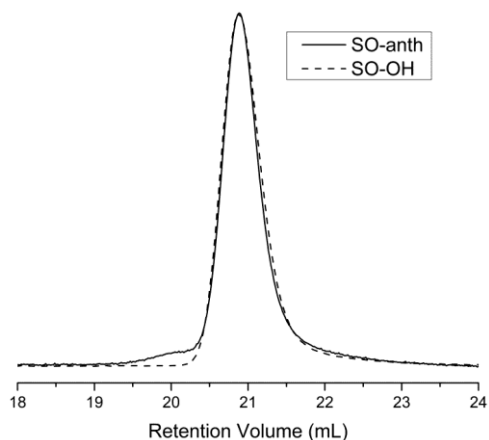
Figure 4.5: GPC traces of SO-anth (solid line) and its parent SO-OH (dashed line).

Heat pressed, self-assembled disks were subjected to additional heating on a hot plate under purge of argon, then irradiated (λ = 365 nm, I ~ 30 mW cm^{-2}) in the melt at 100° C. **Figure 4.6a** depicts SEC if samples irradiated for between 0 and 60 minutes, while **Figure 4.6b** quantifies SOS triblock copolymer content as a function of UV exposure time for the same set of experiments. This time-dependent photocoupling data shows that a plateau is reached, and that after 50 minutes there is a drop from 50% installed SOS triblock copolymer down to under 40 % with an hour's exposure.

(a)   (b)
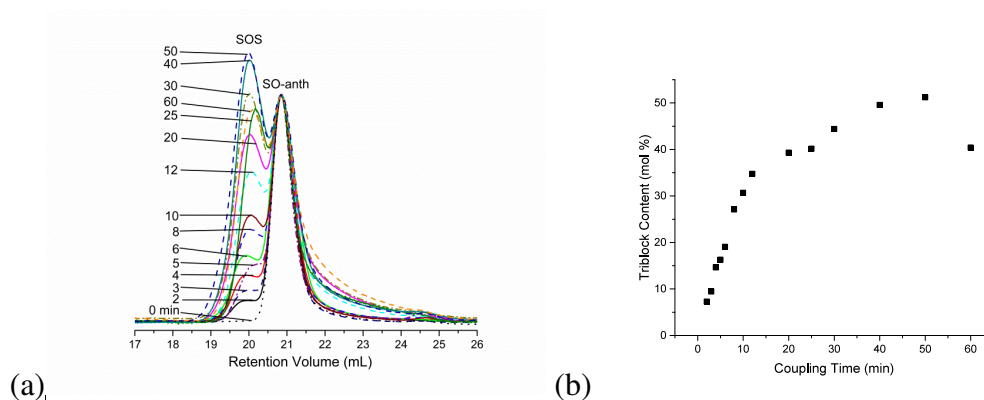
Figure 4.6. (a) GPC traces of samples photocoupled for various times between 0 and at 100° C and **(b)** concentration of installed SOS triblock copolymer as a function of 365 nm irradiation time.

68

Samples were coupled to this maximum, then decoupled for between 0 and 60 minutes (λ = 254 nm, I ~ 30 mW cm^{-2}). It is apparent from **Figure 4.7** below that most of the installed SOS was decoupled within the first 10 minutes of exposure. This higher decoupling efficiency relative to coupling is likely due to the need for chain end proximity in the latter while only sufficient irradiation is necessary for reversing the dimerization.
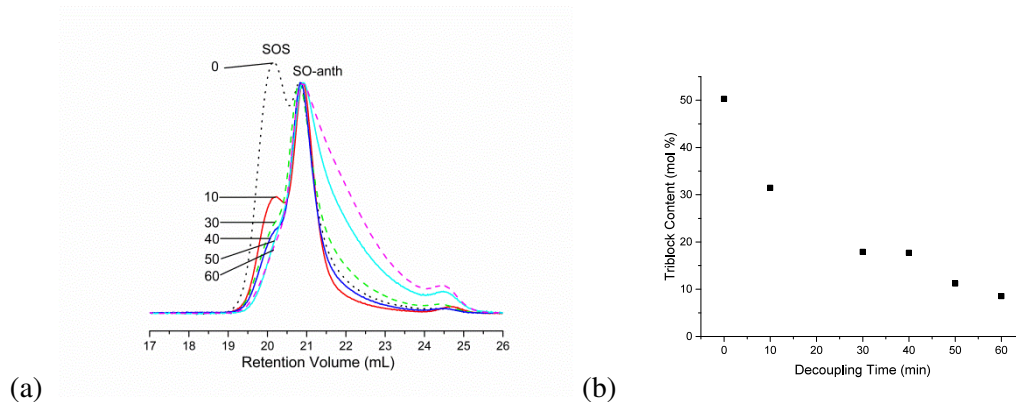
Figure 4.7. (a) GPC traces of samples decoupled of for various times at 100° C and **(b)** concentration of installed SOS triblock copolymer as a function of 254 nm irradiation time.

With the data acquired from coupling and decoupling irradiation time experiments, exposure times were chosen for an attempt at a coupling cycle- that is, coupling, decoupling, and recoupling. Timepoints were chosen so that systems were not fully coupled or decoupled, to avoid pushing the system to decouple prematurely during a coupling cycle or disabling photoactive chain ends when attempting to decouple as was suspected to be occurring during early unsuccessful experiments. **Figure 4.8a** shows SEC data for a representative cyclic trial, and **Figure 4.8b** provides SOS triblock copolymer content data for a series of experimental trials. Disks were coupled in the melt state, then swollen to equilibrium and decoupled in this state. Attempts at recoupling were then embarked upon in the melt state as well as in the swollen state to determine the effects of a hydrated environment on recoupling efficiency. This latter data

evidenced that recoupling the swollen state was less efficient and less consistent than recoupling within a hydrated hydrogel, suspected to be a result of a combination of water's interference with photocoupling UV wavelengths as well as increased dilution and subsequent reduced proximity of adjacent photoactive micelles in the swollen state.

(a)　　　　　　　　　　　　　　　　　　　　　　(b)
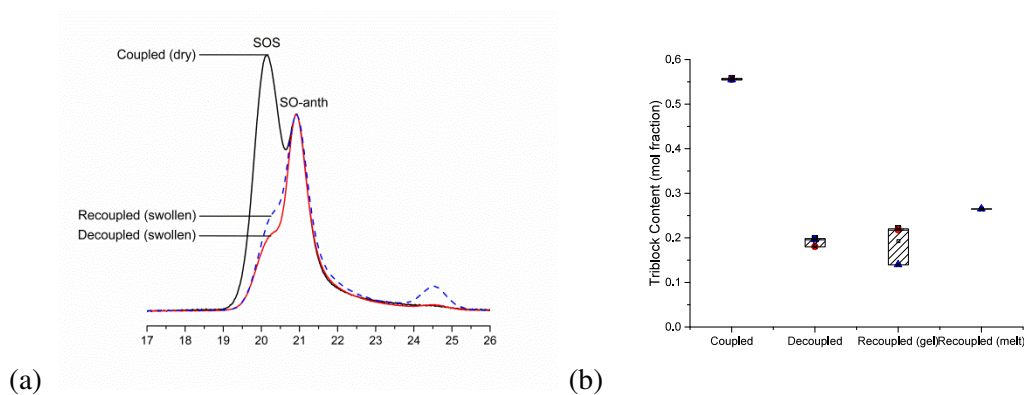
Figure 4.8. (a) GPC traces of a single trial of melt-coupled, swollen-decoupled, and melt- or swollen-recoupled samples of ABP at 100° C and **(b)** SOS content after each successive irradiation step. Mean and standard deviation are shown.

These results indicate that while the trend in photo-installation of SOS tethers remains consistent with a maximum ~55% SOS, the triblock copolymer content cannot be precisely controlled using irradiation as the laboratory-scale equipment used for these experiments does not allow for duplicating conditions exactly. However, consistent trends in the data suggest that, were all else held constant, SOS copolymer content is likely a fixed function of exposure time. The following chapters address this issue by use of a more consistent experimental conditions, including a more radially even UV light source.

To further characterize the tethering within the SO-anth system, the effect of SOS installation on swelling behavior of the hydrogels was explored (**Figure 4.9**). Samples were swollen to

equilibrium in degassed DI water after each irradiation cycle, the swelling quantified by a swelling ratio Q (g water per g polymer). Upon introduction to water, these tethered networks adopt equilibrium dimensions that are determined by a balance of osmotic swelling forces and entropic resistance to stretching intrinsic to the tethering and entangled midblocks.[4] As expected, data shown in **Figure 4.9a** demonstrates the increase in SOS content resulted in a decreased Q (g water per g polymer), confirming that a significant portion of the photoinstalled SOS served to tether spheres and resist swelling. In this manner, the decoupling step resulted in scission of these tethers, allowing the matrix to expand further to new equilibrium dimensions and produce a higher Q. Interestingly, however, upon attempting to recouple tethers in the final step of the cycle, Q increased slightly further rather than retaining its decoupled equilibrium dimensions as expected. This behavior was confirmed with size-based swelling characterization (**Figure 4.9b**), suggesting that some inadvertent decoupling may have been occurring during recoupling, resulting in the release of stressed tethers which would have otherwise served to restrict additional swelling. Importantly, the SEC and swelling data coincide to suggest that the system is hindered in its ability to fully recouple after irradiative decoupling, despite anthracene's demonstrated success in reversible photodimerization. This prompted investigation of the source of this phenomenon by ^{1}H NMR to determine whether structural changes in SO-anth chains were prohibiting cyclic tethering.

71

(a)   (b)
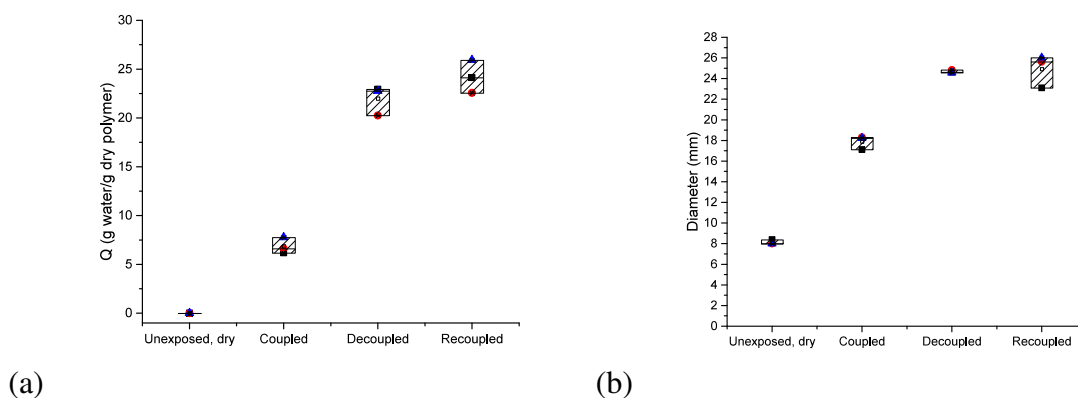
Figure 4.9. (a) Swelling ratio and **(b)** diameter of hydrogels at different points during the coupling cycle. All coupling was performed in the melt, while decoupling and recoupling were performed while the material was swollen. Mean and standard deviation are shown.

Figure 4.10 depicts stacked ^{1}H NMR of the SO-anth material after each step of a full photocoupling cycle, from bottom to top. Based on NMR spectra of free anthracene taken before and after coupling (**Figure S4.2b**), characteristic anthracene proton peaks shift from the 7.3-8.75 ppm range into the 6.25-7.25 ppm range due to the loss of aromaticity in the central six-membered ring of the anthracene molecule after dimerizing. This creates six-membered non-aromatic rings on each of the anthracene molecules involved in coupling, as well as eight-membered rings comprising bonds between the functionalities. This observed shift explains the loss in visibility of the anthracene-indicative peaks in 7.3-8.75 ppm range, since upon dimerization they are shifted into the range of PS phenyl protons. Based on SEC and NMR data, we suspect that the anthracene functionalities are no longer capable of coupling chain ends once they have been coupled and decoupled once. One theory behind this apparent deactivation is detachment from one or both SO chain ends after dimerization as evidenced by the reduction of anthracene proton peaks at 7.3-8.75 ppm over progression of the cycle.
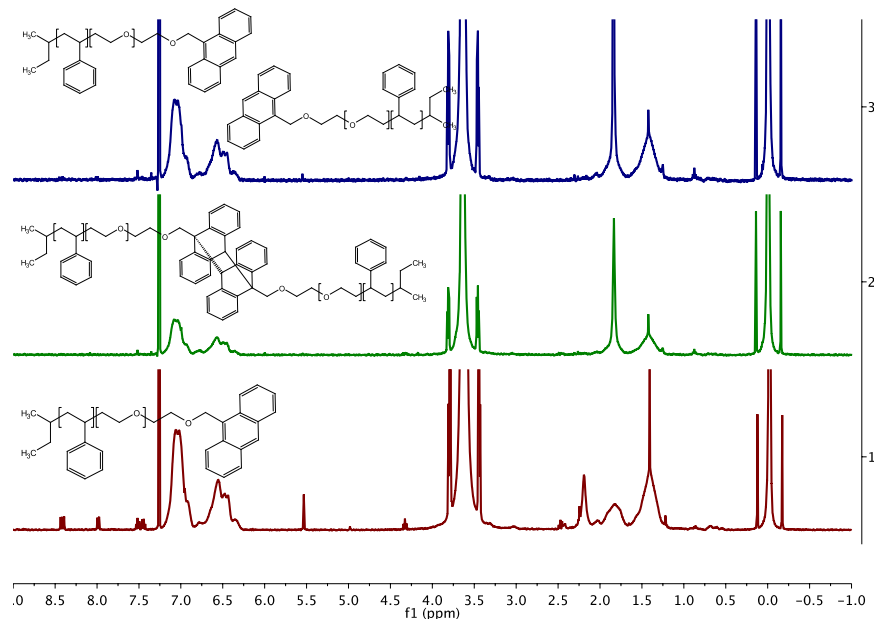
Figure 4.10. Stacked NMR spectra of a full photocoupling cycle, **(1)** before exposure; **(2)** after photocoupling, **(3)** after decoupling.

The success in reversibly coupling free anthracene suggests the potential for an anthracene-function polymer to effectively, reversibly photocouple. However, SEC and NMR data show a limit in the amount of installed triblock copolymer (55% as evidenced in **Fig. 4.8**). One explanation for this discrepancy is that chain mobility is much lower than free molecule mobility,[10] therefore chain ends which are mobile in the melt are not able to move to allow for dimerization as free anthracene can. Additionally, the hydrophobic anthracene substituents of the SO micelles may be preferentially aligning to the hydrophobic and similarly structured PS cores as opposed to remaining as a shell of a dispersed, hydrated corona as assumed.

The detachment of anthracene from the SO diblock copolymer micelle coronas upon attempts to recouple may be due to radical instability stemming from the combination of UV irradiation, heat, and inadvertent exposure to oxygen despite the Ar purge. However, incorporation of BHT

as a radical inhibitor does little to positively affect coupling efficiencies and success of cyclic coupling in the amounts currently used (0.5 wt %), and also does not seem to aid in the prevention of the degradation seen in the right-hand shoulder of SEC traces of long-irradiated samples. BHT may be running out by the completion of these long irradiation times, resulting in loss of the photoactive chain ends from radical instability.

4.4 Conclusions

4.4.1 Summary

In summary, a series of pre-structured hydrogels were built from self-assembled light-responsive BCPs of anthracene end-functional PS–*b*-PEO (SO-anth). Cyclic irradiation of these hydrogels showed minimal initial success, prompting study of the effect of the phenyl-based PS A block on coupling efficiencies. This was accomplished by comparing photocoupling behavior of PI-anth and PS-anth. However, limitations in equivalent experimental design to SO-anth studies resulted in solution-based coupling which inherently prevented conclusive evidence on the source of issues with cyclic coupling in SO-anth systems, but seemed to suggest the source of instability was in phenyl radicals from the PS block. This led to fabrication of a PI-*b*-PEO (IO), but undesirable mechanical properties for membranes using IO hydrogels led to abandonment of this strategy. This returned us to use of the original SO-anth system from **Chapter 3**, though this time using a higher molecular weight SO-OH parent. These larger chains required longer irradiation times given under the same intensity conditions due to restricted chain mobility, and also reached a slightly lower maximum SOS production relative to its low M_n counterpart. However, this system confirmed the ability of SO-anth to controllably photocouple despite these deviations from the previously used material used for melt-state photocoupling studies discussed

in the previous chapter. While these hydrogels appear mechanically viable for UF membrane applications, they show resistance to recoupling due to apparent unavailability after a decoupling step, possibly due to poor dispersal and performance of the radical inhibitor used.

4.4.2 Future Directions and Considerations to Facilitate UF Membrane Development

Development of an SO-anth micelle-based ultrafiltration membrane was not continued past the above studies due to the suitability and pursuit of development of the material for other applications which did not require reversibility. This section serves to present potential future directions and considerations to facilitate continued development of the UF hydrogel membrane, in the event that this effort is resumed in the future.

4.4.2.1 Addressing radical instability

PS has been cited as a potential source of radically motivated instability in the SO-anth micelle construct. Another potential source of instability is the phenyl radicals from the anthracene substituent itself. This may be addressed by proper addition of BHT as proposed, but may also be circumvented or tested as the source of instability through development of a functional precursor with a longer carbon chain between oxygen from the parent SO-OH and the anthracene molecule, such as 9-chloropropyl anthracene. This increased distance between oxygen and anthracene may prevent the radical movement towards O to break the functionality. A final option that may or may not be addressed is replacement of the anthracene functionality with a different photocoupling terminal. The reason for resistance to this latter option is that in multiple sources anthracene is cited to be the terminal that achieves reversible photocoupling to the highest degree and is better understood than other molecules used for photocrosslinking. [5]

4.4.2.2 Minimizing defects for membrane development

This material has shown promise in UV-mediated SOS triblock copolymer tethering, and therefore, potential for mesh size tunability. There is also evidence for potential successful reversible tether removal. However, the fabrication method of the hydrogels themselves yield a large number of defects. Melt-pressing the material into disks then photocoupling them in the melt reveals a material that, upon cooling and vitrification of the PS cores, carries the bubbles and defects acquired from heat pressing and subsequent movement upon melting for photocoupling. Varied grain sizes before pressing tend to trap gaps and bubbles in the polymer, even under high pressure as visualized with magnetic resonance imaging (MRI) (**Figure 4.11**).
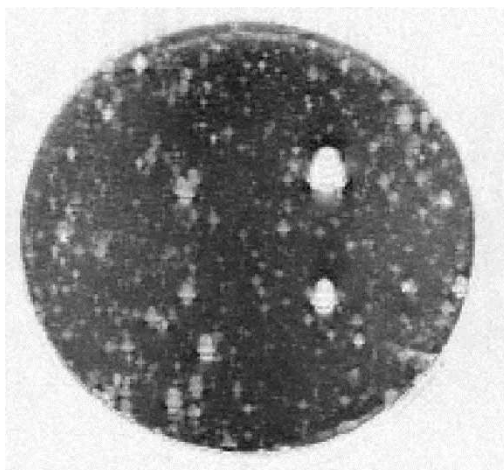
Figure 4.11. MRI scan of a swollen, melt-pressed hydrogel.

Screening isn't possible with such visible macroscopic defects, since the effectiveness of the membrane is compromised if defects exist which are larger than the targeted pore size. Applying vacuum to the polymer and mold while melt pressing tends to decrease the defects slightly, but does not completely remove them. To address this shortcoming, it may be advisable to form the network in solution rather than in the melt in order to increase homogeneity of the hydrogel, and decrease the macroscopic defects. Exploring the tethering behavior of free micelles in solution also presents the possibility of extended mesh-size and mechanical property tunability of the

76

photoactive TPE hydrogel. In-depth study of this solution-based photocoupling strategy is provided in **Chapter 5**.

4.4.2.3 Thin Film Fabrication

Hydrogels used for UF applications must be fabricated in such a way to consistently produce homogeneous thin-film membranes which can withstand significant pressures associated with the filtration process. One option to achieve this is to adapt the above-proposed solution-based system to be solution casted to form a uniform thin film. Highly concentrated viscous solutions may be applied using knife coating techniques to achieve this, while dilute systems could simply be cast and evaporated to reveal a thin, uniform film. These potential designs strategies for thin film membrane fabrication exemplify the ease at which these systems can adapted and the practicality in fabrication they offer. The micellar system can be produced through heated self-assembly, with spherical tethering occurring in situ via irradiation. Simple casting or flow techniques, with or without solvent, can be used to produce thin films of a tethered membrane. Preliminary experiments on the melt-state assembled films have been performed, and 7% triblock copolymer content membrane was able to withstand significant pressures (0.05-0.6 MPa) in dead-end filtration.

4.4.2.4 Improving membrane selectivity

Filtration membranes require appropriate base selectivity (or pore size) in order to be to perform effectively. While average micelle spacing of a particular network can be dicovered using SAXS, this alone is not a good estimate of pore size in the material. Chain entanglements in the network dictate pore size, which requires experimental correlations in order to more accurately predict pore size as a function of irradiation time. Based on preliminary experiments performed by Jackson T. Lewis examining a two-component, non-photoactive tethered micelle

system using SO with varying preblended SOS content, the selectivity of the membrane is limited. This study was aimed at determining how well this micelle network retained bovine serum albumin (BSA), a protein with dimensions of 140 x 40 x 40 Å and a molecular weight of 66.4 g mol^{-1}. Release profiles of BSA from a tethered hydrogel network demonstrated that increased tethering resulted in less released BSA (**Figure 4.12**), suggesting that BSA was to some extent being further retained with increased tethering and entanglements. However, the initial release rate was very high, which suggests that a denser mesh may be necessary for the hydrogel to perform effectively as an UF membrane.
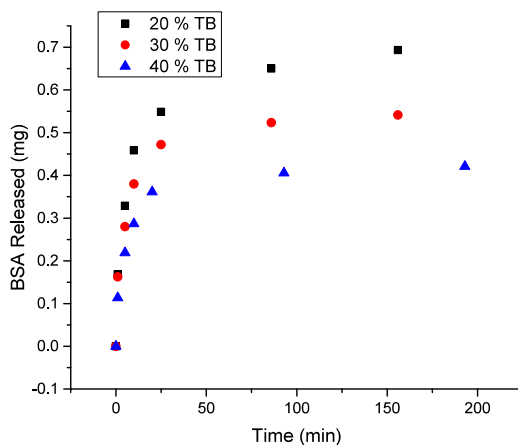
Figure 4.12. BSA release profile over time from a SO-based hydrogel for different concentrations of SOS triblock copolymer.

This experiment of BSA release form our hydrogel membranes provides a basis of understanding for how these hydrogels might function as separation membrane. Screening on the SO-anth membrane itself is still necessary to confirm this behavior, but based on this foundational system performance data, it is likely not selective enough for the intended application at this molecular weight and requires a higher tether density.

One proposal to achieve this finer mesh is to incorporate photoactive functionalities along the backbone of the PEO blocks at intervals which are ideal for photocoupling availability when self-assembled into photoactive micelles. This would require the presence of hydroxyl groups along the PEO chain backbone, to then be subsequently modified with anthracene as accomplished for end group functionality. This would potentially produce coronal micelles with higher concentration of photoactive tethering sites to result in a much higher tether density. Polymerized ethoxy ethyl glycidyl ether (PEEGE) can be used to provide the desired glycidyl ether backbone functionality when randomly or directly interspersed with PEO blocks, to form polyglycidol. The ability to polymerizing blends of EEGE and EO off of PS presents the opportunity to tune and fix the maximum density of hydroxyl backbone functionalities offshoots from a PEO chain (**Figure 4.13**).
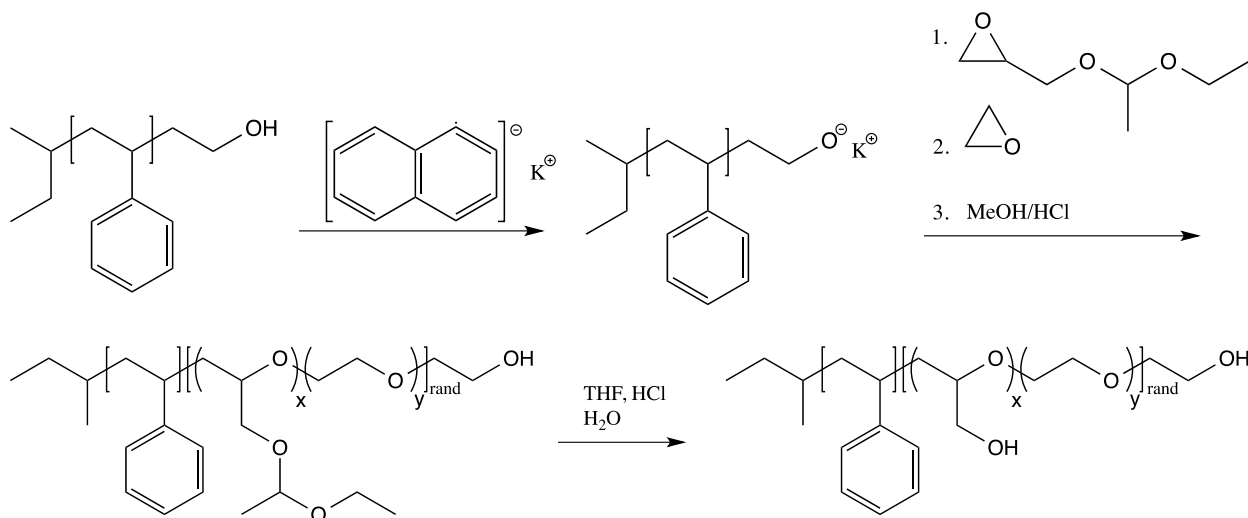
Figure 4.13. Synthetic scheme showing PS → PS-*b*-[(PEO)-(PEEGE)]$_{rand}$ → PS-*b*-[(PEO)-polyglycidol)]$_{rand}$.

4.4.2.5 Testing membrane filtration capabilities and fouling resistance

Once membranes are fabricated, their particular pore size must be determined through separation testing. SAXS can be used to determine intersphere spacing to be used as a lower limit of membrane porosity, and subsequently test base level separation capabilities of nanoparticles this size. Nanoparticles are suggested for initial pore-size determination due to the potential of biomacromolecules binding to the mesh to effect apparent pore size determination data. This can be accomplished through comparison of NP concentrations between both sides of the membrane, determined either through quantifying fluorescently tagged NPs or utilizing IR spectroscopy to acquire more accurate molecule concentrations. After initial screening with NPs is successful over membranes irradiated for a range of times, testing using biological molecules can be performed using HPLC. The goal is to have be able to tune to a large range of porosities, with the primary, preblended SOS mesh setting the lower limit of porosity, and the photo-installed SOS content providing tethers and entanglements serving to determine the upper limit of porosity.

4.4.3 Relevance to Dissertation Work

This chapter revealed the SO-anth BCP micelle system's inability to efficiently cyclically couple in the context of reversible tunabilty of an anti-fouling UF membrane construct. This discovery recommended a number of studies to be performed in the future in order to fully develop a viable TPE hydrogel UF membrane. However, this has little negative effect on the primary purposes of this dissertation work on developing a biomedically relevant and versatile hydrogel material. This shortcoming, for now, prove to be an advantageous quality of the construct given that an easily reversible system may in turn be easily decoupled. Loss of tethering in a biomedical context could have undesirable effects on mechanical properties of the

hydrogel from inadvertent UV exposure. That said, continuing studies on reversibility of the system may eventually contribute to increased versatility of this already highly tunable system.

4.5 Experimental

4.5.1 Materials and Methods

General. Styrene (99%, 50 ppm *p*-tert-butyl catechol inhibitor, Aldrich) and ethylene oxide (99.5+%, compressed gas, Aldrich) monomer were each purified by successive distillations (10-20 mTorr) from dried dibutylmagnesium (1 M solution in heptane, Aldrich) before use. Potassium naphthalenide was prepared according to the procedures from previous reports,[11] and sec-butyl lithium (1.3 M in cyclohexane/hexane solvent, Fisher) was used as received. 9-chloromethyl anthracene (≥98%, Aldrich) was either dried for a few hours prior to use or used as is for various experiments. Tetrahydrofuran (THF) was degassed by sparging with Ar for 45 minutes then purified over molecular sieve columns of neutral alumina (Glass Contour, Inc.). All reactions were performed in an air free environment (all vessels flamed under vacuum and backfilled with Ar at least three times), with those involving UV exposure performed under flow of Ar in open air. All other chemicals were used as received unless otherwise stated within text.

Synthesis of PS-OH. Purified styrene monomer (120.0 g, 1.14 mol, 20° C, Aldrich) was added under argon (3 psig) to a vigorously stirring solution of sec-butyl lithium (10.23 mL, 1.3 M in cyclohexane, Aldrich) and dry, air-free cyclohexane (1L, 20° C) in a 2 L reaction vessel. The vessel was stirred for approximately 8 hours after raising the temperature to 40° C. Purified ethylene oxide (EO) monomer (6.6g, 0.15 mol, 0 C, liquid) was then added to the reactor and the reaction was allowed to stir for an additional 24 hours at 40° C after which excess EO was purged from the reactor under Ar flow. The reaction was then terminated by addition of

methanol (50 mL). The PS-OH was precipitated in a 1:3 solution of isopropanol to methanol, filtered, and vacuum dried at room temperature for over 48 hours, resulting in a powdery white solid. Yield 116 g, 97%; GPC (THF, PS standard) M_w/M_n = 1.03; NMR (^{1}H, CDCl3) M_n = 8290 g/mol.

Synthesis of PS-b-PEO-OH (SO). SO diblock copolymer was synthesized by Dilanji B. Wijayasekara. Homopolymer A was dissolved in dry THF within an air free backfilled vessel. The solution was titrated with potassium napthalenide (KNap) in THF until a pale green color was visible and held constant for around 20 minutes. The reactor was heated to 40° C and purified EO was added under Ar while stirring. The reaction was allowed to run for 48 hours and resulted in a white, powdery solid. GPC (THF, PS standard) M_w/M_n = 1.08; NMR (^{1}H, CDCl3): M_n = 106,373 g/mol.

Synthesis of PS-b-PEO-b-PS (SOS). SOS triblock copolymer was synthesized by Dr. Chen Guo. Dry THF was put into an air free reaction vessel. Dibromoxylene (DBX) (0.283 g) was then dissolved in this to produce a solution of 0.0136 M. material SO (4.977 g) was dissolved in dry THF in a separate reaction vessel. The solution was then titrated with KNap as previously described, and then CsI was added to the reaction under Ar before addition of 5 mL of 0.0136 M solution of DBX. The reaction was stirred overnight and precipitated into pentane 2 times, then isolated and dried. This resulted in an off-white solid. Yield 4.9+ g, 98+%. SEC (DMF, PEO std): 83.7 wt%, 72.0 mol% triblock copolymer; NMR (^{1}H, CDCl3) $M_{n,SOS}$ = 183,000 g/mol.

Synthesis of PS-b-PEO-anthracene (SO-anth). SO-OH diblock copolymer (5.15 g) was dried overnight in an evacuated, flamed, then backfilled reaction vessel after addition of SO-OH to the vessel under positive flow over Ar. ~300 mL of dry, air-free THF was added via cannula to the reaction vessel and stirred until all polymer was dissolved. The solution was titrated using

concentrated KNap in dry THF as previously described. Dry 9-chloromethyl anthracene was then added to the stirred solution in the reaction vessel under positive flow of Ar. The solution turned an amber-brown color and was allowed to stir overnight. Extra THF was removed using a rotary evaporator, leaving about 50 mL in order to remove product from the vessel with ease. This 50 mL THF/SO-anth solution was precipitated into cold stirred pentane, and immediately formed a fluffy yellow-white solid. This solid with added BHT was redissolved and precipitated twice more, then a small portion was kept aside to dry for use in NMR characterization. Before being precipitated a final time, BHT was added to the dissolved solution which was then isolated and dried under vacuum for five days. Yield 4.73 g, 91.8%. GPC (THF, PS standard): M_w/M_n = 1.125.

Synthesis of PI-OH. PI-OH was synthesized by Dilanji B. Wijayasekara. Anionic polymerization of isoprene was initiated with sec-butyllithium in 1L of cyclohexane at 40°C under a positive argon pressure of 1 psi. Ethylene oxide was added as an end-capping agent. The terminal alkoxide was quenched with acidic methanol (70:1 MeOH: HCl), and the cyclohexane polymer solution was reduced to 500 mL on a roto-evaporator. The product precipitated from 4:1 MeOH: EtOH. The polymeric alcohol was dissolved in benzene and freeze-dried in vacuo (25 °C, 24 h). Recovered sticky clear viscous liquid. GPC (PS standards): M_w/M_n = 1.06; NMR (^{1}H, CDCl3): M_n =8450 g/mol.

Synthesis of PS-anth and PI-anth. A procedure identical to that of functionalization of SO-OH with anthracene was performed to functionalize PS (1.007 g, using PS-OH described above) and PI (1.03 g, using PI-OH described above) directly with anthracene. The resulting PS-anth polymer was a mildly tacky off-white powder, GPC (THF, PS standard): M_w/M_n = 1.04. The

resulting PI-anth polymer was a very viscous yellow fluid, GPC (THF, PS standard): M_w/M_n = 1.112.

4.5.2 Measurements

NMR. Nuclear magnetic resonance (NMR) was used to confirm the chemical structure of species used within this project. ^{1}H NMR spectra were collected at room temperature in $CDCl_3$ on a Varian Inova 400 MHz Spectrometer using a 5 to 30 second relaxation delay and 32 to 128 scans. Spectra were collected for all batches of synthesized material, as well as parent materials. End group analysis serves to provide a baseline for quantifying repeat units in a structure and thus determining M_n. The set of peaks shown in the 0.5-0.8 ppm ppm range is the 6-proton initiator fragment (from sec butyl lithium) of all PS-containing polymers, which used to normalize the NMR spectra represent a single chain. The procedure is detailed below for the PS-OH spectrum as an example, and followed by integrated spectra of all remaining NMR run.

The first step is to identify the proton peaks for the initiator fragment. These are then integrated then normalized to six (to represent the six protons on the initiator fragment) for a single chain. The integration of the peaks representing the phenyl protons of the polystyrene block (6.25-7.40 ppm) after this normalization gives an estimate of the number of phenyl protons on one chain. This can therefore be used to calculate the number of repeat units of the chain by dividing the value from integration of the peak by five, for the number of protons on the phenyl group. This can in turn be multiplied by the molecular weight of the monomer to get an estimate of the polymer molecular weight. In the following analysis, n_I and n_P are the number of protons of the initiator and phenyl groups, A_I and A_P are the integral values of these respective proton peaks, and RU_I and RU_P are the respective repeat units of each.

PS-OH NMR analysis

PS dbw1-142
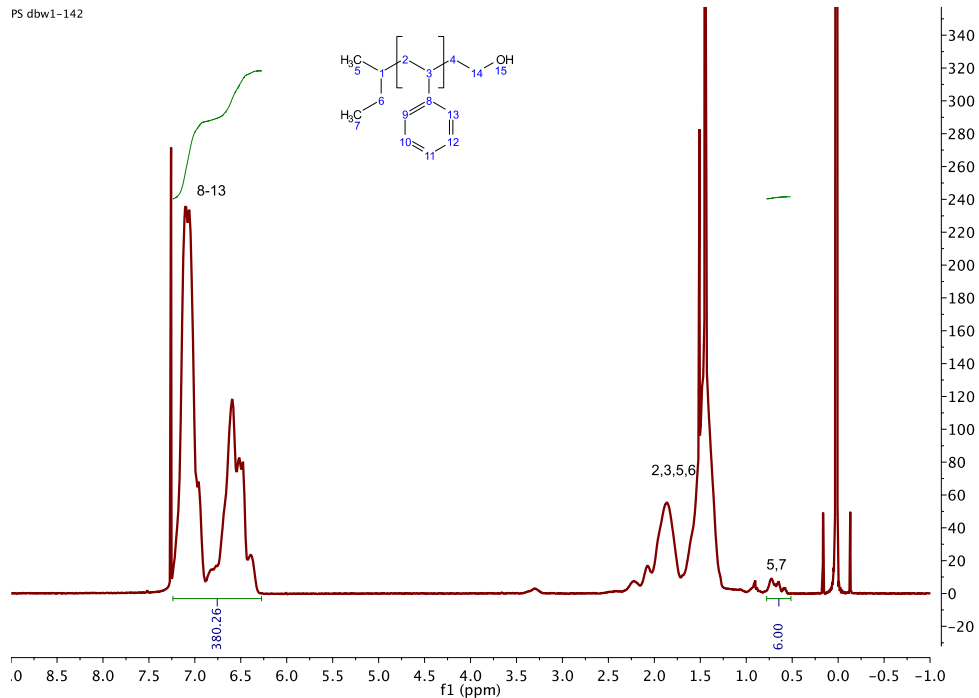
$$M_{n, \ styrene} = 104.15 \frac{g}{mol}$$

$$n_I = 6$$
$$n_P = 5$$

$$A_I = 6 \ for \ RU_I = 1$$

$$A_P = 380$$
$$RU_P = \frac{A_P}{n_P} = \frac{380}{5} = 76$$

$$M_{n, \ PS-OH} = (RU_P) * M_{n, \ styrene} = 76 * 104.15 \frac{g}{mol} = 7{,}915.4 \frac{g}{mol}$$

Though example analysis above was done on a homopolymer with a single type of repeat unit, similar analysis can be performed and the molecular weight of a BCP block can be extracted from the spectra by simply multiplying RU_I by $M_{n, \ I}$.

GPC. Gel permeation chromatography (GPC) was done on a Viscotek GPC-Max chromatography machine with three 7.5 x 340 mm Polypore columns in series, an Alltech

external column oven (40°) and a Viscotek differential refractive index (RI) detector. Characterization was performed with a THF mobile phase (1 mL/min) with PS standards.

GPC (or SEC, size exclusion chromatography) was primarily used to quantify coupling by determining the percentage of triblock copolymer installed within the light sensitive anthracene system. Peaks were fitted and integrated using OriginLabs software, and the integrated values were used to determine triblock copolymer content of the polymers. Equations and traces below denote these integration values as A, subscript TB or DB for triblock or diblock copolymer, respectively.

$$Mol\ \%\ TB = \frac{A_{TB\ peak}}{A_{TB\ peak} + A_{DB\ peak}}$$

SAXS. Small angle X-ray scattering (SAXS) analysis of BCPs used in this project was performed on a Rigaku S-Max 3000 High Brilliance 3 Pinhole SAXS System outfitted with a MicroMax-007HFM Rotating Anode (CuKa), Confocal Max-Flux Optic, Gabriel Multiwire Area Detector, and a Linkham thermal stage. Dry polymer sample were sandwiched between kapton windows (0.05 mm thick by 10 mm diameter). Exposure times were on the order of 3600 s at 100° C, and resulting SAXS data was azimuthally integrated.

UV Light Source. The light source used for photocoupling experiments is a 200 W mercury-xenon spot lamp (Hamamatsu LightningCure LC8 Series) fitted with either a 365 nm or a 254 nm band-pass filter depending on whether coupling or decoupling (respectively) is desired. The light guide was set about 1 inch from a TA Instruments ARES quartz parallel plate with a reflecting mirror tool used as a condensing lens. Intensity of the light source varied between experiments (25-49 mW cm^{-2}), but energy output from the lamp was consistent between all experiments (unless otherwise noted) by adjustment of exposure time.

The lamp was turned on for 15 minutes to 1 hour before use in order to stabilize. The intensity meter was placed the same distance away from the condensing lens as the sample would be, and the intensity was recorded at the point of highest intensity, which was visible as bright dot on the exposure surface. The intensity decreases radially and consistently from this point of highest intensity. Exposure time was determined based on a reference energy E. Calculation of this reference E was from an arbitrarily chosen initial experiment which yielded efficient coupling at t_{ref} = 40 minutes at I_{ref} = 33.1 mW cm^{-2}. Subsequent experiments used irradiation times (t) to match the reference energy, using the formula $t = t_{ref} * \frac{I_{ref}}{I}$.

A sample sandwiched between hydrophobic quartz slides or cover slips (25.4 mm diameter x 0.15-0.25 mm thick, Alfa Aesar) was put on the surface of exposure- a hot plate kept on for melt state exposure, or off for swollen state exposure. A flow of Ar was turned on when the light shutter was removed, and the sample was exposed to light for a time t. The sample was flipped over at t/2, and let cool after removing from the heated surface before being separated from the quartz sandwiching it to prevent tearing or sticking.

Rheology and Mechanical Testing. Rheological data was obtained using a TA Instruments ARES rheometer. Copolymer samples for melt rheology were pressed as solid disks (8 x 1 mm, 150 °C, 500 psi for 60 s). Disks were positioned between two parallel plates (8 mm diameter). The rheometer parallel plates were heated to 75 °C and the gap was reduced and adjusted to ensure even distribution of the sample (typical gaps were 0.5–0.7 mm). Dynamic temperature ramp tests were performed while heating and cooling at 1 °C min-1 at angular frequency of 1 rad/s and a strain of 5 % (well within the linear viscoelastic regime, determined by dynamic strain sweep experiments for each copolymer). Rheological swollen hydrogel frequency sweep and compression experiments were run at room temperature using a water bath lower tool

apparatus and an 8 mm stainless steel upper parallel plate. Before starting the rheological experiments, hydrogels were blotted dry with KimWipes and humidity covers were placed over the water bath to prevent evaporation. A constant force was applied (10 % compression) to all hydrogel samples to prevent slip. Strain rates were adjusted depending on the linear viscoelastic regime (typically 0.1–1%).[7]

Procedures and data from tensile testing in this document are the work of Dr. Chen Guo. Tensile tests were carried out on rectangular pieces of hydrogel sample cut to approximately 14 mm width with thickness that varied from 0.442 to 0.875 mm. All tensile tests were run at room temperature using the normal force transducer of a TA ARES rheometer. TA rectangular torsion geometry test fixtures were used as tensile test grips, although the grip surfaces were modified with 600 grit sand paper to eliminate slip. The experimental setup and strain rate used were similar to that reported Schmidt et al.[12] with some minor adjustments. A strain rate of 5 mm/s was applied until complete hydrogel fracture. The strain rate was chosen to minimize slip while ensuring the maximum travel distance could be covered in less than 0.5 minutes, such that surface evaporation during testing could be minimized. Stress was calculated as the force normalized by the initial cross sectional area of each sample (engineering stress).[13]

4.6 Supporting Information

4.6.1 Synthetic schemes
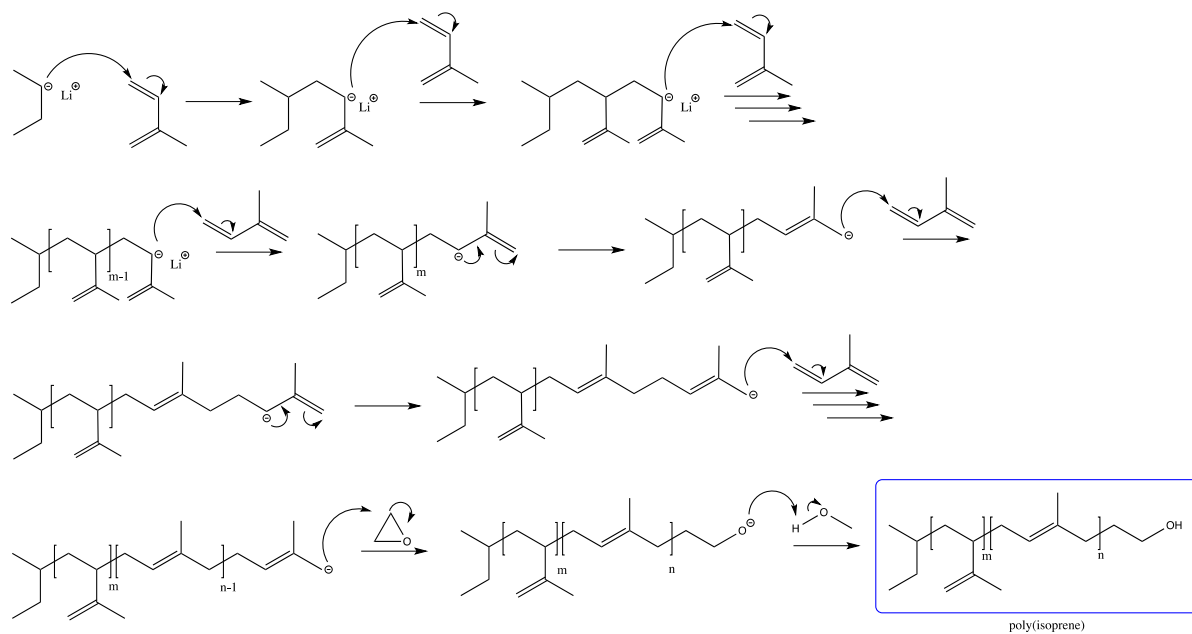
Scheme S4.1. Synthesis of PI-OH
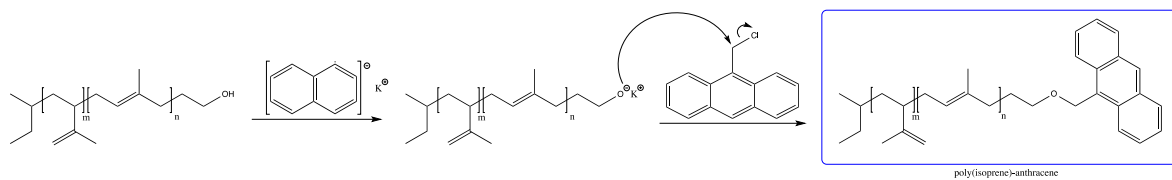
Scheme S4.2. Mechanism for synthesis of PI-anth from PI-OH

4.6.2 Cyclic coupling data

(a)

(b)
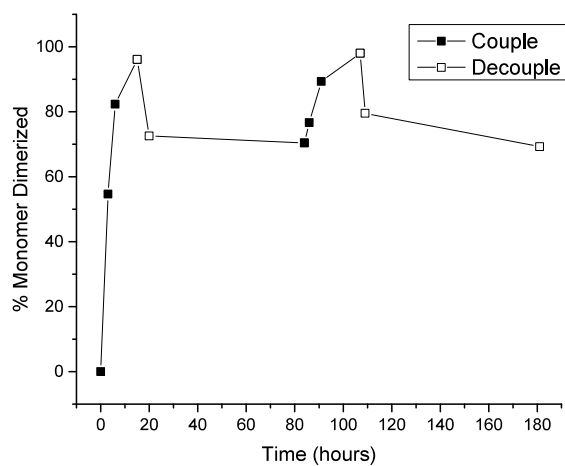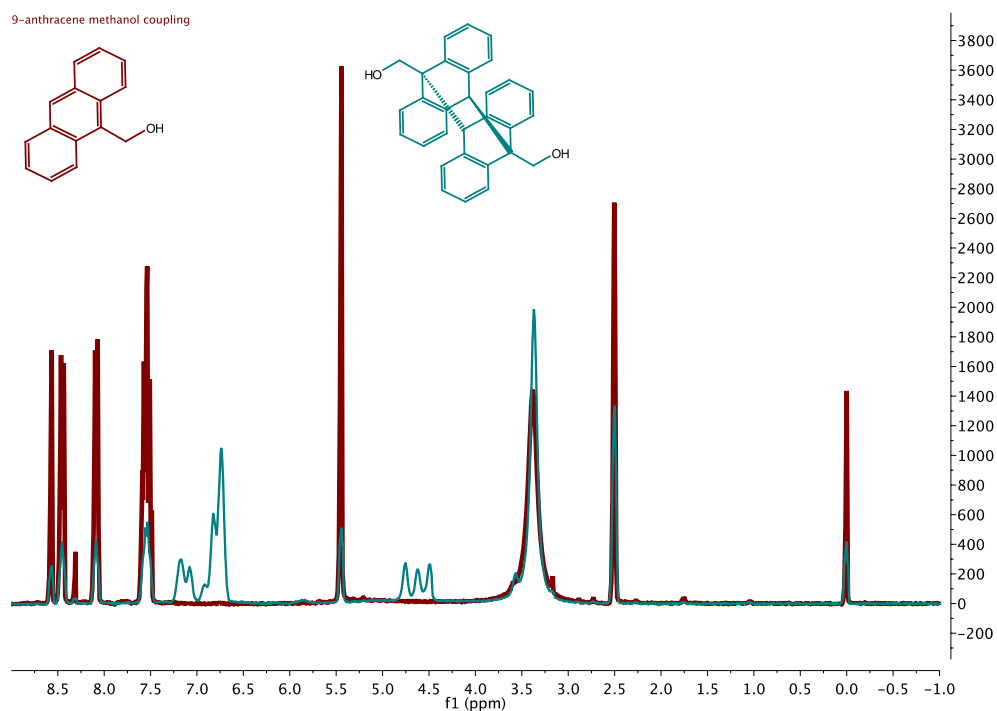
Figure S4.1. 9-anthracene methanol **(a)** shown reversibly dimerizing through % dimerized as a function of UV exposure time, and **(b)** superimposed ^{1}H NMR data from before and after dimerization.

4.6.3 Sample Identification History

Table S4.1.

Manuscript ID	Lab Notebook ID
PS	DBW1142
PS-anth	NH1132
PI	DBW2X (7/2/14)
PI-anth	NH1141
SO	DBW1170
SO-anth	NH1196

References

1.   Ferry, J. D. Ultrafilter membranes and ultrafiltration. *Chem. Rev.* **1936,** 18, (3), 373-455.

2.   Lau, W. J.; Goh, P. S.; Ismail, A. F.; Lai, S. O. Ultrafiltration as a pretreatment for seawater desalination: A review. *Membr Water Treat* **2014,** 5, (1), 15-29.

3.   Mohammad, A. W.; Ng, C. Y.; Lim, Y. P.; Ng, G. H. Ultrafiltration in Food Processing Industry: Review on Application, Membrane Fouling, and Fouling Control. *Food Bioprocess Tech* **2012,** 5, (4), 1143-1156.

4.   Huq, N. A.; Ekblad, J. R.; Leonard, A. T.; Scalfani, V. F.; Bailey, T. S. Phototunable Thermoplastic Elastomer Hydrogel Networks. *Macromolecules* **2017,** 50, (4), 1331 - 1341.

5.   Wells, L. A.; Brook, M. A.; Sheardown, H. Generic, Anthracene-Based Hydrogel Crosslinkers for Photo-controllable Drug Delivery. *Macromol Biosci* **2011,** 11, (7), 988-998.

6.   Zheng, Y.; Micic, M.; Mello, S. V.; Mabrouki, M.; Andreopoulos, F. M.; Konka, V.; Pham, S. M.; Leblanc, R. M. PEG-Based Hydrogel Synthesis via the Photodimerization of Anthracene Groups. *Macromolecules* **2002,** 35, (13), 5228-5234.

7.   Scalfani, V. F. Part I — Access to UV Photocured Nanostructures via Selective Morphological Trapping of Block Copolymer Melts. Part II — Morphological Phase Behavior of Poly(RTIL) Containing Block Copolymer Melts. Ph.D. Dissertation, Colorado State University, Fort Collins, Colorado, 2012.

8.   Li, T.; Zhou, C. L.; Jiang, M. Uv Absorption-Spectra of Polystyrene. *Polym. Bull.* **1991,** 25, (2), 211-216.

9.   Guo, C.; Bailey, T. S. Tailoring mechanical response through coronal layer overlap in tethered micelle hydrogel networks. *Soft Matter* **2015,** 11, (37), 7345-7355.

10.   Hiemenz, P. C.; Lodge, T., *Polymer Chemistry*. 2nd ed.; 2007.

11.   Scalfani, V. F.; Bailey, T. S. Thermally Stable Photocuring Chemistry for Selective Morphological Trapping in Block Copolymer Melt Systems. *Chem. Mater.* **2010,** 22, (21), 5992-6000.

12.   Gaharwar, A. K.; Dammu, S. A.; Canter, J. M.; Wu, C. J.; Schmidt, G. Highly Extensible, Tough, and Elastomeric Nanocomposite Hydrogels from Poly(ethylene glycol) and Hydroxyapatite Nanoparticles. *Biomacromolecules* **2011,** 12, (5), 1641-1650.

13.   Guo, C.; Bailey, T. S. Highly distensible nanostructured elastic hydrogels from AB diblock and ABA triblock copolymer melt blends. *Soft Matter* **2010,** 6, (19), 4807-4818.

Chapter 5.

Melt-fabricated photoreactive block copolymer micelles as building blocks for tunable elastomeric hydrogels

5.1 Summary

Soft, conformally-shaped thermoplastic elastomer (TPE) hydrogels producible from a moldable precursor material are desirable in many biomedical, surgical, and pharmaceutical applications. A new class of hydrogel networks was developed by employing photocurable, moldable solutions of melt-assembled spherical micelles formed from ω-anthracenylpolystyrene-*b*-poly(ethylene oxide) diblock copolymer. Curing was accomplished using photoinduced [4+4] cycloaddition ($\lambda = 365$ nm) of the terminal anthracene groups populating the hydrophilic corona of each micelle. This chain coupling reaction produces polystyrene-*b*-poly(ethylene oxide)-*b*-polystyrene triblock copolymer tethers which adjoin adjacent micelles. The micelle structure was generated using melt state self-assembly, rapidly producing structural uniformity among micelles as confirmed using SAXS, cryo-TEM, and DLS. Homogeneous dispersal of the assembled micelle building blocks in water resulted in spreadable or moldable photoactive micelle solutions. Four concentrations (8, 12, 16, 20 g water/g polymer) were studied for their ability to form elastomeric hydrogels once irradiated. The stability of the precursor micelle solutions was confirmed over a period of nine weeks, showing no significant change in micelle size distribution. Once in molds, these solutions of varied concentration were then irradiated over a range of times (2.5 – 7.5 min) to form soft TPE hydrogels (dynamic shear G' = 0.6 to 3.3 kPa)

with prescribed shape consistent with high fidelity conformal fill. The amount of installed triblock copolymer was dependent on irradiation time, which in combination with the initially chosen micelle concentration, could be used to dictate hydrogel mechanical properties. This ability to photoinstall tethers *in situ* also presented the opportunity to introduce shape through photopatterning.

5.2 Introduction

Polymeric hydrogels are used in a large range of applications including separation membranes,[1, 2] pharmaceuticals,[3-6] biomedical materials,[7-11] cosmetics and personal hygiene products.[6, 12, 13] The efficacy of any particular hydrogel system does, however, require its properties be tailorable to the performance demands of the intended application. Factors such as mechanical behavior, malleability, chemical functionality, or biocompatibility, for example, must often be taken into account. Here, we disclose a versatile hydrogel system based on melt-fabricated photoreactive block copolymer micelle precursor solutions which exhibit an ability to be easily molded into specific shapes, and subsequently photocured to create soft, yet elastomeric solids. Such materials have implications in facets of the above-mentioned application areas where an ability to generate a flexible hydrogel conformally shaped to the surrounding features is extremely desirable.[13]

Our group has been exploring the use of efficient sphere-forming block copolymer (BCP) morphologies as a foundation for a new class of thermoplastic elastomer (TPE) hydrogels.[14-17] These morphologies are generated by blending AB diblock and ABA triblock copolymers of a defined A-block volume fraction[18] chosen to drive formation of a periodic network of spherical micellar-shaped aggregates. The A and B blocks are selected such that the core (A blocks) of the

spherical aggregate is intrinsically hydrophobic and glassy, while the corona (B blocks) is water-soluble. In these systems, the role of the ABA triblock copolymer is to bridge or tether adjacent spherical micelles. Much of this work has focused on the use of ABA triblock copolymer concentration as a dial through which the hydrogel mechanical properties can be tuned, with considerable effort spent on achieving high-modulus, fatigue resistant systems formed entirely in the melt state. However, by requiring the introduction of ABA triblock copolymer tethers during melt-state self-assembly, shape in these systems must be set during thermal processing (100 – 200 ˚C). This limits direct incorporation of thermally sensitive additives (e.g, pharmaceuticals, living cells, etc.), and precludes use in point-of-care applications in which ambient temperatures and conformal shaping prior to gelation is advantageous.[14-16]

The aim of this work was to adapt our original TPE hydrogel system to one in which the basic micellar building blocks could now be dispersed into moldable solutions prior to network formation at ambient temperatures. The key challenge was to develop a system which would allow the thermal processing step required for micelle formation to be divorced from network formation. Our solution to this challenge is based on the replacement of the original AB/ABA BCP blend with a single component AB diblock copolymer end-modified with a photodimerizable substituent (**Figure 5.1a**). This strategy permits the untethered micelles formed during melt processing to be easily dispersed in solution, prior to light-triggered chain coupling between micelles to induce network formation. This, in turn, allows us to maintain the efficient tethered-micelle network architecture of the original blended system while using only a single photoactive BCP species. The model system chosen to validate this new approach was a polystyrene-*b*-poly(ethylene oxide) (SO) diblock copolymer end-modified with anthracene (SO-anth). The SO-anth BCP volume fraction was specifically synthesized to produce micellar

building blocks containing a glassy polystyrene core with water-soluble poly(ethylene oxide) coronal layers. [18-21] Solutions of these micelles, when UV-irradiated (λ = 365 nm), form symmetric polystyrene-*b*-poly(ethylene oxide)-*b*-polystyrene (SOS) triblock copolymer tethers *in situ,* through a [4+4] photocycloaddition reaction between terminal anthracene substituents.

These moldable micelle solutions could be rapidly transformed with only minutes of UV exposure to soft, elastomeric hydrogels. The resulting solids preserved their shape once removed from their molds and maintained a low enough modulus to remain highly flexible. The experiments in this study examine how such attractive properties emerge by closely examining the influence of integrated anthracene substituents on the micelle self-assembly process, the stability of the dispersed micelles in solution over time, and the effects of micelle concentration and UV irradiation time on the mechanical properties and swelling behavior of the hydrogel networks produced using this novel approach (**Figure 5.1b**).
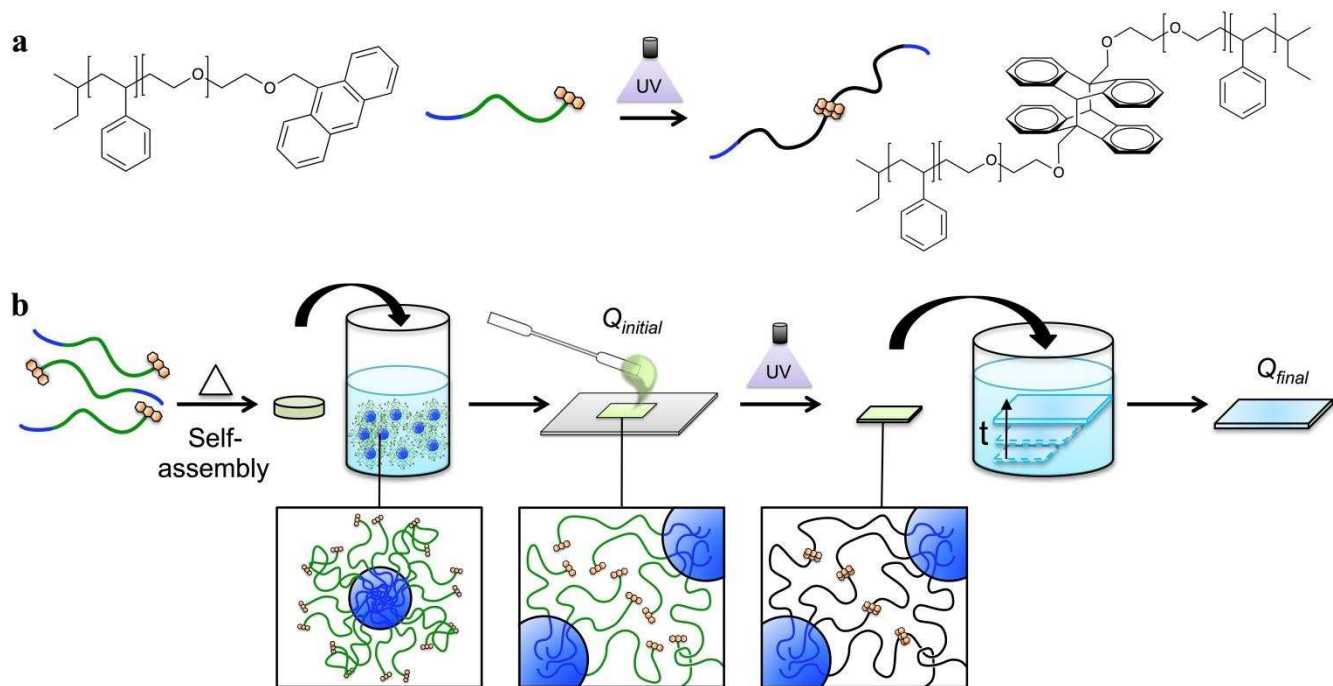
Figure 5.1. (a) Anthracene-functional SO (SO-anth) can be photocoupled to form SOS *in situ* using UV light. **(b)** SO-anth is self-assembled in the melt to form photoactive micelles comprised of glassy PS cores and hydrophilic PEO coronas. These untethered micellar building blocks are dispersed in water (before any UV irradiation) to form viscous solutions of known ratios of water to polymer ($Q_{initial}$). These solutions can then be poured or smeared into a mold and UV-irradiated to form SOS triblock copolymer tethers *in situ*, producing the network architecture. The resulting hydrogel network, which is at the same $Q_{initial}$ as before solution molding and irradiation, retains the shape it was cured in. It is then placed in excess water and allowed to swell to its equilibrium dimensions characterized by Q_{final}, retaining its original (albeit enlarged) shape.

5.3 Results and Discussion

5.3.1 Synthesis and Structure SO-anth Micellar Building Blocks

The synthesis of the SO-OH diblock copolymer ($f_{PS} = 0.122$, $M_n = 73800$ g mol^{-1}, PDI = 1.04) parent to the SO-anth was carried out using anionic polymerization techniques.[14] End-functionalization of the SO-OH with anthracene was accomplished through displacement of the chlorine on 9-chloromethyl anthracene by nucleophilic substitution, using the potassium alkoxide of the terminal hydroxyl end-group of SO-OH.[22] Functionalization was estimated to be approximately quantitative using ^{1}H-NMR peak integrations (**Figure S5.1**). The molecular weight distribution of the SO-anth product was confirmed using size exclusion chromatography (SEC) and resembled that of the parent SO-OH, indicating no evidence of chain degradation. However, a small amount of premature chain coupling was apparent, likely due to inadvertent light exposure during regular handling, during SEC sample preparation (**Figure S5.1, inset**).

This SO-anth product was then used as the sole polymeric component in this solution-based pourable hydrogel fabrication method, effectively comprising three steps. First, the block copolymer was self-assembled in the melt to form spherical micellar structures, containing a hydrophobic polystyrene core and a poly(ethylene oxide)-anthracene corona. Next, these photoactive micelles were combined with water in specific ratios to form solutions of varying viscosity and micelle concentration (and thus mean inter-micelle spacing). Finally, these micelle solutions could be poured or smeared into molds (depending on solution viscosity), and photocoupled using UV light (λ = 365 nm, I = ~30 mW cm^{-2}). This exposure induced dimerization of the terminal anthracene substituents, creating tethers (network strands) between micellar building blocks. The resulting soft thermoplastic elastomer hydrogels produced from this three-step process could then be placed in water and allowed to swell to their final equilibrium dimensions.

The BCP volume fraction was selected such that phase separation in the melt produces spherical micelles.[18, 19, 23] Phase separation at such volume fractions can produce spherical micelles quite rapidly, but development of highly ordered lattices such as the preferred body-centered cubic (BCC) morphology can often require extended annealing. [23-26] Such annealing is necessary to overcome kinetic barriers related to chain entanglements or slow chain dynamics, which constrains early ordering to a liquid-like packing (LLP) of micelles,[14, 16, 17, 23] even at moderate molecular weights.[23-25, 27] Because of our intention to use these micelles as the fundamental building blocks comprising the final hydrogel network, it was critical to understand the role of the emergent BCC structure in the melt as an indicator of eventual micelle structural integrity and size distribution uniformity once in solution. SO-anth BCP pressed from a white

powder into yellow-tinged, translucent disks was subjected to various tests in order to further probe properties of these building blocks. (**Figure 5.2a**).

The transition from LLP to BCC in SO-anth was suspected to occur between 110 and 140 °C from a series of rheological temperature ramp measurements in which a clear increase in elastic modulus could be produced with extended annealing (**Figure S5.2**). To investigate this suspicion, small angle X-ray scattering (SAXS) data was collected on samples during annealing at 120 °C (following cooling from the disordered state). Evolution of the initially formed LLP phase to a BCC lattice was detected via the emergence of a clear diffraction pattern in the SAXS data after three to four hours (**Figure 5.2b**) of annealing time. A comparison of this self-assembly behavior to that of its SO-OH precursor (**Figure S5.3**) shows that while SO-OH seems to adopt a BCC structure slightly faster than SO-anth, the SO-anth diffraction pattern was ultimately more defined. Such subtle differences in phase behavior as a result of differences in chain end functionality have been previously documented.[28] The presence of the terminal anthracene functional groups seemed to also have a minor impact on the lattice constants ($a_{SO\text{-}anth}$ = 37.2 nm vs. a_{SO} = 37.8 nm) and chain aggregation numbers ($\theta_{SO\text{-}anth}$ = 221 vs. θ_{SO} = 232) produced in the final morphologies (**Table S5.1**). With such small differences, it is difficult to ascertain the role in which interactions among anthracene units or anthracene units and polystyrene domains are determining the subtle differences in morphological characteristics.

The evolution of the BCC morphology developed in SO-anth was probed using a rheological frequency sweep under oscillatory shear at 120 °C (ω = 1 rad s^{-1}, ε = 7%). At early annealing times, the morphological structure produced still exhibits terminal relaxation behavior consistent with liquid-like behavior of the micellar units. As annealing proceeds, this slope in log G' vs. log ω begins to evolve from its initial terminal value near two and slowly approaches zero (**Figure**

5.2c). This is consistent with the transition observed in the SAXS data, from a state with significant structural disorder, to that of a highly developed BCC lattice.[29] The rheology data indicates that the sample reaches its final plateau modulus after approximately 15 hours, after which no significant changes are apparent. Interestingly, there is no clear difference between the BCC diffraction pattern adopted after four hours of annealing and those recorded at the 15 or 24 hour time points (**Figure 5.2b**). This difference indicates that the rheological measurements are more sensitive to the evolving correlation among spheres of the BCC morphology than the SAXS measurements obtained using our laboratory-scale instrument. As before, a comparison of this rheological behavior to that of the SO-OH precursor (**Figure S5.4**) shows the evolution of the BCC structure occurs similarly, although slightly faster than SO-anth with terminal behavior indicative of less disorder at early annealing times.
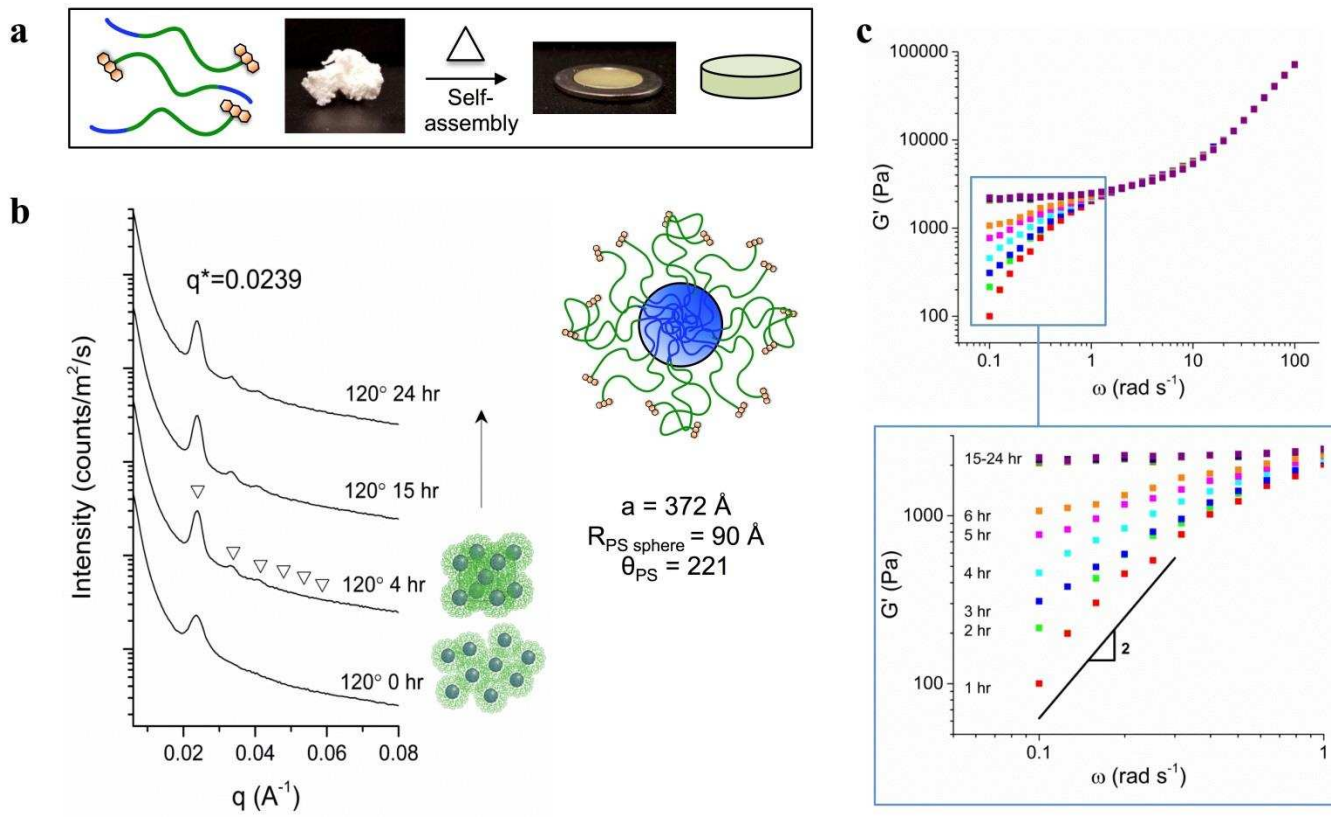
Figure 5.2. (a) SO-anth was pressed from a white powder into yellow-tinged translucent disks by heating to melt-state, inducing self-assembly into a periodic morphology of nanoscale micellar domains. The morphology and size of the micelles as a function of annealing time at 120 °C was investigated using **(b)** SAXS and **(c)** rheological frequency sweeps. Adoption of a BCC lattice appears to occur only after annealing of the samples for about four hours, with continued evolution of the morphology beyond four hours suggested by eventual formation of a plateau in the rheological data.

5.3.2 Pre-cure Micelle Solution Behavior

To form solutions of free micelles, disks of vitrified self-assembled SO-anth spheres were added to argon degassed DI water in specific ratios, quantified as $Q_{initial}$ (g water per g polymer). The micelles were allowed to passively disperse over 24 to 48 hours before being briefly vortexed to ensure even distribution and dissolution. The resulting homogenous mixtures were then given time to consolidate into clear viscous solutions, possessing a yellow tinge associated with the anthracene substituents (**Figure 5.3a**). Even though BCC organization is achieved only after prolonged annealing as seen in **Figure 5.2**, DLS data on solutions containing micelles at various extents of annealing showed no significant difference in hydrated micelle size distribution (**Figure S5.5**). This result suggests that the absence of the BCC morphology during melt assembly has no consequence with respect to micelle size inhomogeneity in solution on a level detectable by DLS, and that a brief heating step is sufficient to achieve uniformity in micelle size. This implies micelle fabrication times can be greatly reduced, in that the extended annealing needed for BCC morphology development is unnecessary in terms of micelle uniformity, size, or structure once dispersed in solution. The ability to produce micelles of relative uniformity without long processing times is an attractive feature of these systems.

102

To assess micelle stability in water, solutions were analyzed over a period of nine weeks. DLS was used to identify undesirable dissolution or aggregation of micelles and SEC was used to detect potential BCP chain degradation. DLS data showed consistency in the SO-anth micelle size distribution over the nine-week period, with no evidence of dissolution or aggregation (**Figure 5.3b**). The only discernible difference in DLS data between weeks one and nine was a slight narrowing in the size distribution seen both in SO-anth and SO-OH micelles. We believe that such narrowing in the calculated distribution is likely associated with changes in diffusive characteristics (hydrodynamics) of the micelles with time, and not a product of actual changes in the number of chains per micelle aggregate. This would be consistent with the vitreous nature of the polystyrene cores, long-term shape preservation previously observed in our TPE hydrogel systems,[14-17, 30] and the demonstrated non-ergodicity of BCP micelles,[31] all of which suggest room temperature chain exchange among micelles is essentially non-existent over this time scale. Additionally, SEC measurements confirmed the absence of chain degradation over the nine-week period, although a small amount of photocoupling was detected by week nine (**Figure S5.6**). We suspect that the appearance of SOS in the SEC data is a result of inadvertent light exposure over the nine-week period and is essentially limited to intra-coronal dimerization of SO-anth chains, as we did not observe micelle aggregation in the DLS data. The stability of the system was also apparent in the SO-OH precursor confirmed using DLS (**Figure 5.3b**) and SEC (**Figure S5.6**) data.

Micelle dimensions and size uniformity were confirmed using cryogenic transmission electron microscopy (cryo-TEM). Micelles were prepared using two processing methods. The first was our preferred method of self-assembly without extended annealing. The second involved annealing at 120 °C in a SAXS instrument until BCC organization was confirmed, followed by

quenching from 70 °C, just above the PEO crystallization temperature (**Figure 5.3c**). Quenching in this manner was done in an attempt to maximize retention of the morphological characteristics developed in the melt. Cryo-TEM images of micelles produced by either processing method contain dark regions consistent with dimensions of the PS cores expected from the SAXS data (~18 nm diameter, **Figure 5.3d**). As expected, the highly hydrated PEO coronas cannot be distinguished from the background solution due to similarities in electron density. However, the regular spacing between the PS cores implies micelle dimensions (~122 nm, core-to-core) that are consistent with the hydrodynamic diameter suggested by the DLS data (~128 nm). Interestingly, both preparation methods yielded non-spherical PS cores. In theory, while the distortion in shape could be associated with random fluctuations in core domain shape in the melt that are trapped during vitrification, we suspect it is more likely a product of PS domains being unable to fully vitrify prior to PEO crystallization near 65 ˚C. That is, the domains experience strain-induced deformation[14, 32] as a result of crystallite formation in the surrounding PEO matrix. This would be consistent with our previous DSC data, which suggests the PS T_g in the nanoscale domains may be depressed from its expected bulk value (~80 ˚C).[14] This would also explain the limited efficacy of our attempt to suppress the effects of crystallization and retain morphological characteristics of the developed BCC lattice through quenching from just above the PEO crystallization temperature.
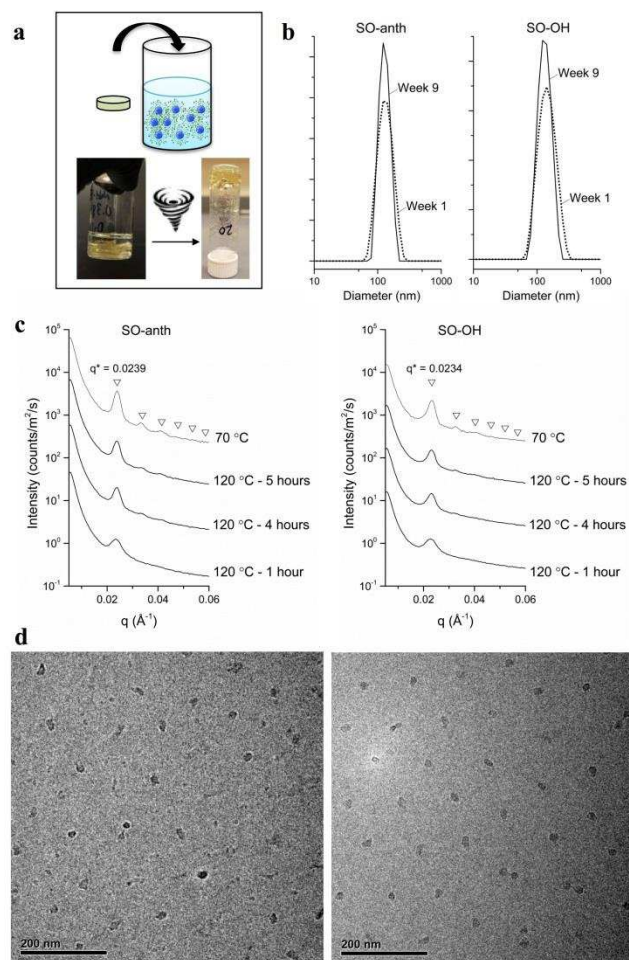
Figure 5.3. (a) Self-assembled micelles were combined with water and then vortexed to form a viscous, yellow-tinged solution. **(b)** Micelle stability and behavior in water was monitored over nine weeks using DLS, during which there was no evidence of aggregation. **(c)** SAXS data confirmed the emergence of BCC morphology after four hours of annealing at 120 °C, with persistence of this organization upon cooling to 70 °C, prior to quenching. **(d)** Cryo-TEM images of micelles produced after quenching melt blends from 70 ˚C followed by dispersion of micelles in water (SO-anth: left, SO-OH: right). Images showed evenly spaced micelles with identifiable non-spherical PS cores. Hydrated PEO coronas appear indistinguishable from the surrounding solution.

5.3.3 UV-Triggered Hydrogel Formation

In this study, solutions with water to polymer mass ratios ($Q_{initial}$) between 8 and 20 g water per g polymer were spread into molds, sandwiched between hydrophobic glass slides, and exposed to UV light (λ=365 nm, I ~ 30 mW cm^{-2}) for up to 7.5 min to form soft hydrogels (**Figure 5.4a**). These hydrogels could then be swollen to new equilibrium dimensions in argon-degassed water, as a result of the system's thermodynamic requirement to balance the osmotic swelling forces against the entropic resistance to swelling provided by the newly formed tethers (**Figure 5.4d**). This new equilibrium ratio of water to polymer (referred to as Q_{final}) notably always exceeded $Q_{initial}$ for the system, a result of being able to swell beyond the minimal initial stress state of the tethers at the time of installation (at Q_{intial}).

To study the effect of irradiation time on SOS concentration and, ultimately, the hydrogel mechanical properties, solutions of $Q_{initial}$ = 16 g water per g polymer were placed in glass-sandwiched molds and exposed to UV light for a total of 2.5, 5, and 7.5 min. Molds were flipped over halfway through the targeted irradiation times in order to ensure equivalent exposure from top and bottom, providing axially symmetric tether installation. SEC data showed installed SOS content increased with increasing exposure time, with a majority of the SOS triblock copolymer formation occurring within the first 2.5 minutes (**Figure 5.4b**). We suspect that the rapid coupling is a consequence of a tendency for terminal anthracene units to pre-organize through π-π stacking[33] and hydrophobic interactions in water. Notably, extended irradiation past this time did not appear to increase the SOS content to a great extent. This is thought to be a product of highly spaced photoactive micelles in these dilute systems, as well as intrinsic local constraint of chain ends anchored in the micelle core. After swelling the photocoupled samples to equilibrium (Q_{final}), dynamic frequency sweep data (ω = 0.1−100 rad s^{-1}) displayed plateau behavior

(frequency independence) in the elastic moduli, typical of elastic solids.[29] The mean elastic modulus extracted from each of these sweeps was positively correlated with UV exposure time, indicating increased modulus with increasing triblock copolymer content (**Figure 5.4c**). Our previous studies on melt systems suggest this increase in modulus is not only due to the increase in network strands (tethers) in the system, but also the result of increased overlap between coronal domains at Q_{final}. This increased overlap is a result of restricted swelling imposed by entanglements trapped among the strands during photocoupling.[15] In a proof-of-concept study immediately preceding this work, we investigated the photocoupling potential of SO-anth in the dry melt state where the concentration of chain ends is maximized.[17] Equilibrium-state hydrogels formed from these initial studies through melt photocoupling exhibited moduli in the range of G' = 1-100 kPa. In contrast, the elastic shear modulus values of hydrogels made as a result of photocoupling $Q_{initial}$ = 16 solutions (G' = 0.6-2.1 kPa) were significantly lower. We suspected that the reduced moduli produced during solution coupling were a direct consequence of fewer entanglements among the tethering chains (strands) during UV irradiation, in contrast to their melt-photocoupled counterparts. This observation suggested a high potential to tailor the modulus of the resultant hydrogels through adjustment of micelle concentration. That is, changing the water-to-polymer ratio would directly influence the mean spacing between micelles, controlling the coronal overlap and entanglement density at the time of photocoupling. Additionally, the decreased micelle proximity relative to the melt-photocoupled system increases the probability of intramicelle photodimerization, resulting in a fraction of the SOS triblock copolymer formed having PS end blocks that occupy the same micelle core. These looping SOS chains, while not distinguishable from tethering SOS chains experimentally, still contribute to the measured SOS content using SEC. However, looping SOS chains are unlikely to contribute

107

to the mechanical properties of the hydrogel network, further emphasizing the influence of micelle concentration during hydrogel formation.

To test this theory, solutions of $Q_{initial}$ = 8, 12, 16, and 20 g water per g polymer were spread into glass-sandwiched molds and then exposed to UV light for 5 minutes before swelling to Q_{final}. Interestingly, the values of Q_{final} were only moderately influenced by $Q_{initial}$ solution concentrations, each appearing to approach a mean final value between 18 and 21 g water per g polymer (**Figure S5.7**). In fact, the difference between Q_{final} and $Q_{initial}$ appears to diminish with increasing $Q_{initial}$, with minimal additional swelling occurring after photocoupling at $Q_{initial}$ = 20. Hydrated micelle dimensions estimated using Cryo-TEM images show consistent core-to-core distances in the 120 nm range, which roughly corresponds to Q values near 30 g water per g polymer, based on estimates of volume occupied per hydrated micelle. Assuming the close micelle packing observed in the images is representative of the length scale at which the coronal chains of the micelles just begin to interact, tethers formed at $Q_{initial}$ = 20 occur at a point of minimal coronal overlap (approximately 5 nm). Thus, at dilute $Q_{initial}$ values, the tethers formed are already quite extended. In contrast, at $Q_{initial}$ = 8 where the overlap is much more substantial, the tethered micelle network formed has a larger capacity to swell. However, increased entanglements accompanying this overlap simultaneously serve to counter this swelling, such that Q_{final} values remain smaller than those associated with more dilute systems.

To assess the correlation between mean intermicelle spacing (implied by $Q_{initial}$) and mechanical characteristics of the resultant hydrogels at Q_{final}, each equilibrium swollen sample was subjected to rheological and tensile testing. Dynamic frequency sweeps confirmed a frequency independent elastic modulus in all hydrogels (**Figure 5.4e, inset**) in the series, with the mean value of the elastic moduli taken at ω = 1 rad s^{-1} being negatively correlated with

increasing $Q_{initial}$ (**Figure 5.4e**). That is, the more water per gram polymer in the system at the time of photocoupling ($Q_{initial}$), the lower the modulus of the hydrogel in its final swollen state (Q_{final}). Given the minimal influence of $Q_{initial}$ on the final SOS content (**Figure S5.8**), it appears the decrease in modulus is likely related to the decrease in the bridging-to-looping ratios present in each of these systems as a consequence of the change in micelle spacing.

Finally, preliminary tensile testing revealed a positive correlation between small-strain tensile modulus and $Q_{initial}$ (**Figure 5.4f**). Past 10% strain, hydrogels were likely to slip from the tensile test fixture prior to failure due to their high lubricity and low modulus. Although preliminary, this data confirmed the trend demonstrated by the oscillatory shear experiments discussed above, in that small strain tensile modulus is negatively correlated with $Q_{initial}$. Taken together, these results demonstrate the ability to fine tune the final modulus simply by tailoring the amount of water used to disperse the micelle building blocks.
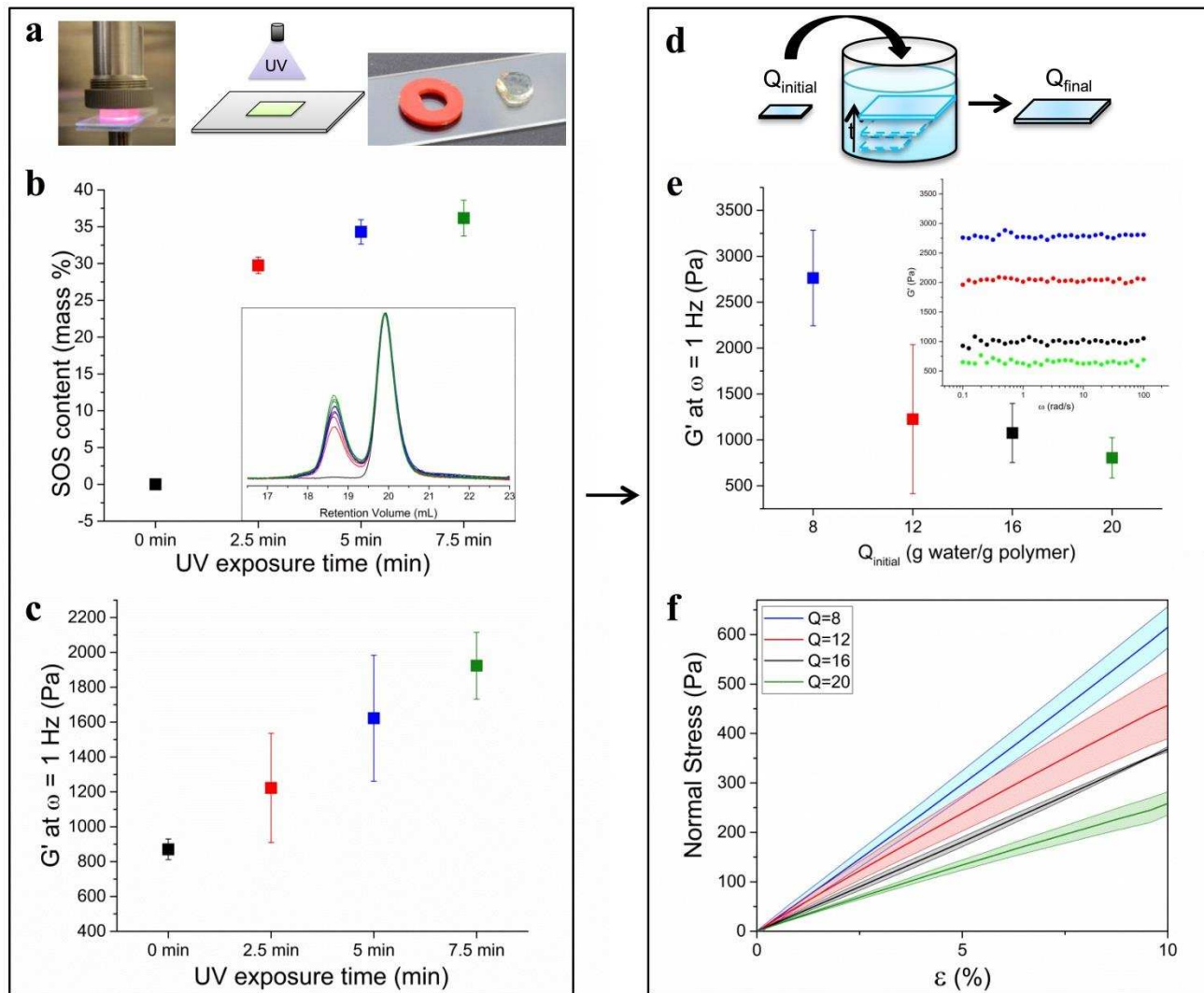
Figure 5.4. (a) $Q_{initial}$ = 16 g water per g polymer solutions were spread into molds and photocoupled using UV light. (b) Installed triblock content based on SEC data was positively correlated with UV exposure time. (c) Shear elastic modulus at room temperature extracted from frequency sweeps (ω = 1 Hz, ε = 7%) was also positively correlated with irradiation time. (d) Samples of photocured hydrogels were then swelled to their equilibrium dimensions in DI water (Q_{final}). (e) Shear elastic modulus (ω = 1 Hz, ε = 7%) and (f) tensile modulus were negatively correlated with $Q_{initial}$ (2 % s^{-1}). Mean and standard deviation shown for all data.

5.3.4 Patterning and Shape Control

The ability of these solutions to rapidly transform from viscous liquids to soft, highly entangled, low-modulus hydrogels make them ideally suited for applications which require high surface area conformal contact, flexibility, and rapid adoption of well-defined macroscopic shapes when molded (**Figure 5.5a-b**). These photographs show the ability of the photocoupled hydrogel to hold a precise edge even after removal from the mold. Network formation through UV irradiation also implies an intrinsic ability for the introduction of shape through photopatterning. In theory, masked regions can be easily removed due to the absence of tethers (network formation) among micelles in those areas. As shown in **Figure 5.5c**, simple letter shapes could be patterned into spread solutions and extracted after rinsing, although edge roughness associated with the scattering of UV light from small gas bubbles is clearly evident. A true assessment of the patterning precision possible in these systems will require removal of bubble inclusions from the solutions prior to UV irradiation. The fluorescence of anthracene and the absence of this fluorescence in the photocycloaddition product allows us to visualize the regions in which photodimerization among SO-anth has occurred to produce the micelle network.[34, 35]

The left side of **Figure 5.5d** depicts powder of SO-OH juxtaposed with powder of SO-anth, showing the strong fluorescence produced even at anthracene concentrations equivalent to one substituent per polymer chain. To the right of this is a self-assembled, pressed disk of SO-anth showing the same fluorescent behavior, followed by an irradiated analogue for which dimerization has been maximized through photocoupling in the melt. A comparison of the two disks shows the clear loss of fluorescence upon significant photodimerization of the SO-anth, such that its appearance is similar to the background luminescence associated the non-anthracene

functional SO-OH powder. In contrast to coupling in the melt, solution photocoupled systems continue to fluoresce (photopatterned star inset) even after extended exposure. This residual fluorescence is thought to be a consequence of unreacted anthracene substituents that have been effectively isolated. Such isolation, we suspect, is a combination of early infinite network formation at very low thresholds of anthracene dimerization (~ 2%), which limits future micelle interactions, in combination with chain anchoring to fixed positions in the micelle core, which limits local chain end mobility. As irradiation proceeds, a fraction of the chain ends become unable to find a dimerization partner in their accessible reaction volume. Other possible sources of limited triblock copolymer formation may derive from non-quantitative functionality present in the initial SO-anth materials, kinetic restrictions on micelle and chain mobility due to high molecular weight entanglements, or the inaccessibility of anthracene-functional chain ends due to being trapped deep within the coronal layer, or even the glassy micelle core itself.
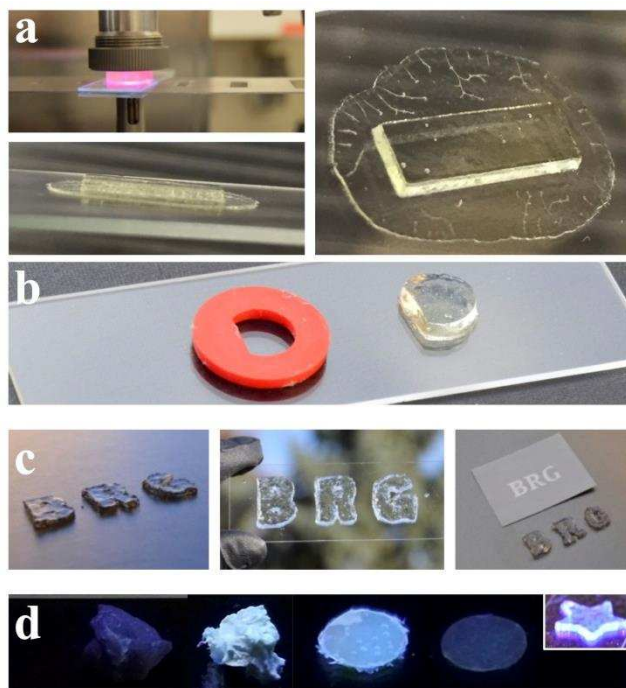
Figure 5.5. (a) Solutions can be molded and irradiated to form distinctly shaped, soft, elastic hydrogels. In the upper panel, $Q_{initial}$ = 20 g water per g polymer was spread into a thin rectangular cutout, previously fixed at the bottom edge to a glass slide. The spread solution was then compacted using a second glass slide, allowing excess material to spread outside the perimeter of the mold's upper face. Extraction from the mold shows the level of conformal integrity achievable by the photocoupled sample throughout the entire depth of the mold. **(b)** Example of a hydrogel formed in a mold (1.73 mm thickness) at $Q_{initial}$ = 20 g water per g polymer, subsequently swollen to Q_{final} following extraction and removal of all peripherally photocoupled (excess) material. **(c)** Shape could also be imposed through photopatterning, using masks to spatially control the introduction of SOS tethers, however with some surface roughness associated with scattering of UV light from small gas bubble inclusions. **(d)** Left to right: SO-OH powder, SO-anth powder, disk of self-assembled SO-anth micelles, and photocoupled SO-anth micelles. Irradiated SO-anth looks akin to SO-OH, consistent with the expected loss of fluorescence upon photocycloaddition to form the dimer. *Inset:* A star-shaped hydrogel

(produced using a star-shaped mask) retains some fluorescence (in contrast to melt photocoupled samples) due to residual orphaned anthracene end groups, present even after longer exposure times.

5.4 Conclusions

Photoreactive block copolymer micelles formed through self-assembly of SO-anth in the melt could be dispersed in water to form spreadable precursor solutions easily transformed into soft, elastic hydrogels with UV irradiation. Rapid preparation of these micellar building blocks was achieved using BCP compositions favoring adoption of the sphere morphology. Micelle structure created during initial phase separation (~ 5 min) was sufficient to produce narrow size distributions and shape uniformity, such that evolution of the morphology to the full BCC structure through extended annealing (> 4 hr) was not required. Micelles were stable in water without evidence of aggregation or degradation over a period of at least nine weeks. Equilibrium swelling (Q_{final}), dynamic elastic modulus, and tensile modulus could be tuned using both UV irradiation time and initial micelle concentration ($Q_{initial}$). UV irradiation time at constant $Q_{initial}$ was positively correlated with SOS concentration, resulting in increased dynamic elastic modulus. Conversely, decreasing $Q_{initial}$ (micelle spacing) under constant irradiation time could also be used to produce higher moduli and limit Q_{final}. Photocoupling in molds could be used to generate custom shapes with excellent conformal integrity and retention of form upon swelling. Preliminary experiments suggest the potential to also introduce shape through photopatterning. Overall, the ability to selectively disperse these micelle building blocks into stable, moldable solutions allows us to produce soft, flexible, conformable hydrogels without the presence of harmful solvents or other leechable small-molecule byproducts. We anticipate these desirable

attributes will have implications in a number of biomedically relevant applications including wound healing, surgical reconstruction, soft tissue repair or replacement, and cosmetics substances.

5.5 Experimental

5.5.1 Materials and Methods

General. Styrene (99%, 50 ppm *p*-tert-butylcatechol inhibitor, Aldrich) was purified by static vacuum (15-30 mTorr) distillations from di-*n*-butylmagnesium (1.0 M in heptane, Aldrich) at 40 °C. Ethylene oxide (99.5+%, compressed gas, Aldrich) was purified by successive distillations from di-*n*-butylmagnesium (1.0 M in heptane, Aldrich) at 3 °C. *sec*-butyllithium (1.3 M in cyclohexane/hexane, Fisher) was used as received. Potassium naphthalenide solution was prepared according to a previous report.[14] 9-(chloromethyl)anthracene (98%, Aldrich) and α,ά-dibromo-*p*-xylene (97%, Aldrich) were dried under high vacuum for several hours prior to use. Tetrahydrofuran (THF) was degassed by sparging with argon (10 psi) for a period of 45 minutes and then purified over two molecular sieve columns of neutral alumina (Glass Contour, Inc.). Cyclohexane (CHX) was degassed with argon and purified through a column of neutral alumina followed by a column of Q5 copper (II) oxide catalyst (Glass Contour, Inc.). Hydrogels were swollen using DI water of 18.2 MΩ resistivity (Evoqua/U.S. Filter Service Deionization). Other common chemicals and solvents were used as received unless otherwise stated. Ultra-high purity argon (99.998% Airgas) was passed through a column of 5 Å molecular sieves with Drierite (Agilent) and oxygen absorbing purifier column (Matheson Tri-gas). Glassware and polymerization reactors were flamed under vacuum and backfilled with argon (3 X).

Synthesis of PS–PEO (SO) and PS-PEO-anthracene (SO-anth). Hydroxyl terminal polystyrene–*b*–poly(ethylene oxide) (PS–PEO, SO) was synthesized according to a previously reported procedure[14] using two-step anionic polymerization of styrene and ethylene oxide monomer. In brief, step one involved the synthesis of a hydroxyl-terminal polystyrene macroinitiator ($M_{n,PS}$ = 8064 g mol^{-1}, $M_{w,PS}/M_{n,PS}$ = 1.05, SEC (polystyrene standards)), from which the final SO-OH diblock copolymer was produced. The volume fraction of the PS block in the final diblock copolymer was determined to be 0.122 (using nominal densities at 140 °C)[36] with an overall M_n = 73800 g mol^{-1} ($M_{w,SO}/M_{n,SO}$ = 1.04. SEC (polystyrene standards)) calculated using the measured $M_{n,PS}$ and the relative ^{1}H NMR integrations.

SO was then dissolved in dry THF. The solution was slowly titrated with potassium naphthalenide such that the solution remained light green for at least 20 min. A large excess of 9-(chloromethyl)anthracene (~10-30 x) was then immediately added to the PS–PEO alkoxide solution under a slight positive pressure of argon at room temperature. The solution was allowed to stir overnight under argon. The anthracene terminated block copolymer product was precipitated from 25 °C pentane twice. The material was then filtered and partially dried, then then re-dissolved in THF with 0.5 weight percent butylated hydroxyl toluene (BHT) added to act as a radical scavenger. The polymer was then dried in vacuo (25 °C, ~24 h) with the resulting block copolymer appearing as a yellow-tinged white powder. Yield varied between 85-90%. SEC (polystyrene standards): M_w/M_n = 1.04. ^{1}H NMR (400 MHz, CDCl$_3$, δ): 8.4–8.5 (m, anthracene H_1, H_8 and H_{10}), 7.9–8.0 (d, anthracene H_4 and H_5), 7.4–7.6 (m, anthracene H_2, H_3, H_6 and H_7), 6.2–7.2 (b, –CH_2–C(R)H–C$_6$$H_5$), 5.5 (s, –O–C$H_2$–anthracene), 3.4–3.8 (b, –CH_2–CH_2–O–), 1.1–2.3 (b, –CH_2–C(R)H–C$_6$H$_5$), 0.8–0.9 (b, CH$_3$–CH_2–C(R)H–CH$_3$), 0.5–0.7 (b, CH_3–CH$_2$–C(R)H–CH_3) See **Figure S5.1** for clarification of anthracene proton assignments, which are

consistent with a previous report.[37] Relative integrations of anthracene to initiator protons suggest a quantitative addition within ^{1}H NMR integration error (~5%).

Synthesis of micelle solutions. SO-anth was pressed between Teflon sheets at 120 °C for 5 min, using a mold to prevent spreading of the material during compression. For annealing studies, this pressed material was then further annealed at 120 °C in either nitrogen (using the rheometer) or in vacuum (in the SAXS) for a range of times. Solutions of SO-anth polymer were pressed without annealing, and combined in specific quantities with degassed DI water. These solutions are used throughout the study in varying concentrations depending on the application, and the relative amounts of water and polymer used are quantified by the value Q (g water per g polymer) which range from $Q = 8$ to 1000. Containing vials of just-made solutions are topped off with argon gas and left to sit for 24-72 h (depending on their Q) to allow the polymer to soften and mix with the water, and subsequently vortexed for 10 seconds and allowed to settle. Solutions were used as soon as they appeared well-mixed with no visible solid suspensions. Solutions of equal concentration were subjected to identical dissolution procedure times for consistency between solution batches.

Hydrogel Formation. Molds were temporarily adhered to a hydrophobic glass slide using double-sided tape. Sample solutions were then scooped into molds using a spatula, and then sandwiched using a second treated glass slide also adhered with the tape to prevent movement of the setup during irradiation and when turning over halfway through irradiation time. UV curing took place using an OmniCure Series 2000 UV curing system with a 200-Watt mercury arc lamp, in conjunction with an Asahi Spectra Co high transmission band pass 365 nm filter. The intensity at the surface of the sample was 28–32 mW cm^{-2} (measured in the range of 200–600 nm with an

117

Omnicure R2000 Radiometer). Samples were exposed to UV 365 nm filtered light for 2.5 – 7.5 minutes and flipped over halfway through the exposure time.

5.5.2 Measurements

NMR and GPC. ^{1}H NMR spectra were recorded at room temperature on a Varian Inova 400 MHz spectrometer with a d1 pulse delay of at least 20 s to ensure complete relaxation of end-groups. Spectra were referenced to $CDCl_3$ solvent. Size exclusion chromatography (SEC) spectra were collected on a Viscotek GPC-Max chromatography system outfitted with three 7.5 x 340 mm Polypore™ (Polymer Laboratories) columns in series, a Viscotek differential refractive index (RI) detector, and an Alltech column oven (mobile phase DMF, 40 °C, 1 mL min^{-1}).

SAXS. Small Angle X-ray Scattering (SAXS) data were collected on a Rigaku S-Max 3000 High Brilliance three pinhole SAXS system outfitted with a MicroMax-007HFM rotating anode (CuKα), Confocal Max-Flux™ Optic, Gabriel multiwire area detector, and a Linkam thermal stage. Dry polymer samples were sandwiched between Kapton windows (0.05 – 0.5 mm thick X 10 mm diameter). Scan times were typically on the order of 3600 s, with temperature ramp rates of 10 °C min^{-1}

Rheology. Rheological melt experiments were run on a TA Instruments Advanced Rheometric Expansion System (ARES) rheometer. Dynamic temperature ramp tests were performed on dry polymer disks while heating and cooling at 1 °C min^{-1} at angular frequency of 1 rad s^{-1} and a strain of 7 % (within the linear viscoelastic regime, determined by dynamic strain sweep experiments for each sample). Rheological frequency sweeps (ω = 0.1 – 100 rad s^{-1}, ε = 7%, $\dot{\varepsilon}$ = 2% s^{-1}) performed on micelle solutions and swollen hydrogels were run at room temperature using a lower tool "cup bath" base and an 8 mm stainless steel upper parallel plate. Non-photocoupled solutions were placed in a small mass upon the center of the base, and

photocoupled and swollen hydrogels were blotted and placed in the center of the base. For both samples, a constant force of approximately 5-10% compression was applied before any testing in order to ensure sufficient contact and prevent slip. Tensile tests were performed on rectangular hydrogel samples at room temperature using the normal force transducer of a TA ARES rheometer. TA rectangular torsion geometry test fixtures modified with sandpaper were used as tensile test grips, and a strain rate of 2 % s^{-1} was applied until slip or fracture. Engineering stress was calculated using sample cross-sectional area-normalized force.

Cryo-TEM. Samples were vitrified using a computer controlled vitrification robot (FEI Vitrobot^{TM} Mark III, FEI Company). Lacey carbon films on 200 mesh copper grids (LC200-CU, Electron Microscopy Sciences) were surface plasma treated with a Cressington 208 carbon coater. Vitrified films were transferred into the vacuum of a Tecnai Sphera microscope with a Gatan 626 cryoholder. The microscope is equipped with an LaB$_6$ filament that was operated at 200 kV, and a bottom mounted 1024x1024 Gatan charged-coupled device (CCD) camera. SO-anth and SO-OH obtained after quenching melt blends from 70 °C were dispersed in DI water at concentrations of 1 mg/mL and 2 mg/mL, respectively. The Vitrobot was operated at 22 °C and at a relative humidity of 100%. In the preparation chamber of the 'Vitrobot', a 3μl sample was applied on a Lacey carbon film which was surface plasma treated for 40 s at 5 mA just prior to use. Excess sample was removed by blotting using two filter papers for 3 s at –3 mm, and the thin film thus formed was plunged (acceleration about 3 g) into liquid ethane just above its freezing point. The vitrified films were observed in the Tecnai Sphera microscope at temperatures below -170 °C. Micrographs were taken at low dose conditions, at a magnification of 25000 and at -5 μm defocus.

Determination of changes in Q. Solutions of particular water to polymer ratio $Q_{initial}$ were photocoupled in rectangular mold to attain solid-like hydrogel properties. They were then swollen to equilibrium in DI water, achieving a new water to polymer ratio of Q_{final}. These two swollen states are compared in the manuscript. To determine $Q_{final,}$ measurements of initial and final dimensions were found using a caliper to then calculate the corresponding volumes. In this way, the increase in volume is attributed to water imbibed after photocuring and placement in water as opposed to gravimetric measurements which do not take into account air bubbles in the dry polymer. Summing this increase in mass with the mass of water initially in the solution, a Q_{final} can be determined.

DLS. Dynamic light scattering measurements were performed using a ZEN3600 Zetasizer Nano particle analyzer. Measurements were taken on the solutions diluted to Q=1000 g water per g polymer, and performed at 25 °C, 173° detector angle, and a 4mW 633 nm laser. All reported particle sizes and PDIs are based on the Z-averaged diameter determined by Zetasizer DLS measurement software.

5.6 Supporting Information

5.6.1. ^{1}H-NMR spectrum and GPC traces of SO-anth and precursors.
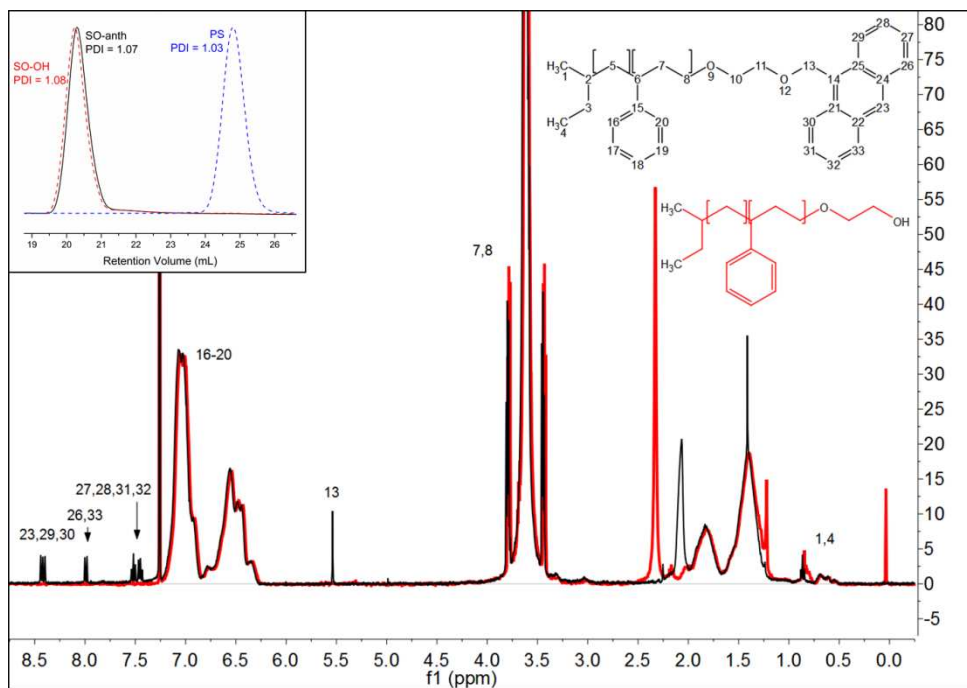
Figure S5.1. Overlaid SO-OH and SO-anth ^{1}H-NMR (with peak assignments) and SEC traces (inset) showing nearly identical molecular weight distributions.

5.6.2. Comparison of SO-anth and SO-OH melt-state self-assembly data
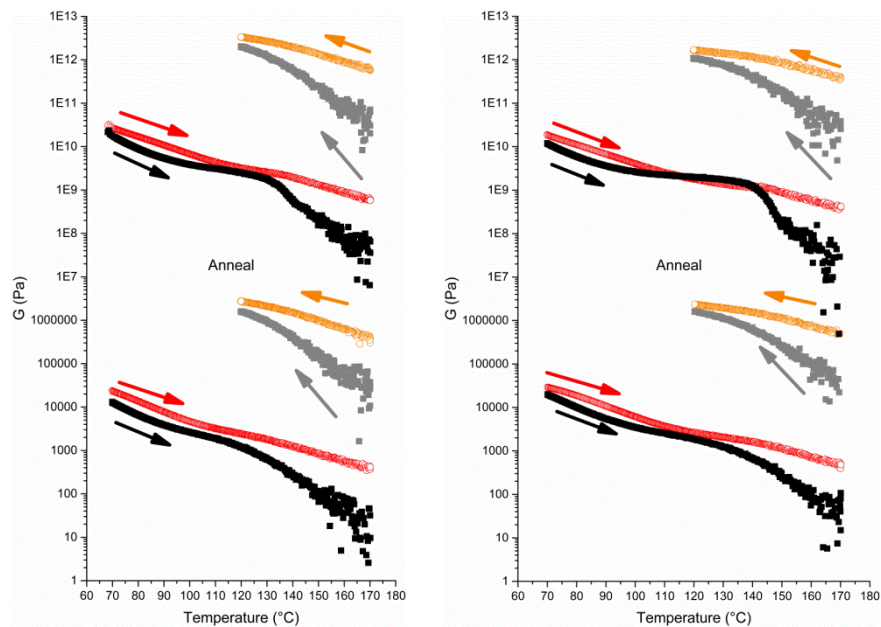
Figure S5.2. A series of consecutive rheological temperature ramp measurements (1 °C min^{-1}, ϵ = 1 %, ω = 1 Hz) performed on SO-anth (left) and SO-OH (right). Experiments were performed as follows (plotted from low to high): Samples were initially heated from 70 °C to 170 °C, cooled to 120 °C, annealed in situ for 4 hours and slowly cooled to 70 °C (not shown), heated through a second cycle from 70 °C to 170 °C, and then cooled back to 120 °C once more. The experiments demonstrate that both SO-OH and SO-anth samples gain an increase in modulus from annealing, associated with organization of the BCC lattice of micelles over time. However, heating past the transition (inflection in G') that is produced post-annealing around 140 °C results in complete loss of the higher order state gained during annealing. We believe this transition reflects a disordering transition from BCC to LLP of micelles. Solid circles indicate storage moduli data (G') and open circles are loss moduli data (G'').
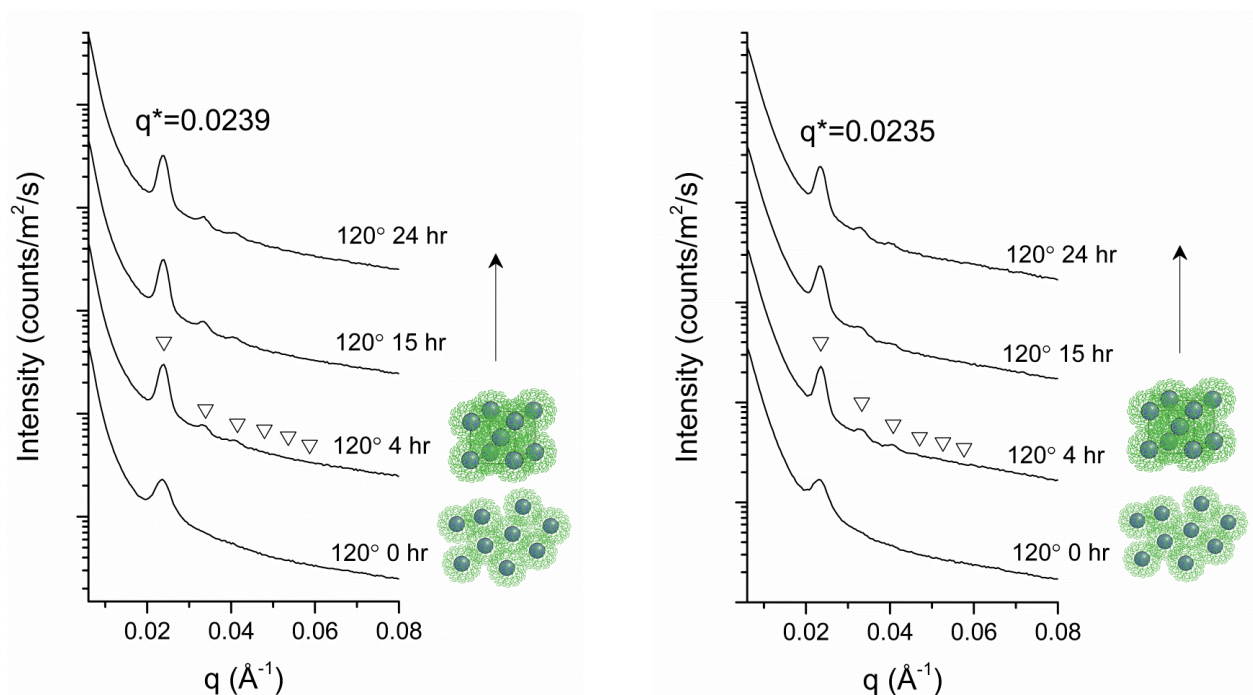
Figure S5.3. SAXS annealing (120 °C) of SO-anth (left) and SO-OH (right), showing adoption of a BCC lattice in the sphere morphology of micelles beginning at four hours.

Table S5.1. Micelle structural characterization information based on SAXS data.

Sample	f_{PS} [a]	$q^*/Å^{-1}$ [b]	d_{110}/nm [c]	a_{BCC}/nm [d]	R^a/nm [e]	θ_{PS} [f]	$M_n/10^6$ g mol^{-1} [g]
SO-Anth (nh3-19)	0.122	0.0239	26.3	37.2	9.0	221	16.3
SO-OH (nh2-207)	0.125	0.0235	26.7	37.8	9.2	232	17.1

[a]Polystrene volume fraction, [b]primary scattering peak, [c]d-spacing for 110 crystal plane, [d]unit cell lattice constant [e]apparent radius, [f]mean aggregation number (i.e., PS chains per sphere), [g]estimated molecular weight of micelle.
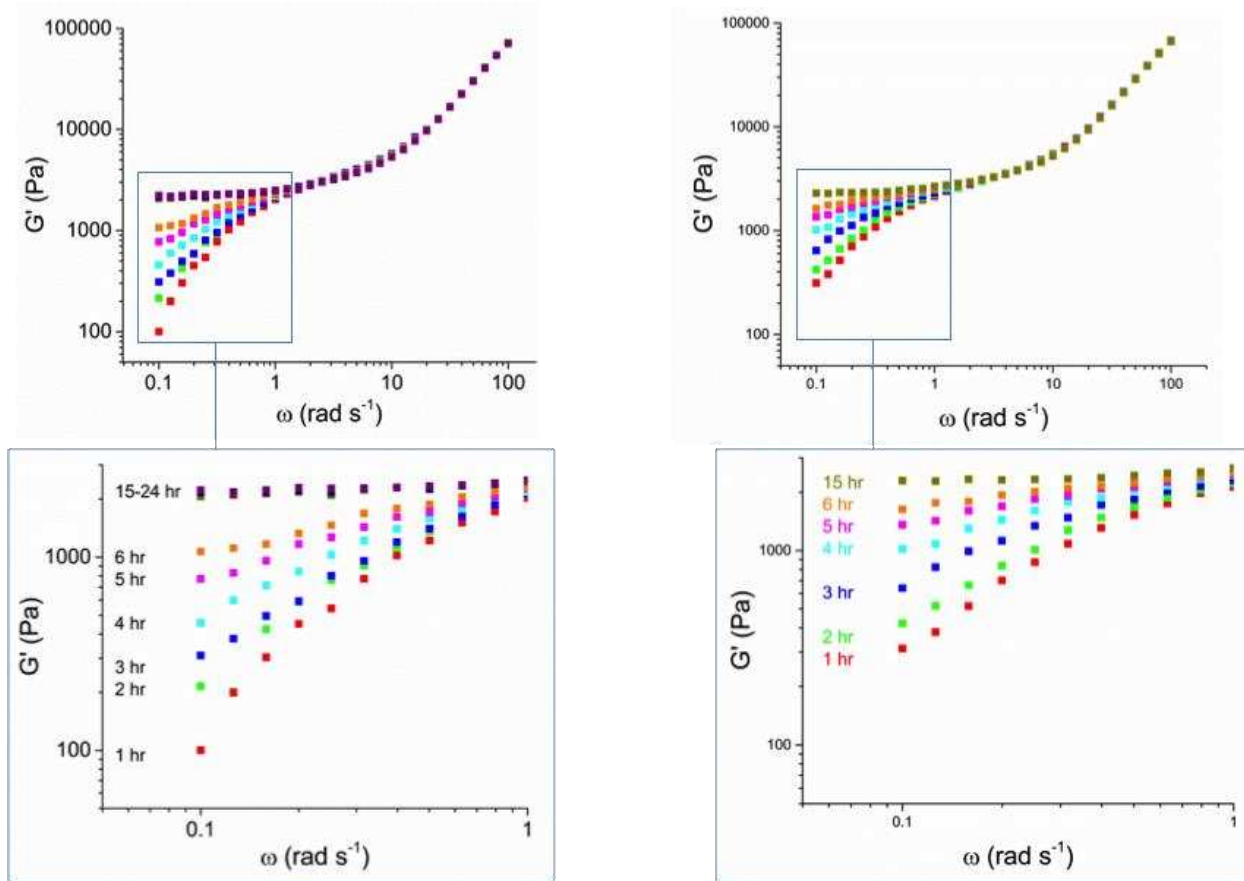
Figure S5.4. Rheological frequency sweeps under oscillatory shear at 120 °C (ω = 1 rad s^{-1}, ε = 7%) for both SO-anth (left) and SO-OH (right), with log G' plotted vs. log ω. Data shows the progression from liquid-like terminal relaxation behavior at a slope of ~2 to a highly ordered BCC lattice with a frequency independent plateau (0 slope) over the course of 15 hours.
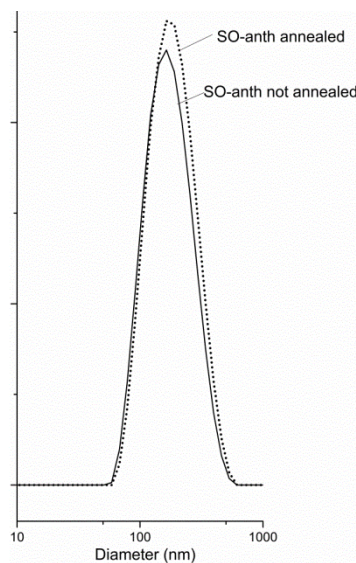
Figure S5.5: Comparison of hydrated SO-anth micelles produced with four hours annealing (BCC) versus those produced without annealing (5 minute melt press only).

5.6.3. Examination of SO-anth and SO-OH building block architecture in solution
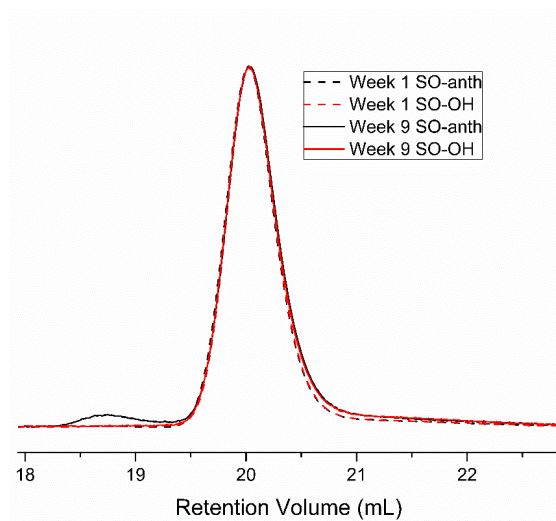
Figure S5.6. Overlaid GPC traces of SO-anth and SO-OH polymer species taken from micelles persisting in solutions for one and nine weeks. Traces show no change in molecular weight distribution over time save a small amount of SO-anth photocoupling to form SOS in the 9-week old SO anth micelles.
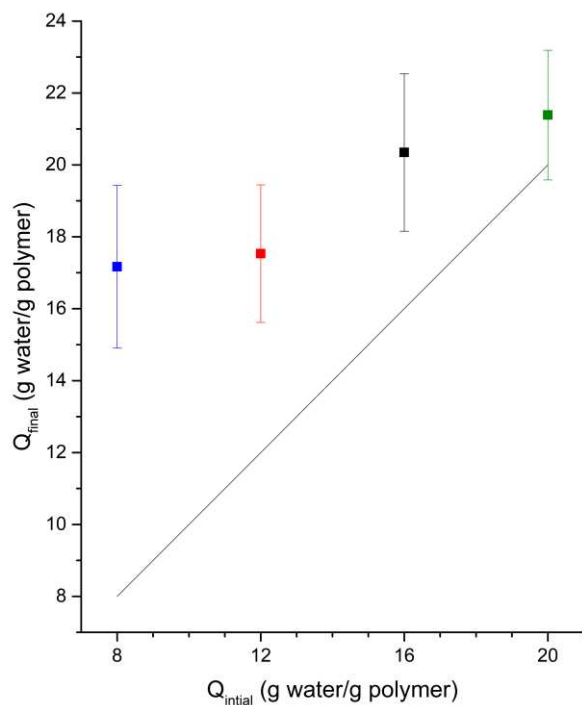
Figure S5.7. Solutions of $Q_{initial}$ = 8, 12, 16, and 20 g water per g polymer were irradiated for 5 min and swelled to their equilibrium state at Q_{final}. Values of Q_{final} were only moderately positively correlated with $Q_{initial}$ solution concentrations, each solution appearing to approach a mean final value between 18 and 21, with ΔQ diminishing with increasing $Q_{initial}$ (minimal additional swelling occurring after photocoupling at $Q_{initial}$ = 20). The line for no swelling is shown for reference.
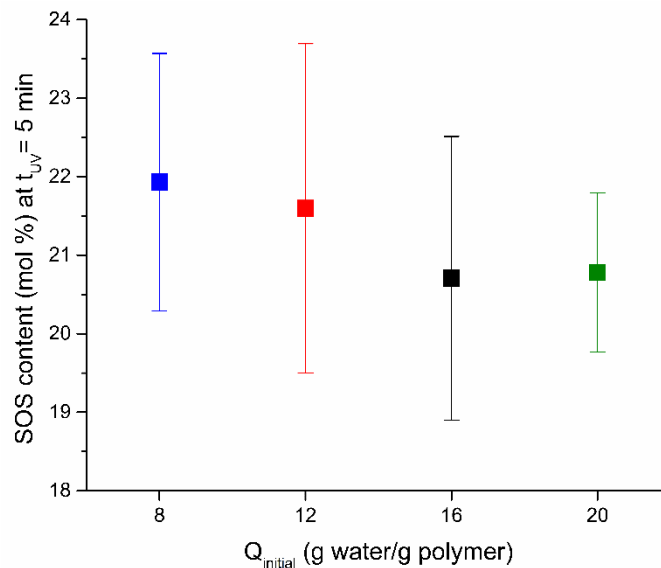
Figure S5.8. SOS triblock copolymer content (mol%, mean with a standard deviation of error shown) had a small, negative correlation with $Q_{initial}$, showing minimal influence of solution concentration on degree of tethering achievable after 5 min of UV irradiation.

5.6.4. Number of Trials per Experiment

Table S5.2.

# Trials	$Q_{initial}$				t_{UV}			
	8	12	16	20	0	2.5	5	7.5
G'	8	9	7	8	2	3	3	3
SOS	4	4	4	3	3	3	3	3
Q (SI)	7	7	7	8				
Tensile	2	3	2	2				

127

5.6.5. Sample Identification History

Table S5.3.

Manuscript ID	Lab Notebook ID
S-OH	DBW1142
SO-OH	NH2207
SO-anth	NH3012/NH3019/NH4053

References

1.   Annaka, M.; Matsuura, T.; Kasai, M.; Nakahira, T.; Hara, Y.; Okano, T. Preparation of Comb-Type N-Isopropylacrylamide Hydrogel Beads and Their Application for Size-Selective Separation Media. *Biomacromolecules* **2003,** 4, (2), 395-403.

2.   Susanto, H.; Ulbricht, M. Photografted Thin Polymer Hydrogel Layers on PES Ultrafiltration Membranes:‚Äâ Characterization, Stability, and Influence on Separation Performance. *Langmuir* **2007,** 23, (14), 7818-7830.

3.   Peppas, N. A.; Bures, P.; Leobandung, W.; Ichikawa, H. Hydrogels in pharmaceutical formulations. *Eur J Pharm Biopharm* **2000,** 50, (1), 27-46.

4.   Gong, C.; Shi, S.; Wang, X.; Wang, Y.; Fu, S.; Dong, P.; Chen, L.; Zhao, X.; Wei, Y.; Qian, Z. Novel Composite Drug Delivery System for Honokiol Delivery: Self-Assembled Poly(ethylene glycol)–Poly(ε-caprolactone)–Poly(ethylene glycol) Micelles in Thermosensitive Poly(ethylene glycol)–Poly(ε-caprolactone)–Poly(ethylene glycol) Hydrogel. *J. Phys. Chem. B* **2009,** 113, (30), 10183-10188.

5.   Dai, H.; Chen, Q.; Qin, H.; Guan, Y.; Shen, D.; Hua, Y.; Tang, Y.; Xu, J. A Temperature-Responsive Copolymer Hydrogel in Controlled Drug Delivery. *Macromolecules* **2006,** 39, (19), 6584-6589.

6.   Madaghiele, M.; Demitri, C.; Sannino, A.; Ambrosio, L. Polymeric hydrogels for burn wound care: Advanced skin wound dressings and regenerative templates. *Burns & trauma* **2014,** 2, (4), 153-61.

7.   Desai, P. N.; Yuan, Q.; Yang, H. Synthesis and Characterization of Photocurable Polyamidoamine Dendrimer Hydrogels as a Versatile Platform for Tissue Engineering and Drug Delivery. *Biomacromolecules* **2010,** 11, (3), 666-673.

8.   Hou, Y.; Schoener, C. A.; Regan, K. R.; Munoz-Pinto, D.; Hahn, M. S.; Grunlan, M. A. Photo-Cross-Linked PDMSstar-PEG Hydrogels: Synthesis, Characterization, and Potential Application for Tissue Engineering Scaffolds. *Biomacromolecules* **2010,** 11, (3), 648-656.

9.   Stile, R. A.; Burghardt, W. R.; Healy, K. E. Synthesis and Characterization of Injectable Poly(N-isopropylacrylamide)-Based Hydrogels That Support Tissue Formation in Vitro. *Macromolecules* **1999,** 32, (22), 7370-7379.

10.	Moller, S.; Weisser, J.; Bischoff, S.; Schnabelrauch, M. Dextran and hyaluronan methacrylate based hydrogels as matrices for soft tissue reconstruction. *Biomol. Eng* **2007,** 24, (5), 496-504.

11.	Ho, E.; Lowman, A.; Marcolongo, M. Synthesis and characterization of an injectable hydrogel with tunable mechanical properties for soft tissue repair. *Biomacromolecules* **2006,** 7, (11), 3223-3228.

12.	Sannino, A.; Demitri, C.; Madaghiele, M. Biodegradable Cellulose-based Hydrogels: Design and Applications. *Materials* **2009,** 2, (2), 353-373.

13.	Parente, M. E.; Andrade, A. O.; Ares, G.; Russo, F.; Jimenez-Kairuz, A. Bioadhesive hydrogels for cosmetic applications. *Int J Cosmetic Sci* **2015,** 37, (5), 511-518.

14.	Guo, C.; Bailey, T. S. Highly distensible nanostructured elastic hydrogels from AB diblock and ABA triblock copolymer melt blends. *Soft Matter* **2010,** 6, (19), 4807-4818.

15.	Guo, C.; Bailey, T. S. Tailoring mechanical response through coronal layer overlap in tethered micelle hydrogel networks. *Soft Matter* **2015,** 11, (37), 7345-7355.

16.	Guo, C.; Lewis, J. T.; Scalfani, V. F.; Schwartz, M. M.; Bailey, T. S. Dangling-End Double Networks: Tapping Hidden Toughness in Highly Swollen Thermoplastic Elastomer Hydrogels. *Chem. Mater.* **2016,** 28, (6), 1678-1690.

17.	Huq, N. A.; Ekblad, J. R.; Leonard, A. T.; Scalfani, V. F.; Bailey, T. S. Phototunable Thermoplastic Elastomer Hydrogel Networks. *Macromolecules* **2017,** 50, (4), 1331 - 1341.

18.	Bates, F. S.; Fredrickson, G. H. Block Copolymers: Designer Soft Materials. *Phys.Today* **1999,** 52, 32-38.

19.	Bates, F. S. Polymer-Polymer Phase Behavior. *Science* **1991,** 251, (4996), 898-905.

20.	Bates, F. S.; Schulz, M. F.; Khandpur, A. K.; Forster, S.; Rosedale, J. H.; Almdal, K.; Mortensen, K. Fluctuations, Conformational Asymmetry and Block-Copolymer Phase-Behavior. *Faraday Discuss.* **1994,** 98, 7-18.

21.	Cavicchi, K. A.; Lodge, T. P. Domain size equilibration in sphere-forming block copolymers. *J Polym Sci Pol Phys* **2003,** 41, (7), 715-724.

22.	Scalfani, V. F. Part I — Access to UV Photocured Nanostructures via Selective Morphological Trapping of Block Copolymer Melts. Part II — Morphological Phase Behavior of Poly(RTIL) Containing Block Copolymer Melts. Ph.D. Dissertation, Colorado State University, Fort Collins, Colorado, 2012.

23.   Scalfani, V. F.; Bailey, T. S. Access to Nanostructured Hydrogel Networks through Photocured Body-Centered Cubic Block Copolymer Melts. *Macromolecules* **2011,** 44, (16), 6557-6567.

24.   Scalfani, V. F.; Wiesenauer, E. F.; Ekblad, J. R.; Edwards, J. P.; Gin, D. L.; Bailey, T. S. Morphological Phase Behavior of Poly(RTIL)-Containing Diblock Copolymer Melts. *Macromolecules* **2012,** 45, (10), 4262-4276.

25.   Shi, Z. X.; May, A. W.; Kohno, Y.; Bailey, T. S.; Gin, D. L. Metal-Containing Ionic Liquid-Based, Uncharged-Charged Diblock Copolymers that Form Ordered, Phase-Separated Microstructures and Reversibly Coordinate Small Protic Molecules. *J Polym Sci Pol Chem* **2017,** 55, (18), 2961-2965.

26.   Shi, Z. X.; Newell, B. S.; Bailey, T. S.; Gin, D. L. Ordered, microphase-separated, noncharged-charged diblock copolymers via the sequential ATRP of styrene and styrenic imidazolium monomers. *Polymer* **2014,** 55, (26), 6664-6671.

27.   Shi, Z.; Newell, B. S.; Bailey, T. S.; Gin, D. L. Ordered, Microphase-Separated, Noncharged-Charged Diblock Copolymers via the Sequential ATRP of Styrene and Styrenic Imidazolium Monomers. *Polymer* **2014,** 55, (26), 6664-6671.

28.   Bailey, T. S. Morphological behavior spanning the symmetric AB and ABC block copolymer states. Ph.D. Dissertation, University of Minnesota, Minneapolis, Minnesota, 2001.

29.   Kossuth, M. B.; Morse, D. C.; Bates, F. S. Viscoelastic behavior of cubic phases in block copolymer melts. *J. Rheol.* **1999,** 43, (1), 167-196.

30.   Wijayasekara, D. B.; Cowan, M. G.; Lewis, J. T.; Gin, D. L.; Noble, R. D.; Bailey, T. S. Elastic free-standing RTIL composite membranes for CO2/N2 separation based on sphere-forming triblock/diblock copolymer blends. *Journal of Membrane Science* **2016,** 511, 170-179.

31.   Jain, S.; Bates, F. S. Consequences of nonergodicity in aqueous binary PEO-PB micellar dispersions. *Macromolecules* **2004,** 37, (4), 1511-1523.

32.   Scalfani, V. F.; Bailey, T. S. Thermally Stable Photocuring Chemistry for Selective Morphological Trapping in Block Copolymer Melt Systems. *Chem. Mater.* **2010,** 22, (21), 5992-6000.

33.   Egbe, D. A. M.; Turk, S.; Rathgeber, S.; Kuhnlenz, F.; Jadhav, R.; Wild, A.; Birckner, E.; Adam, G.; Pivrikas, A.; Cimrova, V.; Knor, G.; Sariciftci, N. S.; Hoppe, H. Anthracene Based Conjugated Polymers: Correlation between pi-pi-Stacking Ability, Photophysical Properties, Charge Carrier Mobility, and Photovoltaic Performance. *Macromolecules* **2010,** 43, (3), 1261-1269.

34.   Schwarz, F. P.; Wasik, S. P. Fluorescence Measurements of Benzene, Naphthalene, Anthracene, Pyrene, Fluoranthene, and Benzo[E]Pyrene in Water. *Anal. Chem.* **1976,** 48, (3), 524-528.

35.   Byron, C. M.; Werner, T. C. Experiments in Synchronous Fluorescence Spectroscopy for the Undergraduate Instrumental Chemistry Course. *J. Chem. Educ.* **1991,** 68, (5), 433-436.

36.   Fetters, L. J.; Lohse, D. J.; Richter, D.; Witten, T. A.; Zirkel, A. Connection between Polymer Molecular Weight, Density, Chain Dimensions, and Melt Viscoelastic Properties. *Macromolecules* **1994,** 27, (17), 4639-47.

37.   Coursan, M.; Desvergne, J. P.; Deffieux, A. Reversible photodimerisation of ω-anthrylpolystyrenes. *Macromol. Chem. Phys.* **1996,** 197, (5), 1599-1608.

Chapter 6.

Spatial control of mechanical properties and surface topography in a photoreactive block copolymer hydrogel

6.1 Summary

A simple method for spatially directed mechanical reinforcement and surface feature implementation on a photoactive BCP-based TPE hydrogel is presented here. The hydrogel material comprises two primary spherical micelle-forming block copolymer species, photoactive ω-anthracenylpolystyrene-*b*-poly(ethylene oxide) diblock copolymer (SO-anth) and polystyrene-*b*-poly(ethylene oxide)-*b*-polystyrene triblock copolymer (SOS). The PEO midblock of the SOS triblock copolymer species provides a physical tether between adjacent micelles, increasing mechanical robustness (modulus) with addition of bridging SOS chains. The photoactive SO-anth diblock copolymer contains terminal anthracene unit capable of dimerization by application of 365 nm light to induce a [4+4] photocycloaddition. The ability to photocouple chain termini populating the outer shell of the hydrophilic micelle coronas produces additional SOS triblock copolymer *in situ*. While the initial population of SOS tethers act to form a primary network in the system, photoinstallation can be used to introduce a secondary network after swelling. This work reports the impact of UV exposure on a hydrogel comprising a base amount (24 or 17 mol %) of SOS triblock copolymer (serving as a primary tethering network), with the balance SO diblock copolymer predominantly terminated with anthracene. Following melt-state self-assembly and subsequent swelling to its equilibrium dimensions, photoinstallation of a secondary

SOS network (up to a 6 mol % increase in SOS) resulted in a two- to five-fold increase in toughness (from 86 to 224 and 35 to 168 kJ/m^3 for SOS-24 and SOS-17, respectively). This ability to photoinstall tethers *in situ* also presented a straightforward means to reinforce particular regions of a hydrogel, exploited here by incorporating photopatterned mechanical anisotropy. In addition, photopatterning tether density led to the formation of surface topography, a side effect of intrinsically restricting swelling in irradiated regions of the hydrogel.

6.2 Introduction

Of the many diverse application areas proposed for hydrogel materials, there are a range of such applications which require spatially directed and designed periodicity, such as in tissue engineering and cellular environments,[1-5] load bearing biomedical components,[6-8] drug delivery matrices,[9] and microchips.[10, 11] One way to achieve such periodicity is by patterning the hydrogels as needed for the application. Such hydrogel patterning usually requires 3D printing[11] or a range of lithographic techniques[4, 12] which require complex preparation and execution and often suffer in resolution. Additionally, such patterning is usually employed for building structures rather than achieving spatio-mechanical tunability, which can be highly advantageous in load-bearing applications. One prominent example is in the design of soft tissue mimics, for which spatial anisotropy in mechanical properties is necessary to match the combined compressive and tensile properties of the target tissue.[13, 14]

Other photopatterning and photolithography strategies have demonstrated an ability to set injectable hydrogel precursors into desired features using a photomask.[15] Eijkel et al.[11] reports a process to create precisely formed hydrogel microarrays in closed microchips using optical lithography and photopolymerizable hydrogels precursor solutions. Despite the utility of photopatterning for this particular application due to the ability to set small feature sizes and

benefit from the high mass transport of the photopolymerized hydrogels, this particular photopatterning technique has not been shown permit a large range of mechanical properties or ease of tunability in this context. This is because the stiffness of the hydrogel produced from irradiation of a monomeric precursor is mainly dependent on monomer concentration, which limits its mechanical variability and does not necessarily allow for incorporation or adjustment of elasticity and other mechanical properties.

Block copolymers, given their inherent ability to organize into regular nanoscale structures and access to tunable mechanical properties, have been attractive options for use in fabrication of hydrogels for electronic storage media[16] and integrated surface design applications using masked photolithography.[10] Previous work using BCPs demonstrates mechanical tunability in the areas of stiffness and toughness, but accomplishes such tunability by incorporation and cellulose fiber for reinforcement.[17] This report details an alternative hydrogel design which also provides access to a wide range of mechanical properties using irradiation and potential for photomasking, but without requiring complex fabrication or addition of non-BCP components.

This hydrogel design was developed from a foundational class of swollen hydrogels developed previously by our group, produced from sphere-forming BCP thermoplastics.[18] These hydrogels are highly elastic and retain the macroscopic shape imposed during melt-state self-assembly and processing.[19-22] The BCP thermoplastics consist of AB diblock and ABA triblock copolymer blends, the A and B blocks of which are selected such that the vitrified core (A blocks) of the spherical aggregate is intrinsically hydrophobic, while the corona (B blocks) is hydrophilic. Incorporation of the ABA triblock copolymer species serves to tether adjacent spherical micelles due to the shared B midblock, allowing for the use of ABA triblock copolymer concentration (number of tethers per sphere) as a means of controlling hydrogel mechanical properties and

swelling behavior. Initial investigations based on these concepts utilized blends of polystyrene-*b*-poly(ethylene oxide) diblock and polystyrene-*b*-poly(ethylene oxide)-*b*-polystyrene (SO-OH/SOS) triblock copolymers, resulting in hydrogels which exhibited not only shape preservation but exceptional elasticity, with elastic moduli tunable through SOS triblock copolymer concentration which could be established through blending prior to self-assembly.

The terminal hydroxyl functionality of the SO-OH diblock copolymer species can be used as a straightforward means of incorporating functionality onto these micelles. In a previous report, our group demonstrated the ability to customize these micelles' dangling hydroxyl chain ends with clickable azide and alkyne functionality. This functionalization allowed for dangling chain ends within the swollen hydrogel matrix to be actively coupled through the introduction of a copper catalyst. This coupling effectively installed a second, interpenetrating network of SOS tethers within the primary, pre-blended population of tethers present during melt-state assembly.[21] We recently also used the same terminal hydroxyl functionality to introduce anthracene substituents to the chain ends, such that photo-induced anthracene dimerization could be used to generate SOS triblock copolymer through light-induced chain coupling. In this case, we used self-assembly of the anthracene functionalized BCP to produce micelle systems in which adjustment of mechanical properties and swelling behavior of the hydrogels through SOS concentration could be achieved simply by controlling UV irradiation time (total intensity).[22, 23] This strategy was based around the ability of UV light at around 365 nm to induce [4 + 4]cycloaddition between anthracene groups,[24] thus forming a symmetric SOS triblock copolymer *in situ*. Thus tethering of spherical domains could be achieved without having to preblend the SOS triblock copolymer population prior to melt processing. This strategy resulted in simplified bulk formation of TPE hydrogel networks both in the melt and in solution, reaching a wide range

of moduli, swelling behaviors, and potential applications due to the modularity and versatility of this simple construct.

However, we had yet to exploit the latent potential to generate unique network properties afforded by combining direct addition of SOS prior to melt-assembly with post-swelling installation of additional SOS using UV light, or the intrinsic ability to spatially control tether density through photopatterning. The latter, if successful, would present an opportunity to dictate both mechanical properties and swelling behavior in chosen regions of the hydrogel. In this chapter, we explore this latent potential. All experiments were performed on a blend of anthracene and hydroxyl functional diblock copolymer (SO-anth and SO-OH), with a base amount of preblended SOS triblock copolymer (**Figure 6.1**). First, we examined the mechanical and swelling effects of a photoinstalled secondary network on two base SOS blend compositions, carrying out the installation of the second tether population both in the melt and in the swollen equilibrium state. Next, we used the results of this initial study examine the effects of tether concentration anisotropy on the tensile performance of the hydrogels, with tensile stresses applied either parallel to or perpendicular to photopatterned striations of tether concentration installed in the swollen state. Finally, we examined the utility of photopatterning in the melt state to impose surface topography which could autonomously present at the surface upon swelling.
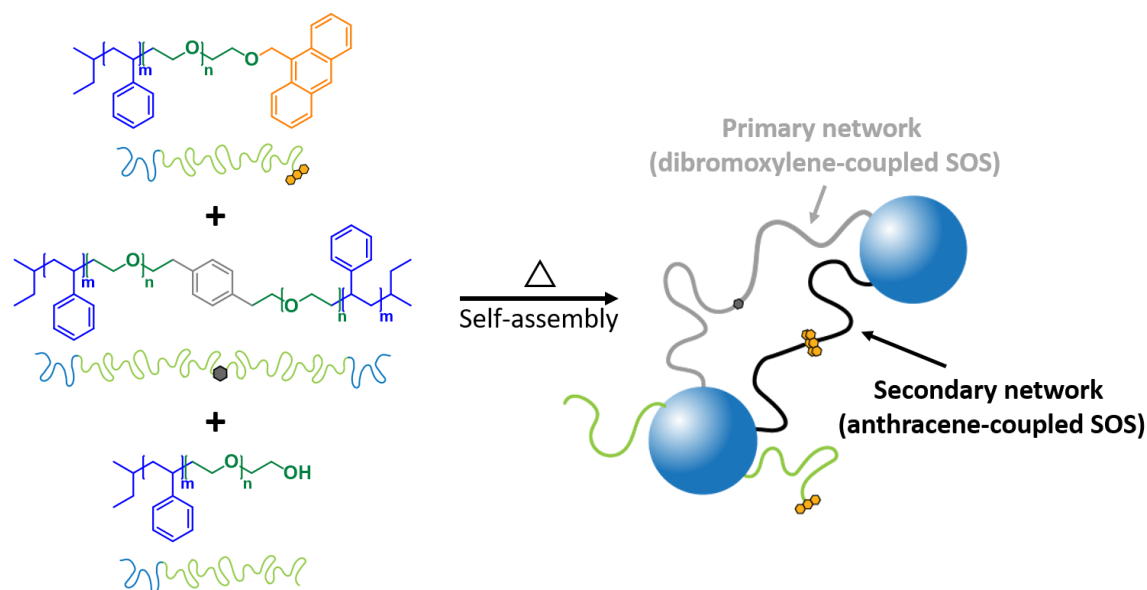
Figure 6.1. SO-anth, SOS, and SO block copolymer components shown to self-assemble in the melt-state to form micelle-like spheres comprising PS cores and dangling anthracene- or hydroxyl-functional PEO chains (green). The primary network present upon self-assembly is made of permanent dibromoxylene-coupled PEO tethers (gray), and anthracene-coupled PEO tethers (black) created upon irradiation of the self-assembled network comprise the secondary network.

6.3 Results and Discussion

6.3.1 Synthesis and Material Characterization

Studies were performed on three component blends containing SO-anth, SO-OH, and SOS. Two blend compositions were investigated. One blend (SOS-24) was comprised of 24 mol% SOS, 50 mol% SO-anth, and a balance of photoreactively inert SO-OH. The second blend (SOS-17) was comprised of 17 mol% SOS, 66 mol% SO-anth, and a balance SO-OH. (see **Table S6.1**). All blend components were derived from a one-pot SO diblock copolymer synthesis (f_{PS} = 0.124, M_n = 72900 g mol^{-1}, PDI = 1.04) carried out using anionic polymerization techniques.[26]

After completed polymerization of the PEO block, living SO (with a terminal potassium alkoxide) was partitioned into separate reactors and either coupled using dibromoxylene to form SOS (with residual SO-OH) or functionalized using 9-chloromethyl anthracene to form SO-anth through displacement of the chlorine by nucleophilic substitution.[31] Functionalization with anthracene was estimated to be approximately quantitative using ^{1}H NMR peak integrations. Molecular weight distributions of the SOS/SO-OH and SO-anth products were analyzed using size exclusion chromatography (SEC), which confirmed partial SOS coupling in the former, and absence of significant coupling in the latter (**Figure S6.1**). The SOS/SO-OH product was further fractionated to achieve a final SOS composition of 34 mol%. The two blend compositions described above were then gravimetrically prepared by combining the fractioned SOS and SO-anth products, with the final SOS/SO-X blend ratio confirmed using SEC (**Table S6.1**). SEC could not distinguish between SO-OH and SO-anth.

These BCP blends were self-assembled in the melt to form SOS-tethered spherical micellar structures as confirmed by SAXS (**Figure S6.2**), each containing a hydrophobic poly(styrene) core and a poly(ethylene oxide) corona, with anthracene functional chain ends comprising the majority of the non-tether population and non-photoreactive hydroxyl functional chain ends comprising the balance. The presence of the non-photoreactive SO-OH in these blends was purely the consequence of limitations in the efficiencies of fractionation, for which SOS purity had to be balanced against diminishing sample sizes. These two blends of photoactive micelle networks could then be irradiated (λ = 365 nm, I = ~30 mW cm^{-2}) while still in the melt-state following self-assembly, or after being cooled and subsequently swollen. In either case, the effect of irradiation was to create additional, secondary tethers (network strands) between micellar units beyond those produced by the original SOS concentration. However, the swelling

139

behavior and mechanical impact of the secondary network of tethers was dramatically different depending on the state (melt or swollen) of the blend when the photo installation took place.

6.3.2 Photoinstallation of a secondary network

To study the effects of a photoinstalled secondary network, the self-assembled blends of SOS-24 and SOS-17 were irradiated for 20 min (λ = 365 nm, I = ~30 mW cm^{-2}) under purge of inert argon gas in either the melt or swollen state. As shown in **Figure 6.2b**, irradiation in the melt state resulted in the installation of an additional 11 mol% SOS for both blend compositions (producing final SOS concentrations of 34.9 and 28 mol% for SOS-24 and SOS-17, respectively), while irradiation after equilibrium swelling in DI water produced only a 6 mol% increase in SOS content beyond the original SOS concentration (final SOS concentrations of 29.5 and 23 mol% for SOS-24 and SOS-17, respectively). This limitation in swollen-state photocoupling is suspected to be a consequence of decreased micelle proximity in the dilute state, as well reduced UV intensity as a function of depth due to absorbance by water.[23] The latter being a limitation absent in the melt state.
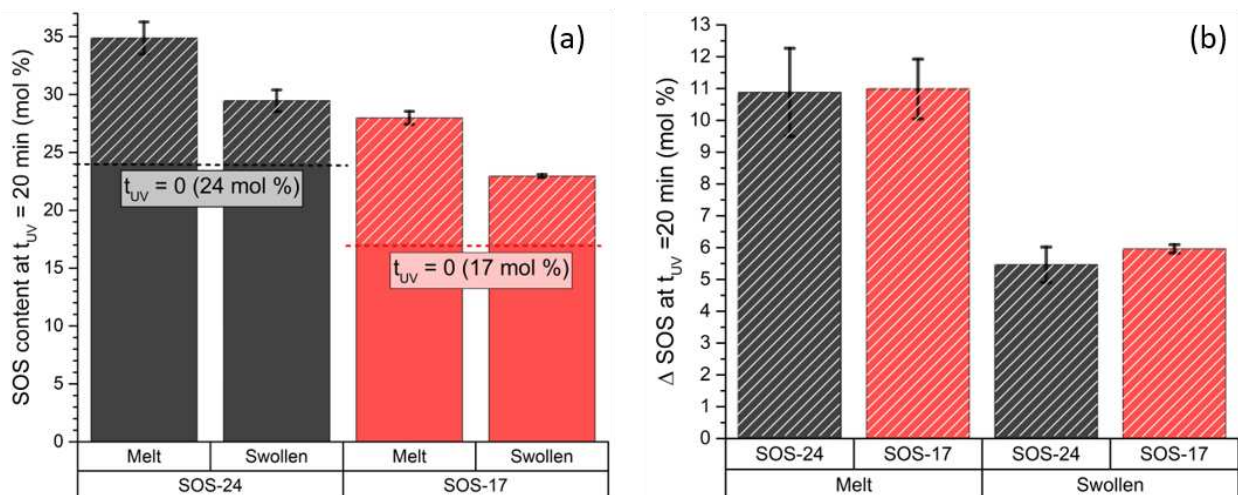
Figure 6.2. (a) Comparison of SOS concentration following irradiation (365 nm, 30 mW/cm^{-2}) of SOS-24 (black) and SOS-17 (red) samples for 20 min in the melt and swollen states. **(b)** The amount of photoinstalled SOS (ΔSOS) appears to be consistent between SOS-24 and SOS-17 when irradiated in the same state (melt or swollen). Non-irradiated controls for each blend are shown as dotted lines.

After photoinstallation of the secondary network, both melt and swollen-state samples were then placed in water and allowed to swell to equilibrium dimensions. As expected, melt photocoupled samples swelled less than non-irradiated swollen controls in both blends investigated (**Figure 6.3**). In the melt, the photoinstalled SOS population effectively adds as tethers which are largely, if not completely, indistinguishable topologically from the primary SOS network. Thus both the original and photoinstalled tether populations combine to restrict swelling through an increased number of chain entanglements present in the melt and physically trapped upon vitrification of the PS cores during cooling.

Unexpectedly, both blends experienced increased swelling after irradiation in their equilibrium swollen states, measured relative to their non-irradiated controls (**Figure 6.3**), despite

experiencing a net increase in SOS concentration. Irradiation in this initial (swollen) equilibrium state was expected to result in no change swelling, due to the dominant role of entanglements in the osmotically stressed primary network in determining the degree of swelling possible by the system. That is, the addition of a secondary, unstressed interpenetrating network within the framework of the taut primary network was anticipated to have no significant influence on swelling. Thus, increased swelling ability suggested possible concomitant degradation of the primary network during photoinstallation of the secondary network due to UV-triggered radical generation. This supposition was confirmed by a simple control experiment in which irradiation of non-photoactive SOS triblock copolymer species showed a reduction in SOS concentration by as much as 5 mol% (example trace shown in **Figure S6.3**). This phenomenon was not directly observable in melt-photocoupled blends because any breakdown of the primary network tethers was obscured by their effective replacement with topologically equivalent photoinstalled tethers in the same state of non-stressed entanglement. Thus the final change swelling dimensions were always the product of the net increase in SOS concentration acting to further restricted swelling relative to the non-irradiated control.
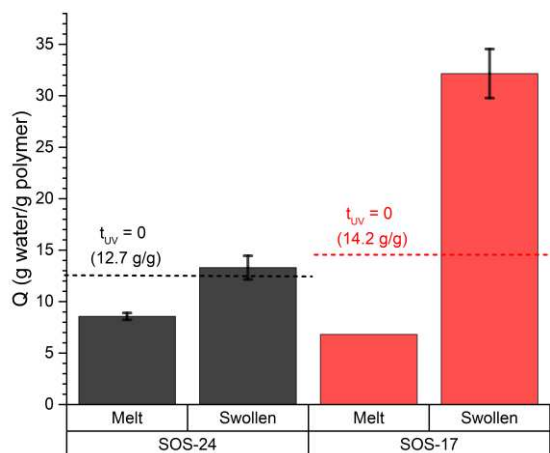
Figure 6.3. Comparison of swelling ratios of SOS-24 (black) and SOS-17 (red) samples irradiated in the melt or swollen states for 20 min (365 nm, 30 mW/cm^{-2}) with non-irradiated controls for each shown as dotted lines. Samples irradiated in the melt-state swell less than their respective controls and their swollen counterparts. Samples irradiated while swollen show a subsequent increase in swelling due some minimal breakdown of the primary network with exposure to UV.

After swelling to their equilibrium dimensions, all samples underwent mechanical testing to determine effects of secondary network installation. Each was subjected to two unconfined compressive cycles to 50% strain, at a strain rate of 5% s^{-1}, showing a small degree of recoverable hysteresis during removal of stress (**Figure S6.4**). Hydrogels photocoupled in the melt state and then swelled exhibited increased compressive moduli relative to nonirradiated control samples (**Figure 6.4**). For example, irradiated SOS-24 exhibited a more than 2-fold increases in mean compressive modulus from 100 to 234 kPa. SOS-17 behaved similarly, with an increase in mean compressive modulus from 89 to 204 kPa. This increase is consistent with swelling data, in that upon irradiation, samples exhibited reduced water uptake in response to the net overall increase in tether concentration. Photocoupling in the swollen state, however

decreased the compressive modulus to below that of the non-irradiated state (from about 99.9 to 49.2 kPa in SOS-24, and 88.6 to 13 kPa in SOS-17). This result is consistent with the hypothesis developed from observing increased swelling in these same samples. That is, irradiation, while inducing photocoupling of the anthracene units and formation of new SOS tethers, simultaneously induces chain cleavage in the original tether population making up the primary SOS network. While net SOS content increased (as confirmed by SEC), this increase is the sum of a reduced primary SOS population and the newly installed secondary SOS population. SEC cannot distinguish between these populations. However, compressive testing can distinguish between the two populations, as the measured mechanical response is predominantly the result of the resistance to deformation provided by the osmotically stressed primary network. The unconfined compression test does not induce a mechanical strain sufficient to mechanically engage the newly installed secondary network of tethers (installed in an unstressed state). Thus, the decrease in compressive modulus is capturing the partial cleavage of SOS chains originally comprising the primary network. Interestingly, non-irradiated (t_{UV} = 0) SOS-17 exhibits a compressive modulus close to that of SOS-24 irradiated in the swollen state, implying that the mechanical response of its primary network is approaching that of a 17 mol% SOS hydrogel. While a more rigorous investigation would be required to confirm the actual percent change, the similarity in compressive moduli suggests about a 7 mol% loss of primary SOS tethers when irradiated in the hydrated state. This would imply a balance of 13 mol% photoinstalled SOS, comparable to the tether installation rates of melt-irradiated samples. A more in-depth study could likely correlate modulus or Q to SOS content, providing a means to estimate primary and secondary SOS population distributions following irradiation.
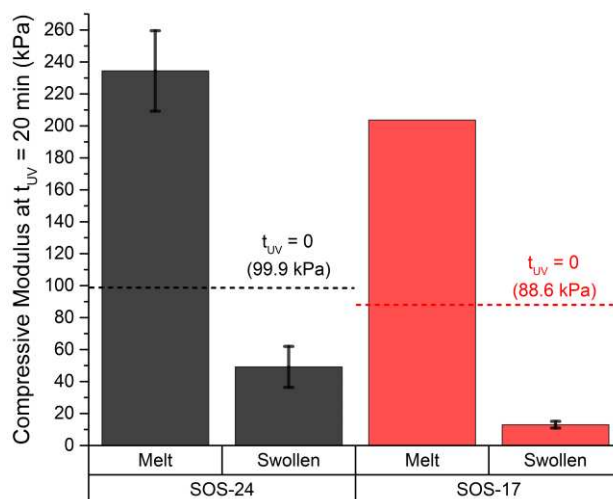
Figure 6.4. Comparison of compressive moduli of irradiated SOS-24 (black) and SOS-17 (red) samples in the melt and swollen states, with non-irradiated controls for each shown as dotted lines. Samples irradiated in the melt state and swollen to equilibrium exhibited an increase in compressive modulus, while those irradiated after being swelled to equilibrium experienced a decrease in modulus.

In order to capture the effects of the secondary network on mechanical behavior of the photocoupled hydrogels, samples were subjected to tensile testing at 2 % strain s^{-1} until break or slip from the testing fixtures (**Figure S6.5**). It must be noted that the data presented is specifically selected as a representation of the potential of the system, therefore does not include tests which resulted in non-midsubstance failure. While tensile testing is an effective way to demonstrate contribution of the secondary network to mechanical properties of the hydrogel due to later engagement, tensile tests are highly vulnerable to bubble and sintering defects often present in these hydrogels as a product of limited laboratory processing capabilities. We are not yet able to divorce the sample quality from tensile extension results, therefore the highest quality tests and samples are presented here. That said, small strain tensile moduli appear to be largely independent of sample quality, and are compared in **Figure 6.5a**. Photocoupling in the melt (on

average) increased the tensile moduli (from 40 to 90 kPa in SOS-24 (black), and 15 to 30 kPa in SOS-17 (red)) while photocoupling equilibrium swollen gels appeared exhibit initial tensile moduli below that of non-irradiated hydrogels (from 40 to 30 kPa in SOS-24 (black), and 15 to 10 kPa in SOS-17 (red). Small-strain tensile moduli upon photocoupling (whether swollen or in the melt) are comparable to that measured during compression testing, and therefore are taken to be characteristic of the primary network. However, tensile extension and toughness data reveal the effects of the secondary network installed in the swollen state. Though moduli dropped when photocoupled in the swollen state due to presumed breakdown of the primary SOS network, both SOS-24 and SOS-17 samples exhibited higher toughness values than their melt-photocoupled counterparts, as seen in **Figure 6.5b**. This is because melt photocoupling results in largely indistinguishable "primary" and "secondary" networks.
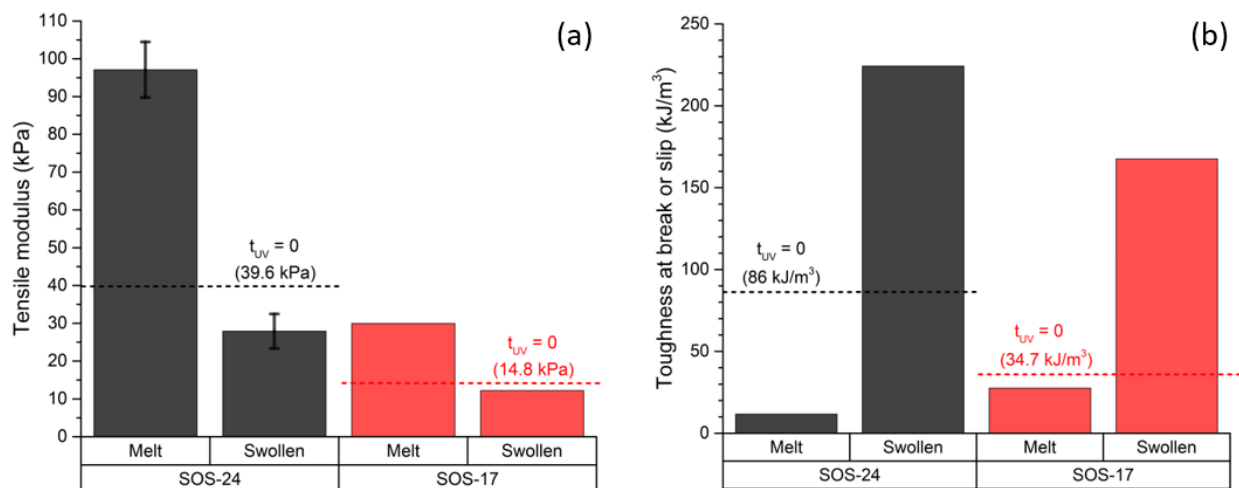

Figure 6.5. (a) Comparison of tensile moduli of equilibrium-swollen SOS-24 (black) and SOS-17 (red) samples irradiated to form secondary networks in either the melt or swollen states. Tensile moduli of samples increased when irradiated in the melt prior to swelling, while moduli decreased when irradiated at equilibrium swelling dimension**s. (b)** Toughness values extracted

from this tensile data showed a significant average increase for samples for which secondary networks were installed in the swollen state. Irradiated samples of swollen SOS-24 and SOS-17 exhibited a twofold and five-fold increases in toughness, respectively, relative to non-irradiated controls. Secondary networks installed in the melt state did not have a positive effect on toughness. Non-irradiated controls for each SOS-17 and SOS-24 are shown as dotted lines.

6.3.3 Swollen-state photopatterning to impose anisotropy

Both the ability to install tethers *in situ* combined with then influence of secondary network installation on toughness when performed in the swollen equilibrium state presented the opportunity to spatially pattern regions of reinforcement (higher tethering) for increased toughness in swollen hydrogel blends. This was especially intriguing in the context of introducing mechanical anisotropy, a common feature of soft biological tissues. To study whether photopatterning could produce mechanical anisotropy in these hydrogels, SOS-24 samples were melt processed into dry, 0.9 mm thick rectangles (8.8 x 2.9 mm) and swelled in water to their equilibrium dimensions. The swollen samples were then irradiated through a photomask of alternating 83 μm wide black and transparent stripes, with the stripes oriented either parallel or perpendicular to the planned direction of tensile loading (parallel to the long edge of the rectangular sample). Hydrogels patterned with parallel striping were anticipated to exhibit improved tensile toughness due to the alignment in the direction of patterned reinforcement and the direction of applied load. Hydrogels patterned with striping perpendicular to the direction of applied loading were expected to experience little to no improvement in tensile toughness, despite comparable increases in overall SOS tether concentration.

After photopatterning, visible striations appeared on the hydrogels and were made more distinct after subsequent swelling to equilibrium, with 0.5 mm wide features of about 5 μm in

height as determined by physical profilometry of the hydrogel surfaces (**Figure 6.6a**). Digital photographs of the hydrogels and SEM images the patterned samples dried and re-swollen in nonvolatile ionic liquid showed clear evidence of the striated patterns continuing throughout the depth of the irradiated hydrogels (**Figures 6.6a-c**), Notably, the swollen striations were observed to continue down the corresponding edge faces of the hydrogel, while remaining absent from the two faces parallel to the striations.
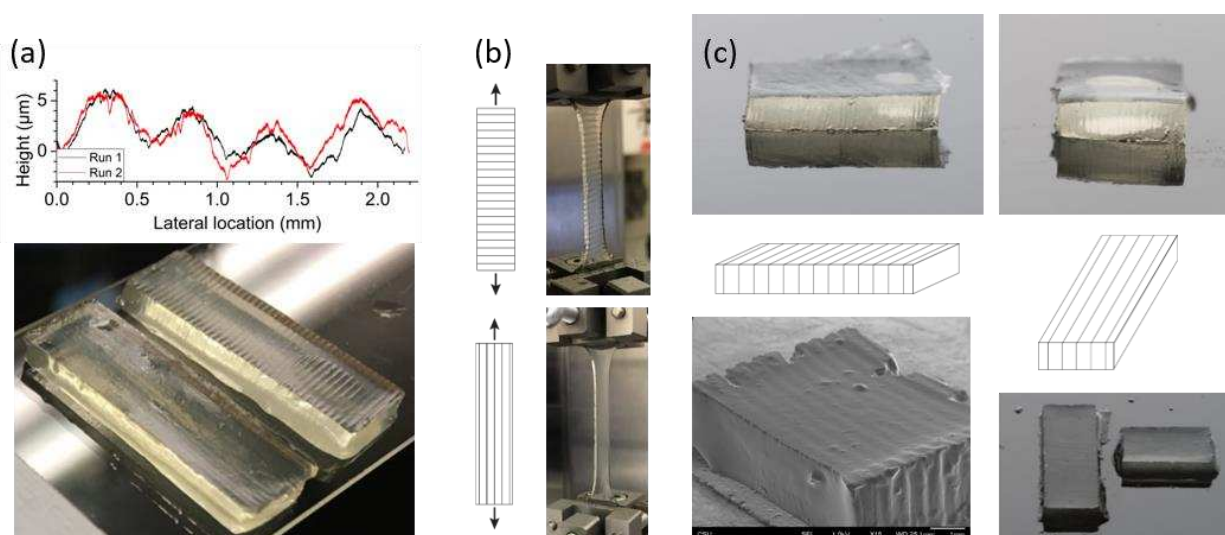
Figure 6.6. (a) Hydrogels photopatterned for studies of anisotropy were photographed subjected to physical profilometry to study small surface striations. **(b)** Cartoons and photographs of tensile experimental design are shown. **(c)** Striations can be seen to continue down the edge faces of the gel, indicating the full depth of patterned tethering. These features are particularly clear in SEM taken of sample swollen with ionic liquid (1-ethyl-3-methylimidazolium bis(trifluoromethylsulfonyl)imide ($[EMIM][Tf_2N]$)) and then patterned. The ionic liquid was used exclusively for direct SEM imaging of the swollen architecture under vacuum.

SOS triblock copolymer content of SOS-24 swollen samples increased from 24 to 28.8 mol% SOS for hydrogels photopatterned perpendicular to the direction of applied load and from 24 to 30.5 mol % SOS in hydrogels photopatterned parallel to the direction of load. (**Figure 6.7a**). The slight discrepancy in SOS content between the differently photopatterned samples is a believed to be largely a consequence of a slight differences in total photopatterned area of the samples isolated for SEC characterization, and is not believed to be significant in terms of the overall conclusions drawn from the testing results. Fully irradiated control samples gained almost twice the amount of photo-installed SOS as their striped counterparts, with a total SOS content of about 34.9 mol % after irradiation. This reduction by approximately half the added SOS tether concentration in the patterned samples is consistent with the equivalency between masked and unmasked line widths in the selected pattern. All irradiated samples were then placed back into water and allowed to reestablish their preferred equilibrium swelling dimensions post UV exposure. In general, very little change in equilibrium swelling dimensions was observed for any of the samples (**Figure 6.7b**), with only slight increases in swelling ratios detected for the irradiated samples. Such slight increase is likely a consequence of irradiation-induced cleavage of the primary network tethers as discussed previously, although in these cases the magnitude of such cleavage seemed to be rather minimal.
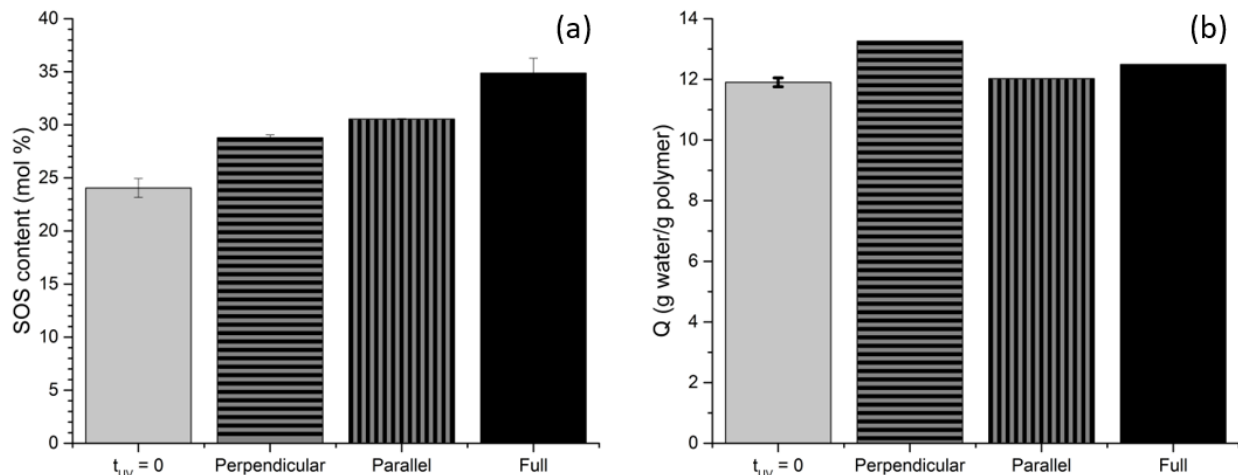
Figure 6.7. (a) Comparison of SOS content and **(b)** swelling ratio (Q, g water per g polymer) of hydrogels 1) not irradiated (gray), 2) patterned perpendicular (horizontal lines) and parallel (vertical lines) to the direction of intended tensile loading, and 3) fully irradiated. The UV irradiated gels were exposed for 20 min.

The assessment of imposed directionality in mechanical properties was examined by comparing toughness values of non-irradiated and fully irradiated controls to hydrogels pulled perpendicular to and parallel to their striated photopattern. Again, it must be noted that the toughness data presented here was specifically selected as a representation of the potential of the system, therefore does not include tests which did not appear to demonstrate true limits of extension of the material as determined by clean mid-substance failure. As seen in **Figure 6.8a and b**, the sample pulled parallel to the striations exhibited improved extension and toughness over samples pulled perpendicular to striations of the same reinforcement region line width. Notably, samples photopatterned along the direction of applied tensile load exhibited toughness values very similar to fully irradiated hydrogels, despite lower overall SOS triblock copolymer concentrations (**Figure 6.7a, 6.8c**). The ability to achieve equivalent toughness to fully irradiated hydrogels of higher SOS concentration means that more uncoupled, photoactive chain ends are

still available to create tethers. This presents the opportunity to further exploit the untapped tethering from greater availability of uncoupled anthracene chain-ends in future work. In the experiment detailed in this report, we stressed the primary SOS network through swelling, and then photopatterned regions of reinforcement parallel to the direction of eventual tensile stress up to a maximum SOS content achievable in 20 min. The population of additional anthracene end-groups left uncoupled between the reinforced regions (which, before the photopatterning, would already have been photocoupled into tethers) has the potential to be further used to create what is effectively a third network, if photoinstalled in a state distinctly stressed from the primary and secondary ones. For instance, if we photopatterned the striations onto a swollen primary network as before, the material could then be dehydrated to some point (e.g. half of its equilibrium water content), and then again photopatterned with parallel striations. This would add additionally reinforced regions using the population of still-available anthracene substituents, which were not coupled during initial photopatterning. In contrast, the same hypothetical experiment on a fully irradiated gel (versus a striated one) would not allow for as highly tethered a trinary network, given the relatively limited availability of anthracene chain-ends left to be photocoupled. This suggests access to an entirely new handle by which to more finely tune mechanical properties of these versatile materials, and potentially improve toughness to an even greater degree.

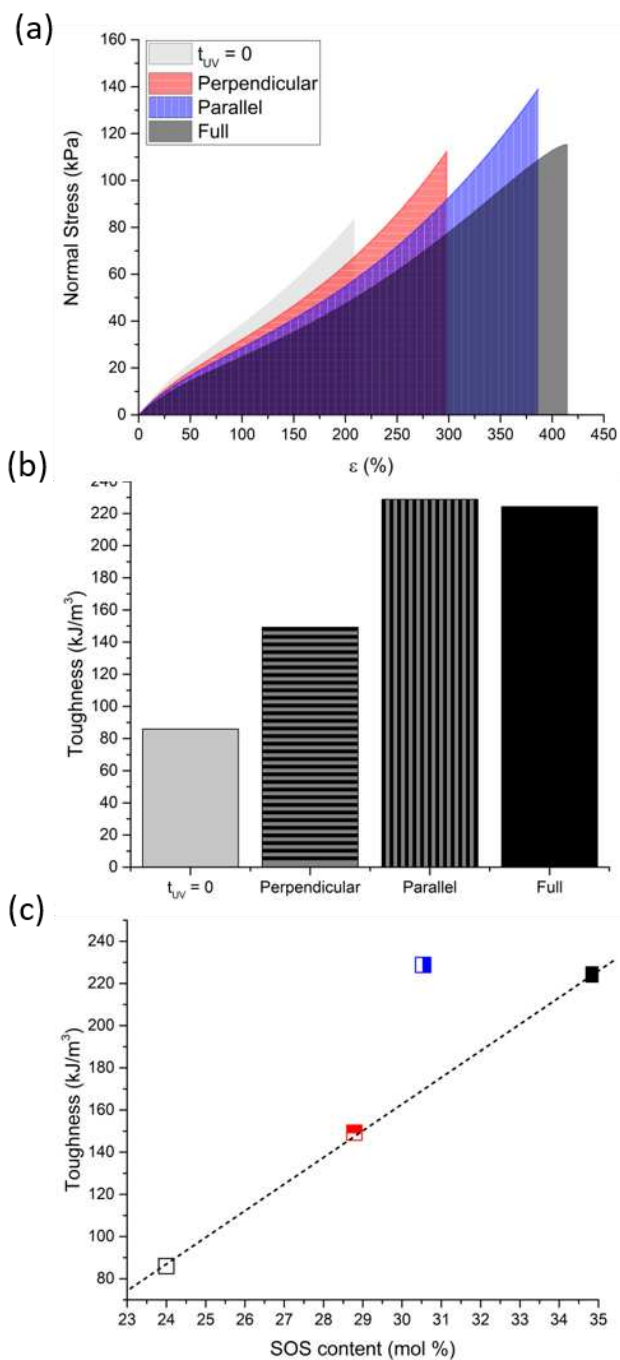**Figure 6.8. (a)** Swollen hydrogels were subjected to tensile testing at 2% strain s⁻¹. The tensile response of nonirradiated (light gray) and fully irradiated (dark gray) controls were compared to photopatterned hydrogels pulled perpendicular (red) or parallel (blue) to the patterned lines of reinforcement. Areas underneath tensile curves are shaded to pictorially indicate relative

toughness. **(b)** Calculated toughness is shown to be comparable between fully irradiated hydrogels and those pulled parallel to the patterned reinforcement lines. Both show toughness higher than non-irradiated samples or those pulled perpendicular to patterned striations. **(c)** A plot of toughness of a function of SOS content. All irradiated samples received 20 min of UV exposure (365 nm, 30 mW cm^{-2}).

6.3.4 Melt-state photopatterning to impose surface topography

Network formation through UV irradiation and subsequent tunability of swelling ratio implied an intrinsic ability for the introduction of both shape[21] and surface features through photopatterning. The hypothesis was based on our recognition that 1) we could spatially control SOS concentration through patterning in the melt-state, and 2), more highly tethered (photocoupled) regions exhibit a reduced ability to osmotically expand due to the increase in network entanglements. Thus, by patterning the SOS concentrations installed, the regional differences in swelling would manifest as surface topography. These photopatterning capabilities were explored using self-assembled SOS-24, which was photopatterned in the melt state using a variety of photomasks (printed by CAD/Art Services, Inc.). The goal was to generate raised surface shapes and features in masked regions, where added SOS installation was negligible and tether concentrations remained at the lower (more swellable) baseline concentrations of 24 mol%. As seen in **Figure 6.9a**, masking in the shape of a thin spiral (**Figure 6.9a inset**) yielded a raised, spiral-shaped feature on the surface of the hydrogel. **Figure 6.9b** shows the negative of the original spiral pattern, where everything but a spiral shape is masked (**Figure 6.9b inset**). This yielded swelling of the majority non-irradiated area, while the more highly tethered spiral remains depressed into the surface of the hydrogel. **Figure 6.9c** shows the effective transfer of a cartoon image of a micellar building block, with the mask itself shown in the inset (**Figure 6.9c**

inset). Although achieving proper photographic contrast with a transparent hydrogel proved challenging, the captured image shows the highly-detailed cartoon could be reproduced with reasonable fidelity on the soft hydrogel surface.
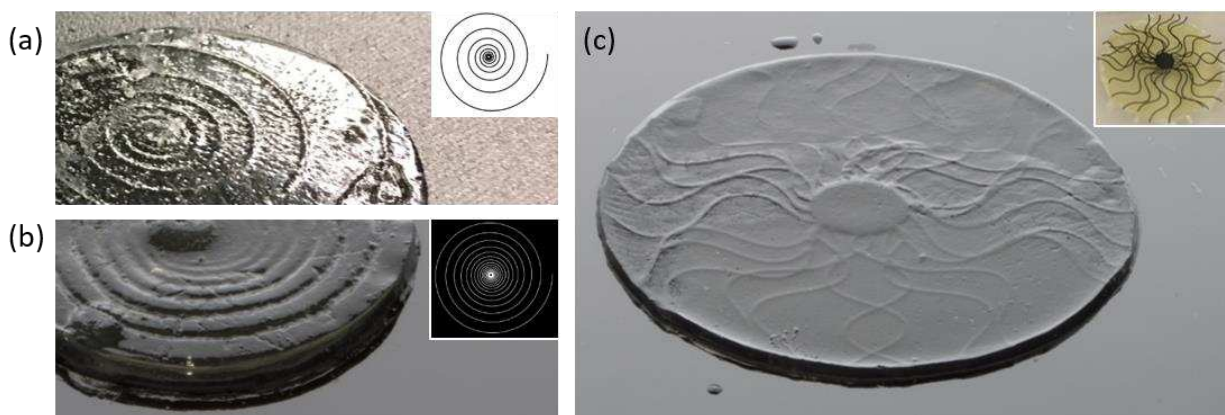
Figure 6.9. (a) Positive spiral transferred to the soft hydrogel surface using a spiral mask (inset) **(b)** Negative spiral transferred using the negative of the mask (inset) used in (a). **(c)** Positive micelle shape transferred using a mask containing a cartoon image of a micelle.

6.4 Conclusions

Blends of SO, SO-anth, and SOS copolymers were self-assembled in the melt state to form a photoactive BCP micelle network held together with a primary mesh of SOS triblock copolymer. The effects of photoinstallation of a secondary SOS network using available dangling SO-anth chains were distinctly different depending on whether samples were irradiated in the dry melt, or at their swollen equilibrium dimensions. Samples irradiated at equilibrium, resulting in the primary and secondary networks in separate states of stress, exhibited significant improvements in toughness compared to the melt-photocoupled counterparts where the secondary network was installed under equivalent stress as the primary SOS tethers. Adjustment of the initial primary SOS content did not appear to affect these results.

Photopatterning hydrogels in the swollen state allowed direct installation of the secondary network in targeted regions of the hydrogel. This ability to define regions of reinforcement led to an exploration of the effects of anisotropy in tether concentration on mechanical properties. Photomasks were then used to install evenly distributed parallel lines of secondary networks of SOS tethers. The response to tensile testing varied depending on direction of applied tensile loading, with loading applied parallel to the lines of increased tether concentration resulting in significantly higher toughness values than samples for which the tensile loading was applied perpendicular to the patterned striations of higher SOS concentrations. Notably, patterning lines parallel to the load direction produced toughness comparable to homogeneously (fully) irradiated hydrogels.

Photopatterning in the melt state, did not produce increased toughness observed to manifest in samples irradiated in the swollen state. However, it did result in producing distinct surface topography, with raised features appearing as a result of spatial differences in swelling capacity produced through selective masking. Masked areas, with no added SOS tethers relative to the primary concentration added prior to irradiation, appeared more swollen than UV exposed areas, allowing for highly detailed transfer of unique topographies onto the hydrogel surfaces.

Overall, the ability to install tethers at any point after self-assembly and at different states of hydration allows for a powerful level of control within this unique, photoactive micelle construct. In particular, the ability to install multiple networks through simple UV exposure provides access to tunable and directionally-dependent states of swelling and material toughness. This type of versatility in a hydrogel produced from a single block copolymer species is a rather remarkable achievement.

6.5 Experimental

6.5.1 Materials and Methods

General. Styrene (99%, 50 ppm *p*-tert-butylcatechol inhibitor, Aldrich) was purified by static vacuum (15-30 mTorr) distillations from di-*n*-butylmagnesium (1.0 M in heptane, Aldrich) at 40 °C. Ethylene oxide (99.5+%, compressed gas, Aldrich) was purified by successive distillations from di-*n*-butylmagnesium (1.0 M in heptane, Aldrich) at 3 °C. *sec*-butyllithium (1.3 M in cyclohexane/hexane, Fisher) was used as received. Potassium naphthalenide solution was prepared according to a previous report.[19] 9-(chloromethyl)anthracene (98%, Aldrich) and α,ά-dibromo-*p*-xylene (97%, Aldrich) were dried under high vacuum for several hours prior to use. Tetrahydrofuran (THF) was degassed by sparging with argon (10 psi) for a period of 45 minutes and then purified over two molecular sieve columns of neutral alumina (Glass Contour, Inc.). Cyclohexane (CHX) was degassed with argon and purified through a column of neutral alumina followed by a column of Q5 copper (II) oxide catalyst (Glass Contour, Inc.). Hydrogels were swollen using DI water of 18.2 MΩ resistivity (Evoqua/U.S. Filter Service Deionization). Other common chemicals and solvents were used as received unless otherwise stated. Ultra-high purity argon (99.998% Airgas) was passed through a column of 5 Å molecular sieves with Drierite (Agilent) and oxygen absorbing purifier column (Matheson Tri-gas). Glassware and polymerization reactors were flamed under vacuum and backfilled with argon (3 X).

Synthesis (one-pot) of PS-PEO-PS, PS–PEO (SO) and PS-PEO-anthracene (SO-anth). Hydroxyl-terminal polystyrene–*b*–poly(ethylene oxide) (PS–PEO, SO), anthracene-terminal polystyrene–*b*–poly(ethylene oxide), and polystyrene–*b*–poly(ethylene oxide)-*b*-polystyrene were synthesized using a one-pot strategy. This involved using a two-step anionic polymerization of styrene and ethylene oxide monomer[19] followed by separation of the live SO

156

diblock copolymer into three fractions for either hydroxyl termination (SO-OH), anthracene termination (SO-anth), or coupling with dibromoxylene (SOS). In brief, the first step involved synthesis of a hydroxyl-terminal polystyrene macroinitator (3.6 g PS, $M_{n,PS}$ = 8064 g mol^{-1}, $M_{w,PS}/M_{n,PS}$ = 1.05, SEC (polystyrene standards)), [19] from which ethylene oxide was polymerized to form a live SO diblock copolymer. This live polymer (dissolved in THF) was then separated, with ~1/6 of the volume sent to via cannula into a reactor with an excess (~10 x) of 9-chloromethyl anthracene for diblock copolymer termination with anthracene, ~1/3 to a molar equivalent of HCl in a methanol solution for termination of the chain with a hydroxyl group, and the rest retained to couple using a half molar equivalent of dibromoxylene added slowly via syringe pump.

The SO-OH and SOS were each precipitated from 25 °C pentane, then vacuum filtered and dried in vacuo for three days. The volume fraction of the PS block in the final diblock copolymer was determined to be 0.124 (using nominal densities at 140 ˚C)[25] with an overall M_n = 72900 g mol^{-1} ($M_{w,SO}/M_{n,SO}$ = 1.04, SEC (PS standards)) calculated using the measured $M_{n,PS}$ and the relative ^{1}H NMR integrations. The batch set aside for coupling to SOS yielded a 50% by mass quantity of SOS relative to uncoupled SO-OH. Subsequent fractionation[19] and blending was performed to produce photoactive SOS-17 and SOS-24 blends.

The anthracene terminated block copolymer product was precipitated from 25 °C pentane twice. The material was then vacuum filtered and partially dried, then then re-dissolved in THF with 0.5 weight percent butylated hydroxyl toluene (BHT) added to act as a radical scavenger. The polymer was then dried in vacuo (25 °C, ~24 h) with the resulting block copolymer appearing as a yellow-tinged white powder. SEC (polystyrene standards): M_w/M_n = 1.04. ^{1}H NMR (400 MHz, CDCl$_3$, δ): 8.4–8.5 (m, anthracene H$_1$, H$_8$ and H$_{10}$), 7.9–8.0 (d, anthracene

H$_4$ and H$_5$), 7.4–7.6 (m, anthracene H$_2$, H$_3$, H$_6$ and H$_7$), 6.2–7.2 (b, –CH$_2$–C(R)H–C$_6$*H*$_5$), 5.5 (s, –O–C*H*$_2$–anthracene), 3.4–3.8 (b, –C*H*$_2$–CH$_2$–O–), 1.1–2.3 (b, –C*H*$_2$–C(R)*H*–C$_6$H$_5$), 0.8–0.9 (b, CH$_3$–C*H*$_2$–C(R)H–CH$_3$), 0.5–0.7 (b, C*H*$_3$–CH$_2$–C(R)H–C*H*$_3$) See **Figure S6.1** for clarification of anthracene proton assignments, which are consistent with a previous report.[26] Relative integrations of anthracene to initiator protons suggest a quantitative addition within ^{1}H NMR integration error (~5%). The overall yield of the one-pot synthesis was estimated to be above 90%.

SO/SOS/SO-anth blends. SOS-17 and SOS-24 polymer blend samples were produced by combining targeted amounts of SOS/SO with SO-anth and SO via solution blending in benzene using a stir bar. The blends were then freeze-dried to produce the desired homogenous polymer blends used throughout this report.

UV irradiation/photopatterning. SOS-17 and SOS-24 photoactive polymer blends were pressed as discs or rectangles (150 °C, 500 psi for 15 min), then stored in the dark prior to use. Irradiation in the melt-state took place in the molds samples were pressed in to retain shape, sandwiched by glass slides, while swollen-state irradiation to install a secondary network were simply sandwiched with the slides. UV curing took place using an OmniCure Series 2000 UV curing system with a 200-Watt mercury arc lamp, in conjunction with an Asahi Spectra Co high transmission band pass 365 nm filter. The intensity at the surface of the sample was 28–32 mW cm^{-2} (measured in the range of 200–600 nm with an Omnicure R2000 Radiometer). Photopatterned samples used masks placed between the light source and upper glass slide, which were printed by CAD/Art Services, Inc. with emulsion down. All samples were exposed to 365 nm light for 20 minutes.

6.5.2 Measurements

NMR and GPC. ^{1}H NMR spectra were recorded at room temperature on a Varian Inova 400 MHz spectrometer with a d1 pulse delay of at least 20 s to ensure complete relaxation of end-groups. Spectra were referenced to $CDCl_3$ solvent. Size exclusion chromatography (SEC) spectra were collected on a Viscotek GPC-Max chromatography system outfitted with three 7.5 x 340 mm Polypore™ (Polymer Laboratories) columns in series, a Viscotek differential refractive index (RI) detector, and an Alltech column oven (mobile phase DMF, 40 °C, 1 mL min^{-1}).

SAXS. Small Angle X-ray Scattering (SAXS) data were collected on a Rigaku S-Max 3000 High Brilliance three pinhole SAXS system outfitted with a MicroMax-007HFM rotating anode (CuKα), Confocal Max-Flux™ Optic, Gabriel multiwire area detector, and a Linkam thermal stage. Dry polymer samples were sandwiched between Kapton windows (0.05 – 0.5 mm thick X 10 mm diameter). Scan times were typically on the order of 3600 s, with temperature ramp rates of 10 °C min^{-1}

Mechanical testing and Rheology. Mechanical performance of the hydrogels was quantified using a TA Instruments Advanced Rheometric Expansion System (ARES) rheometer. Swollen samples were subjected to unconfined compression testing to 50 % strain over two successive cycles (2% s^{-1}) at room temperature using a lower tool "cup bath" base and an 8 mm stainless steel upper parallel plate. For all samples, a constant force of approximately 5-10% compression was applied before any testing in order to ensure sufficient contact and prevent slip. Tensile tests were performed on rectangular hydrogel samples at room temperature using the normal force transducer of a TA ARES rheometer. TA rectangular torsion geometry test fixtures modified with sandpaper were used as tensile test grips, and a strain rate of 2 % s^{-1} was applied until slip or fracture. Engineering stress was calculated using cross-sectional area-normalized force.

Physical profilometry. Physical profilometry of the hydrogel topography was obtained using a Burker Dektak XT Stylus Profilometer. A force of 0.5 mg was applied to a stylus with radius 12.5 μm.

SEM. Scanning electron microscopy measurements were obtained using JEOL JSM-6500F field emission scanning electron microscope in the Central Instrument Facility at Colorado State University. It was operated at 1.0 kV at x15 magnification on the SOS-24 polymer blend swelled with [EMIM][Tf2N] ionic liquid, subsequently photopatterned to result in striated raised features and valleys.

Determination of changes in Q. Polymer blends were massed dry, and then massed again when swollen in water to their equilibrium dimensions to determine their swelling ratio, Q (g water per g polymer). Samples were also massed after coming to equilibrium again post-irradiation to determine whether any changes in water content occurred after this additional SOS triblock copolymer installation.

6.6 Supporting Information

6.6.1. Synthesis and material characterization of BCP blends and their component polymers
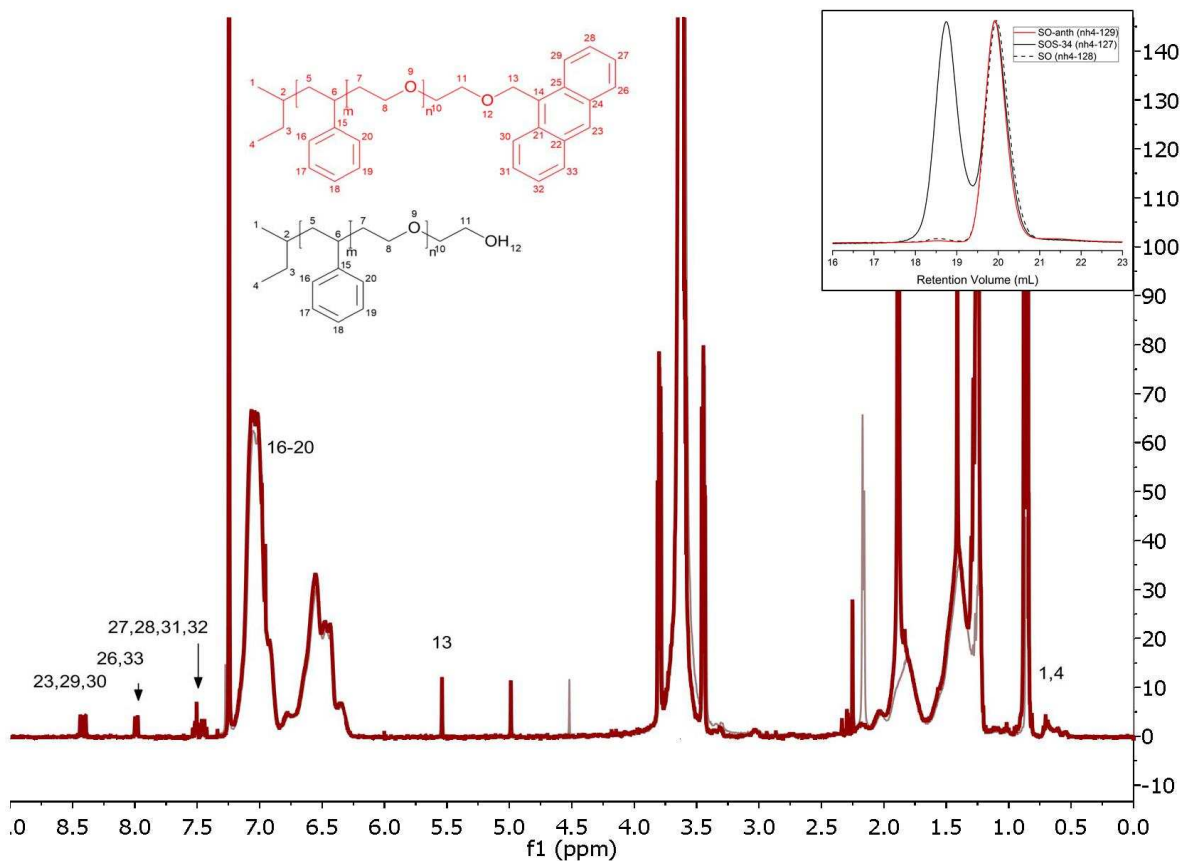
Figure S1. SO-OH (black) and SO-anth (red) ^{1}H NMR end-group peaks. SEC traces of SOS, SO-OH, and SO-anth show expected bimodal and monomodal molecular weight distributions, respectively (inset).

Table S1. Blend compositions (mol %) of SO-anth/SO-OH/SOS blends.

Sample	SO-anth	SO-OH	SOS
SOS-24	50	26	24
SOS-17	66	17	17

6.6.2. Photoinstallation of a secondary SOS network
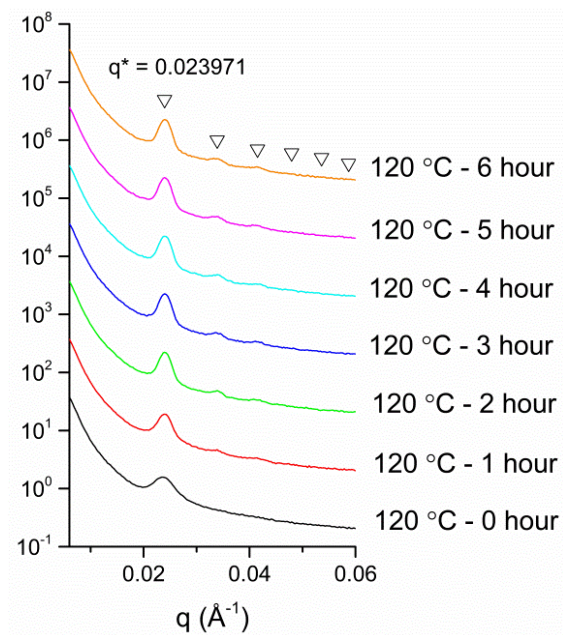
Figure S2. SAXS annealing (120 °C) of SO-anth, showing adoption of BCC lattice morphology of micelles from LLP beginning after one hour of annealing.
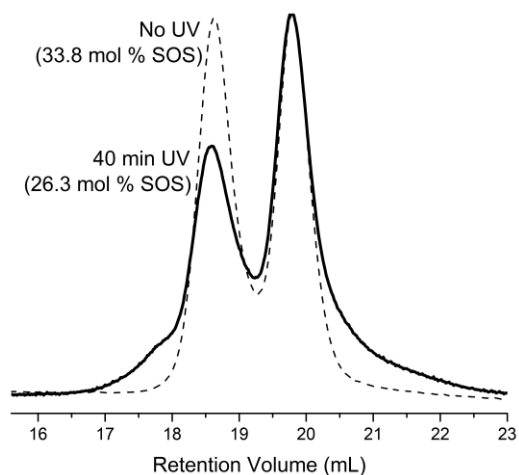
Figure S3. Effect 40 min irradiation on (non-photoactive) SOS-34. The SOS concentration was observed to decrease by about 7 mol % triblock copolymer.

6.6.3. Mechanical testing of photoactive BCP blends
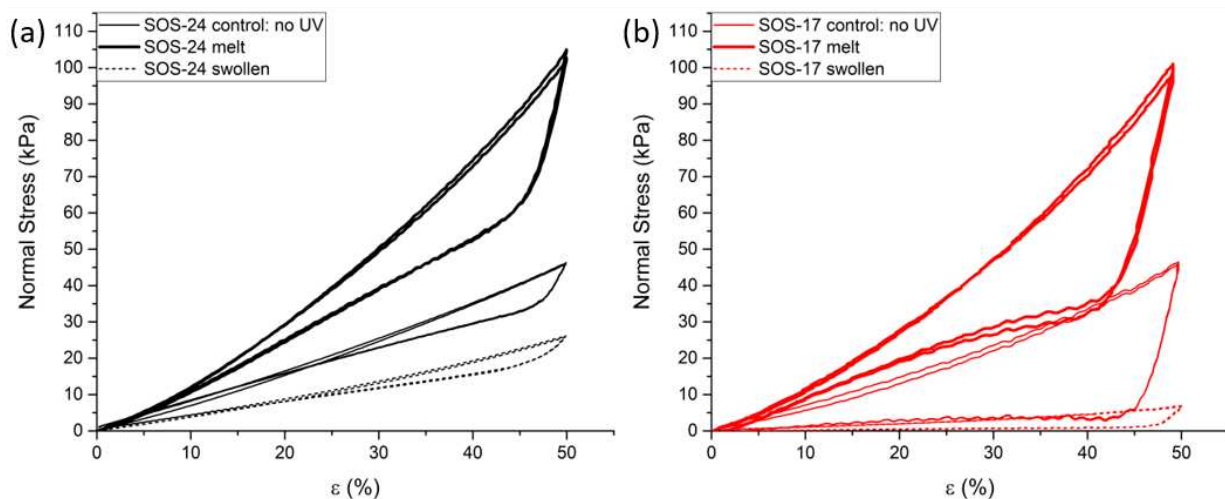
Figure S4. Two cycles of representative unconfined compression data on hydrogels compressed to 50% strain at 5% strain s^{-1}) for (a) SOS-24 and (b) SOS-17 blends, irradiated to form a secondary network in either the melt (solid, bold) or swollen (dashed) state. Controls, swollen without irradiation, are shown as a thin solid line.
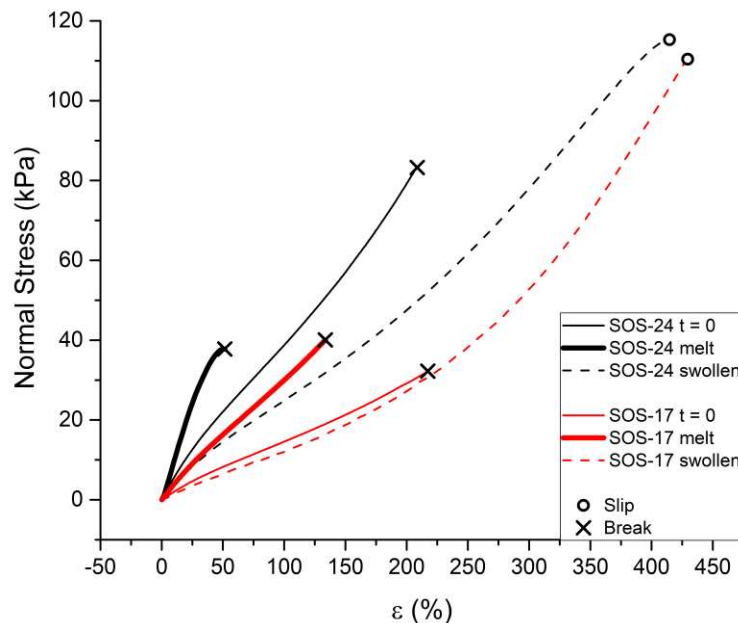
Figure S5. Representative tensile test data on equilibrium-swollen SOS-24 (black) and SOS-17 (red) blends irradiated to form a secondary network in either the melt (solid, bold) or swollen (dashed) state pulled at 2% s^{-1} strain. Samples with secondary networks installed in the melt exhibited increased moduli but loss in toughness, and while samples with secondary networks installed in the stressed swollen equilibrium state decreased in moduli but increased at least two-fold in toughness values.

6.6.4. Number of Trials per Experiment

Table S2.

# Trials	$Q_{initial}$				t_{UV}			
	8	**12**	**16**	**20**	**0**	**2.5**	**5**	**7.5**
G'	8	9	7	8	2	3	3	3
SOS	4	4	4	3	3	3	3	3
Q (SI)	7	7	7	8				
Tensile	2	3	2	2				

6.6.5. Sample Identification History

Table S3.

Manuscript ID	Lab Notebook ID
S-OH	DBW1142
SO-OH	NH4128
SO-anth	NH4129
SOS-34	NH4-127
SOS-17	NH4228
SOS-24	NH4170

References

1.   Kloxin, A. M.; Tibbitt, M. W.; Kasko, A. M.; Fairbairn, J. A.; Anseth, K. S. Tunable Hydrogels for External Manipulation of Cellular Microenvironments through Controlled Photodegradation. *Adv. Mater.* **2010,** 22, (1), 61-+.

2.   Liu, V. A.; Bhatia, S. N. Three-dimensional photopatterning of hydrogels containing living cells. *Biomed. Microdevices* **2002,** 4, (4), 257-266.

3.   Melchels, F. P. W.; Blokzijl, M. M.; Levato, R.; Peiffer, Q. C.; de Ruijter, M.; Hennink, W. E.; Vermonden, T.; Malda, J. Hydrogel-based reinforcement of 3D bioprinted constructs. *Biofabrication* **2016,** 8, (3).

4.   Chan, V.; Zorlutuna, P.; Jeong, J. H.; Kong, H.; Bashir, R. Three-dimensional photopatterning of hydrogels using stereolithography for long-term cell encapsulation. *Lab Chip* **2010,** 10, (16), 2062-2070.

5.   Tsurkan, M. V.; Wetzel, R.; Perez-Hernandez, H. R.; Chwalek, K.; Kozlova, A.; Freudenberg, U.; Kempermann, G.; Zhang, Y. X.; Lasagni, A. F.; Werner, C. Photopatterning of Multifunctional Hydrogels to Direct Adult Neural Precursor Cells. *Adv Healthc Mater* **2015,** 4, (4), 516-521.

6.   Bryant, S. J.; Cuy, J. L.; Hauch, K. D.; Ratner, B. D. Photo-patterning of porous hydrogels for tissue engineering. *Biomaterials* **2007,** 28, (19), 2978-2986.

7.   Davey, S. K.; Aung, A.; Agrawal, G.; Lim, H. L.; Kar, M.; Varghese, S. Embedded 3D Photopatterning of Hydrogels with Diverse and Complex Architectures for Tissue Engineering and Disease Models. *Tissue Eng Part C-Me* **2015,** 21, (11), 1188-1196.

8.   Suri, S.; Schmidt, C. E. Photopatterned collagen-hyaluronic acid interpenetrating polymer network hydrogels. *Acta Biomater* **2009,** 5, (7), 2385-2397.

9.   Xing, J. F.; Zheng, M. L.; Duan, X. M. Two-photon polymerization microfabrication of hydrogels: an advanced 3D printing technology for tissue engineering and drug delivery. *Chem. Soc. Rev.* **2015,** 44, (15), 5031-5039.

10.   Lane, A. P.; Maher, M. J.; Willson, C. G.; Ellison, C. J. Photopatterning of Block Copolymer Thin Films. *Acs Macro Lett* **2016,** 5, (4), 460-465.

11.   Gumuscu, B.; Bomer, J. G.; van den Berg, A.; Eijkel, J. C. T. Photopatterning of Hydrogel Microarrays in Closed Microchips. *Biomacromolecules* **2015,** 16, (12), 3802-3810.

12.   Yu, T. Y.; Ober, C. K. Methods for the topographical patterning and patterned surface modification of hydrogels based on hydroxyethyl methacrylate. *Biomacromolecules* **2003,** 4, (5), 1126-1131.

13.   Mitchell, G. R.; Tojeira, A. Role of Anisotropy in Tissue Engineering. *Procedia Engineer* **2013,** 59, 117-125.

14.   Murphy, J. G. Evolution of anisotropy in soft tissue. *P Roy Soc a-Math Phy* **2014,** 470, (2161).

15.   Helgeson, M. E.; Chapin, S. C.; Doyle, P. S. Hydrogel microparticles from lithographic processes: Novel materials for fundamental and applied colloid science. *Curr Opin Colloid In* **2011,** 16, (2), 106-117.

16.   Ross, C.; Cheng, J. Patterned Magnetic Media Made by Self-Assembled Block-Copolymer Lithography. *MRS Bull.* **2008,** 33, (9), 838-845.

17.   Khoushabi, A.; Schmocker, A.; Pioletti, D. P.; Moser, C.; Schizas, C.; Manson, J. A.; Bourban, P. E. Photo-polymerization, swelling and mechanical properties of cellulose fibre reinforced poly(ethylene glycol) hydrogels. *Compos. Sci. Technol.* **2015,** 119, 93-99.

18. Bates, F. S.; Fredrickson, G. H. Block Copolymers: Designer Soft Materials. *Phys.Today* **1999,** 52, 32-38.

19.   Guo, C.; Bailey, T. S. Highly distensible nanostructured elastic hydrogels from AB diblock and ABA triblock copolymer melt blends. *Soft Matter* **2010,** 6, (19), 4807-4818.

20.   Guo, C.; Bailey, T. S. Tailoring mechanical response through coronal layer overlap in tethered micelle hydrogel networks. *Soft Matter* **2015,** 11, (37), 7345-7355.

21.   Guo, C.; Lewis, J. T.; Scalfani, V. F.; Schwartz, M. M.; Bailey, T. S. Dangling-End Double Networks: Tapping Hidden Toughness in Highly Swollen Thermoplastic Elastomer Hydrogels. *Chem. Mater.* **2016,** 28, (6), 1678-1690.

22.   Huq, N. A.; Ekblad, J. R.; Leonard, A. T.; Scalfani, V. F.; Bailey, T. S. Phototunable Thermoplastic Elastomer Hydrogel Networks. *Macromolecules* **2017,** 50, (4), 1331 - 1341.

23.   Huq, N. A.; Lafleur, R. P. M.; Bailey, T. S., Melt-fabricated photoreactive block copolymer micelles as building blocks for tunable elastomeric hydrogels. CSU: NanoLetters (submitted), 2017.

24.   Becker, H. D. Unimolecular photochemistry of anthracenes. *Chem. Rev.* **1993,** 93, (1), 145-172.

25.   Fetters, L. J.; Lohse, D. J.; Richter, D.; Witten, T. A.; Zirkel, A. Connection between Polymer Molecular Weight, Density, Chain Dimensions, and Melt Viscoelastic Properties. *Macromolecules* **1994,** 27, (17), 4639-47.

26.   Coursan, M.; Desvergne, J. P.; Deffieux, A. Reversible photodimerisation of ω-anthrylpolystyrenes. *Macromol. Chem. Phys.* **1996,** 197, (5), 1599-1608.

Chapter 7.

Summary and Future Directions

7.1 Summary of Major Results

Development of this novel photoactive thermoplastic elastomer hydrogel system resulted in an easily fabricated, highly modular and tunable material which affords the ability to fix mechanical and swelling properties of the final hydrogel *in situ*. There are four major results from the research discussed in this dissertation. In Chapter 3, a series of TPE hydrogels based on single component photoreactive SO-anth block copolymers were fabricated. Irradiation in the melt state induces photodimerization of the terminal anthracene units, producing SOS triblock copolymer *in situ*. This new SOS population serves to tether adjacent hydrophobic PS domains, forming a mechanically robust hydrogel after sample vitrification and swelling in water. Through adjustment of UV irradiation time, the installed triblock copolymer concentration could be controlled, producing hydrogels in which the resultant water content and mechanical properties could be easily tuned with moduli spanning 10 - 100 kPa with UV irradiation times under 20 min with a slight axial gradient relative to their homogeneously pre-blended counterparts

In Chapter 4, a series of pre-structured hydrogels were built from self-assembled light-responsive BCPs of anthracene end-functional PS–*b*-PEO (SO-anth). Cyclic irradiation of these hydrogels showed minimal initial success, prompting study of the effect of the phenyl-based PS A block on coupling efficiencies where we compared photocoupling behavior of PI-anth and PS-anth, where minimal differences were found between the two systems. This led to revisiting of a one-component SO-anth system with a BHT radical inhibitor incorporated, which confirmed the

ability of SO-anth to controllably photocouple. While these hydrogels appeared mechanically viable for UF membrane applications, they showed resistance to recoupling, possibly due to poor dispersal and performance of the radical inhibitor used.

In Chapter 5, we explored photoreactive block copolymer micelles formed through self-assembly of SO-anth in the melt, which could then be dispersed in water to form spreadable precursor solutions easily transformed into soft, elastic hydrogels with UV irradiation. Micelle structure created during initial phase separation (~ 5 min) was sufficient to produce narrow size distributions and shape uniformity, and micelles were stable in water without evidence of aggregation or degradation over a period of at least nine weeks. Equilibrium swelling (Q_{final}), dynamic elastic modulus, and tensile modulus could be tuned using both UV irradiation time and initial micelle concentration ($Q_{initial}$). UV irradiation time at constant $Q_{initial}$ was positively correlated with SOS concentration, resulting in tunable dynamic elastic moduli between 0.6 and 2.1 kPa. Conversely, decreasing $Q_{initial}$ (micelle spacing) under constant irradiation time could also be used to produce higher moduli and limit Q_{final}. Photocoupling in molds could be used to generate custom shapes with excellent conformal integrity and retention of form upon swelling. Overall, the ability to selectively disperse these micelle building blocks into stable, moldable solutions allows us to produce soft, flexible, highly conformable hydrogels without the presence of harmful solvents or other leechable small-molecule byproducts.

In Chapter 6, we extended the one-component photoreactive construct to one which exploited blends of SO, SO-anth, and SOS copolymer. These blends were self-assembled in the melt state to form a photoactive BCP micelle network held together with a primary mesh of SOS triblock copolymer. The effects of photoinstallation of a secondary SOS network using available dangling SO-anth chains were distinctly different depending on whether samples were irradiated

in the dry melt, or at their swollen equilibrium dimensions. Samples irradiated at equilibrium, resulting in the primary and secondary networks in separate states of stress, exhibited significant improvements in toughness compared to the melt-photocoupled counterparts where the secondary network was installed under equivalent stress as the primary SOS tethers. Adjustment of the initial primary SOS content did not appear to affect these results. Photopatterning hydrogels in the swollen state allowed direct installation of the secondary network in targeted regions of the hydrogel. This ability to define regions of reinforcement led to an exploration of the effects of anisotropy in tether concentration on mechanical properties. Photomasks were then used to install evenly distributed parallel lines of secondary networks of SOS tethers. Notably, patterning lines parallel to the load direction produced toughness comparable to homogeneously (fully) irradiated hydrogels, while patterning perpendicular to the load direction yielded minimal mechanical improvement. Photopatterning in the melt state, did not produce increased toughness observed to manifest in samples irradiated in the swollen state. However, it did result in producing distinct surface topography. Masked areas, with no added SOS tethers relative to the primary concentration added prior to irradiation, appeared more swollen than UV exposed areas, allowing for highly detailed transfer of unique topographies onto the hydrogel surfaces. The ability to install multiple networks through simple UV exposure provides access to tunable and directionally-dependent states of swelling and material toughness. This type of versatility in a hydrogel produced from a single block copolymer species is a rather remarkable achievement.

The ability to install tethering triblock copolymer at any point after self-assembly introduces a new level of control to our TPE hydrogel construct. This work focused on development of this one-component photoactive polymer construct as a highly tunable hydrogel with access to a large array of mechanical properties, shapes, and swelling behaviors applicable to a wide range

of applications. Controllable properties using irradiation time and the amount of water in the system upon irradiation, potential for reversible and repeatable photocoupling, and the ability to photopattern these materials have resulted in a modular, stable, and potentially biocompatible product with high potential for a range of undiscovered additional properties and possible applications.

7.2 Recommendations for Future Studies

The full potential of the photoactive TPE hydrogel has not yet been reached. There still exist many avenues for exploration with respect to material tunability, in addition to potential applications already accessible based on our current understanding of the material. For instance, one major area not yet studied is the role of UV intensity on photocoupling behavior. All studies included in this work appeared to reach a plateau or maximum for SOS triblock copolymer photoinstallation. However, adjustment of the UV intensity may mitigate this limitation. A deeper understanding of the coupling kinetics of various sized constituents, as well as spatial distribution of photoinstalled tethers due to UV intensity depth dependence may allow for more precise control of material properties.

7.2.1 Biomedical Applications

These materials have promise for use in biological settings due to their mechanical properties and shapeability, the ability to spatially direct areas of reinforcement, the absence of harmful solvents and leechable byproducts; additionally, preliminary evidence for acceptable cytotoxicity levels has been found in unpublished work by Jackson T. Lewis. However, there remains work to be done to ensure dependability of this hydrogel as a biomedically relevant material. Initial work

shows promise for stability in the body, but these materials will eventually require more in-depth as well as *in vivo* stability testing.

The development of micellar building blocks in solution (Chapter 5) has shown great potential for a number of biomedically relevant applications due to its moldability and tunability based on concentration and irradiation time. However, implementing the material in these varied applications requires further adaptation and testing. To begin with, use in dermal applications which aim towards wound healing would require testing the network's effectiveness as a drug encapsulation matrix, which we have yet to physically test. The ability for this highly stable matrix to controllably and effectively release the drugs also depends on the ability to reliably reverse the anthracene substituent dimerization, a strategy which requires further refinement and discussed in more detail with respect to filtration membrane development in the next section.

Perhaps most importantly, thorough cytotoxicity tests are necessary for both dermal/external and internal biomedical applications, to determine whether this material is biologically appropriate for its end use. This includes testing for suitability as a soft tissue repair material, or even cosmetic applications. The versatility of the material afforded by varied fabrication and treatment strategies, such as melt coupling, dilution, and the ability to effectively photopattern for topography and mechanical customization actually extends its use to tougher soft tissues in the body, as well as the ability to more closely mimic those which exhibit anisotropy and regions of varied mechanical properties. This vast application base therefore requires study of material combability specific to its biomedical application and setting.

In summary, this hydrogel appears very well-suited to biomedical applications based on composition and mechanical testing, but requires final verification of its utility in the form of

checks on toxicity, *in vivo* testing, and stability studies of the material in biological environments.

7.2.2 Membrane Development

This section serves to present potential future directions and considerations to facilitate continued development of the pore-size tunable, reversibly fouling UF hydrogel membrane. One major limitation of the TPE hydrogel for filtration purposes is the presence of MRI-visible defects in the matrix, a product of the fabrication method involving melt-state self-assembly and core vitrification upon cooling. Varied grain sizes before pressing tends to trap bubbles in the polymer, even under high pressure and time. Since the effectiveness of the membrane is compromised if defects exist which are larger than the targeted pore size, minimization of defects must be accomplished for this purpose. One option may be to form the network in solution as opposed to the melt as has been preliminarily attempted, which may prevent large grains and therefore large gaps in the material. This will also extend mesh-size and mechanical property tunability of the photoactive TPE hydrogel, and also provide greater control to film thickness, allowing for a thin film UF membrane which can still withstand significant pressures associated with the filtration process. Highly concentrated viscous solutions may be applied using knife coating techniques to achieve this, while dilute systems could simply be cast and evaporated to reveal a thin, uniform film. Simple casting or flow techniques, with or without solvent, could also be used to produce thin films of a tethered membrane.

The next steps, after perfecting thin film fabrication of the UF membrane, would be to thoroughly test pore size tunability and filtration capabilities through release studies at various UV-installed SOS contents. If pore sizes smaller than the hydrogel's fully photocoupled limit are required for some applications, a potential route would be to incorporate photoactive

functionalities along the backbone of the PEO blocks at intervals which are ideal for photocoupling availability when self-assembled into photoactive micelles. This would require the presence of hydroxyl groups along the PEO chain backbone, to then be subsequently modified with anthracene as accomplished for end group functionality. This would potentially produce coronal micelles with higher concentration of photoactive tethering sites to result in a much higher tether density. Polymerized ethoxy ethyl glycidyl ether (PEEGE) can be used to provide the desired glycidyl ether backbone functionality when randomly or directly interspersed with PEO blocks, to form polyglycidol. Once pore sizes have been determined with initial screening using nanoparticles, testing using biological molecules can be performed using HPLC. The goal is to access a large range of porosities, with the primary, preblended SOS mesh setting the lower limit of porosity, and the photo-installed SOS content providing tethers and entanglements serving to determine the upper limit of porosity.

A final feature that must be further addressed for development of the reversible fouling feature in the UF membrane hydrogel, is to implement fully reversible photocoupling of the SO-anth chains ends. Addressing radical instability as a potential source of this limitation is necessary to improve this construct towards use as an effective, reversibly fouling filtration membrane. This may involve further exploration of both PS and the anthracene substituent as potential sources of radicals, preliminarily addressed by addition of BHT but requiring refinement. Another potential study would be to test the source of instability through development of a functional precursor with a longer carbon chain between oxygen from the parent SO-OH and the anthracene molecule, such as 9-chloropropyl anthracene. This increased distance between oxygen and anthracene may prevent the radical movement towards O to break the functionality. A final option is exploration of alternative reversibly photocoupled end-groups.

In summary, success of the hydrogel as a novel and highly effective UF membrane requires minimization of defects through refinement of the fabrication method, verification of tunable selectivity through use of nanoparticles and biomacromolecules using HPLC, and reversible photocoupling capabilities. This perfected membrane will address many of the shortcomings of UF membranes in use currently.

7.3 Final Remarks

In conclusion, this block copolymer-based system is capable of accessing a large range of mechanical properties, sizes, shapes, and behavior, all of which are tuned through a combination of irradiation time, initial water content upon irradiation, and spatially directed irradiation to impose regions of reinforcement and anisotropy. This capability results in a highly modular system which has shown potential for suitability in a large range of areas including biomedical and separations-based applications.